LEAN BLOWOUT AND ITS ROBUST SENSING

IN SWIRL COMBUSTORS

A Dissertation
Presented to
The Academic Faculty

by

Ravi Kiran Bompelly

In Partial Fulfillment
of the Requirements for the Degree
Doctor of Philosophy in the
School of Aerospace Engineering

School of Aerospace Engineering
Georgia Institute of Technology
May 2013

LEAN BLOWOUT AND ITS ROBUST SENSING

IN SWIRL COMBUSTORS

Approved by:

Dr. Jerry Seitzman, Advisor
School of Aerospace Engineering
Georgia Institute of Technology

Dr. Benn T. Zinn
Aerospace Engineering
Georgia Institute of Technology

Dr. Timothy Lieuwen
School of Aerospace Engineering
Georgia Institute of Technology

Dr. Clarence T. Chang
Combustion Branch
NASA Glenn Research Center, OH.

Dr. Jeff Jagoda
School of Aerospace Engineering
Georgia Institute of Technology

Date Approved: 22nd August 2012

To my family

For their love and support

ACKNOWLEDGEMENTS

First of all, I would like to thank my advisor Dr. Jerry Seitzman for believing in me and giving me the opportunity to work on my PhD research. His guidance, support and constructive criticism helped me greatly in accomplishing the research tasks. It was a real pleasure working with him and the things I learnt from him will be an invaluable asset to my career.

I would also like to thank Dr. Tim Lieuwen for his guidance and support during the initial part of the research. In addition I would like to thank Dr. Jeff Jagoda, Dr. Ben T. Zinn and Dr. Clarence Chang for being on my thesis committee and providing helpful comments.

I would like to acknowledge NASA Glenn Research Center for funding this research project. I thank Mr. John Delaat and Dr. Clarence Chang for monitoring the project and providing support and guidance.

I would like to thank the research staff at the combustion lab for maintaining the experimental facilities in great shape and helping me with the usage. I would like to thank Bobby Noble, David Scarbrough, Sasha Bibik, Eugene Lubarsky, Yedidia Neumeier and Brad Ochs for their help and advice in conducting my experiments.

I would like to thank all my fellow graduate students at the combustion lab for the great research and social environment they provided. The intellectual discussions I had with them helped me immensely in understanding things clearly and advancing my knowledge. A special thanks goes to Karthik for helping me with running my experiments at odd times of the day. I would like to thank Yash, Chilu, Yogish, Sai,

Arun, Nishant, Sampath, Jack, Ianko, Ben, Jacheol, Yong, JP and Nori for their help in my hour of need. I thank my qualifying exam study group, Jackie, Jack, Shreekrishna, Tom and Caleb, who made the task much easier.

Finally I thank my family for their love and support throughout the journey of my life.

TABLE OF CONTENTS

LIST OF TABLES

LIST OF FIGURES

NOMENCLATURE

a	Duct diameter
C	Speed of sound
k	Acoustic wave number
M	Mach number
$Ps3$	Combustor inlet static pressure
R	Reflection coefficient
T	Transmission coefficient
U	Uniform random number
Wf	Fuel flow rate
Z	Acoustic impedance
λ	Average event occurrence rate
Λ	Expected number of events in a transient
μ	Signal mean
φ	Normalized equivalence ratio
Φ	Equivalence ratio
ρ	Density
σ	Signal standard deviation
LBO	Lean Blow Out
LDI	Lean Direct Injection
RU	Ratio Unit
SI	Stability Index
TBE	Time Between Events

SUMMARY

Lean combustion is increasingly employed in both ground-based gas turbines and aircraft engines for minimizing NO_x emissions. Operating under lean conditions increases the risk of Lean Blowout (LBO). Thus LBO proximity sensors, combined with appropriate blowout prevention systems, have the potential to improve the performance of engines. In previous studies, atmospheric pressure, swirl flames near LBO have been observed to exhibit partial extinction and re-ignition events called LBO precursors. Detecting these precursor events in optical and acoustic signals with simple non-intrusive sensors provided a measure of LBO proximity.

This thesis examines robust LBO margin sensing approaches, by exploring LBO precursors in the presence of combustion dynamics and for combustor operating conditions that are more representative of practical combustors, i.e., elevated pressure and preheat temperature. To this end, two combustors were used: a gas-fueled, atmospheric pressure combustor that exhibits pronounced combustion dynamics under a wide range of lean conditions, and a low NO_x, liquid-fueled Lean Direct Injection (LDI) combustor, operating at elevated pressure and preheat temperature. In the gas-fueled combustor, flame extinction and re-ignition LBO precursor events were observed in the presence of strong combustion dynamics, and were similar to those observed in dynamically stable conditions. However, the signature of the events in the raw optical signals have different characteristics under various operating conditions. Low-pass filtering and a single threshold-based event detection algorithm provided robust precursor sensing, regardless of the type or level of dynamic instability. The same algorithm provides robust event detection in the LDI combustor, which also exhibits low level dynamic oscillations. Compared to the gas-fueled combustor, the LDI events have weaker signatures, much shorter durations, but considerably higher occurrence rates. The

disparity in precursor durations is due to a flame mode switch that occurs during precursors in the gas-fueled combustor, which is absent in the LDI combustor.

Acoustic sensing was also investigated in both the combustors. Low-pass filtering is required to reveal a precursor signature under dynamically unstable conditions in the gas-fueled combustor. On the other hand in the LDI combustor, neither the raw signals nor the low-pass filtered signals reveal precursor events. The failure of acoustic sensing is attributed in part to the lower heat release variations, and the similarity in time scales for the precursors and dynamic oscillations in the LDI combustor. In addition, the impact of acoustic reflections from combustor boundaries and transducer placement was addressed by modeling reflections in a one-dimensional combustor geometry with an impedance jump caused by the flame.

Implementing LBO margin sensors in gas turbine engines can potentially improve time response during deceleration transients by allowing lower operating margins. Occurrence of precursor events under transient operating conditions was examined with a statistical approach. For example, the rate at which the fuel-air ratio can be safely reduced might be limited by the requirement that at least one precursor occurs before blowout. The statistics governing the probability of a precursor event occurring during some time interval was shown to be reasonably modeled by Poisson statistics. A method has been developed to select a lower operating margin when LBO proximity sensors are employed, such that the lowered margin case provides a similar reliability in preventing LBO as the standard approach utilizing a more restrictive operating margin. Illustrative improvements in transient response and reliabilities in preventing LBO are presented for a model turbofan engine. In addition, an event-based, active LBO control approach for deceleration transients is also demonstrated in the engine simulation.

CHAPTER 1

INTRODUCTION

1.1. Motivation

Reduction of pollutant emissions from ground-based gas turbine engines and aircraft engines is essential for protecting air quality and preventing damage to the environment. Nitrogen oxides (NO_x) are a major pollutant with many adverse effects on the environment. At ground level and low altitudes, NO_x emissions contribute to formation of photochemical smog, harmful ozone and acid rain [1]. NO_x emissions from current subsonic commercial aircraft operating at cruise altitudes (9-13 km) increase ozone levels along the traffic routes, which could alter the climate [2] . At high altitudes (17-20 km) in the stratosphere, corresponding to the cruise altitudes of future supersonic passenger aircraft, NO_x emissions would lead to depletion of the ultraviolet-blocking ozone layer [2].

NO_x emissions in lean conditions are generally an exponential function of flame temperature. Hence lowering average flame temperatures and avoiding local temperature peaks can greatly reduce NO_X emissions. In addition, lowering the residence time combustion products spend at high temperature (before temperature drops due to work extraction or heat transfer) can aid in reducing NO_x. Fuel lean operation with uniform fuel-air mixing produces the homogenous and low combustion zone temperatures required for lowering NO_x. Hence, recent gas turbine combustor design approaches have mainly focused on leaner combustion, using premixed or partially premixed operation as a preferred option for NO_x reduction. Lean premixed operation has reduced NO_x emissions substantially in land based gas turbine engines [3]. Similarly, lean premixed pre-vaporized (LPP) [4], and Lean Direct Injection (LDI) [5] combustion approaches are suggested solutions for NO_x reduction in aero engines. An alternate approach, Rich-

Quench-Lean (RQL) combustion, has also been pursued [6]. While RQL is preferred for its enhanced stability, incomplete mixing between rich products and secondary air and higher particulate emissions in RQL favor lean combustion approaches [7].

Continuous combustion in gas turbines, in contrast to intermittent combustion in reciprocating engines, requires a stable flame to continuously burn fuel. The flame needs to be stable in high velocity streams employed for producing high heat release rates in compact volumes. Gas turbine engine main combustors predominantly use flow recirculation generated by swirl and sudden area expansion for flame stabilization. In addition, a pilot flame is occasionally employed. The recirculation region provides a continuous supply of hot products and radicals to the oncoming reactants and helps stabilize the flame [8]. In addition, flow recirculation creates low velocity regions where flame speed can match flow speed for flame stabilization. By making a fuel-air mixture leaner, the stabilization process weakens due to multiple reasons. For example, lean mixtures result in low product temperatures and radical concentrations in recirculation zone reducing their ability to ignite reactants. In addition, flame speed decreases for leaner mixtures, such that it cannot match flow speed, required for stabilization. Furthermore, lean flames are less able to withstand high flame stretch rates [9], as the extinction strain rate is lower for lean mixtures. Swirl stabilized flames usually experience high stretch rates due to high velocity gradients and turbulence levels, making lean flames more susceptible to extinction. Therefore for sufficiently lean mixtures, a flame cannot be stabilized, resulting in flame Lean Blowout (LBO). This is also referred to as static instability of a flame.

Lean blowout results in disruption of essential power or thrust output from engines and requires a complex relight procedure to restore power. In land-based gas turbines used for electric power generation, power outage resulting from LBO would require operators to pay penalties making LBO an expensive problem. In aero engines,

LBO is a flight safety hazard. For example, LBO near ground level could lead to a catastrophic crash since aircrafts would descend rapidly with no thrust and little time for engine restart. LBO at cruise altitudes can require considerable reduction in altitude as it is hard to relight at high altitudes where ambient pressure and temperature are low.

The exact conditions at which LBO occurs are hard to predict. For example, LBO occurrence is dependent on local flow conditions, including turbulence levels, temperature, equivalence ratio, spray properties (for liquid fuels), fuel composition and product entrainment into the reactants. These conditions are not precisely known or predictable during engine operation, and can vary significantly with engine operating conditions or due to aging effects. In addition, inherent disturbances in engine operating conditions can push the combustor to LBO. Thus combustors are typically designed with large operating margins to avoid LBO, i.e., with a flame zone equivalence ratio much higher than the actual LBO limit. However, excessive margins mean the engine is likely operating at sub-optimal conditions. If however, LBO margin sensors and control systems were available to avoid LBO, the required margins could be reduced, and further reduction of NO_x could be achieved.

For land-based gas turbine engines, the operating point may be chosen primarily to minimize NO_x while maintaining allowable CO emissions and preventing LBO and excessive combustion dynamics. NO_x and CO emissions, along with an LBO boundary, are illustrated in Figure 1 for a "typical" Dry Low NO_x (DLN) combustor. Keeping NO_x and CO within the allowable limits (for example, 15 ppm for NOx and 25 ppm for CO) results in a relatively narrow operating range for combustors. Typically, the minimum equivalence ratio for preventing excessive CO emissions is higher than the LBO equivalence ratio. However, this lower bound on equivalence ratio is close to the LBO limit. DLN combustors often employ radial staging using multiple burners within a combustor can to provide sufficient turndown. The burner arrangement requires fuel split

schedules as a function of engine load, for maintaining low emissions throughout the load range. For part load operation, some of the burners operate below their LBO limit while keeping other burners richer, to stabilize the lean burners. In practice, however, it has been observed that power trips due to LBO occurred due to insufficient stabilization provided by rich burners [10]. In land-based engines, fuel tuning is performed regularly in the field, mainly to prevent dynamics. Errors associated with tuning, changes in fuel properties, variation in ambient conditions can result in occasional LBO trips. LBO proximity detection systems could be used to avoid these events and improve the performance of engines.

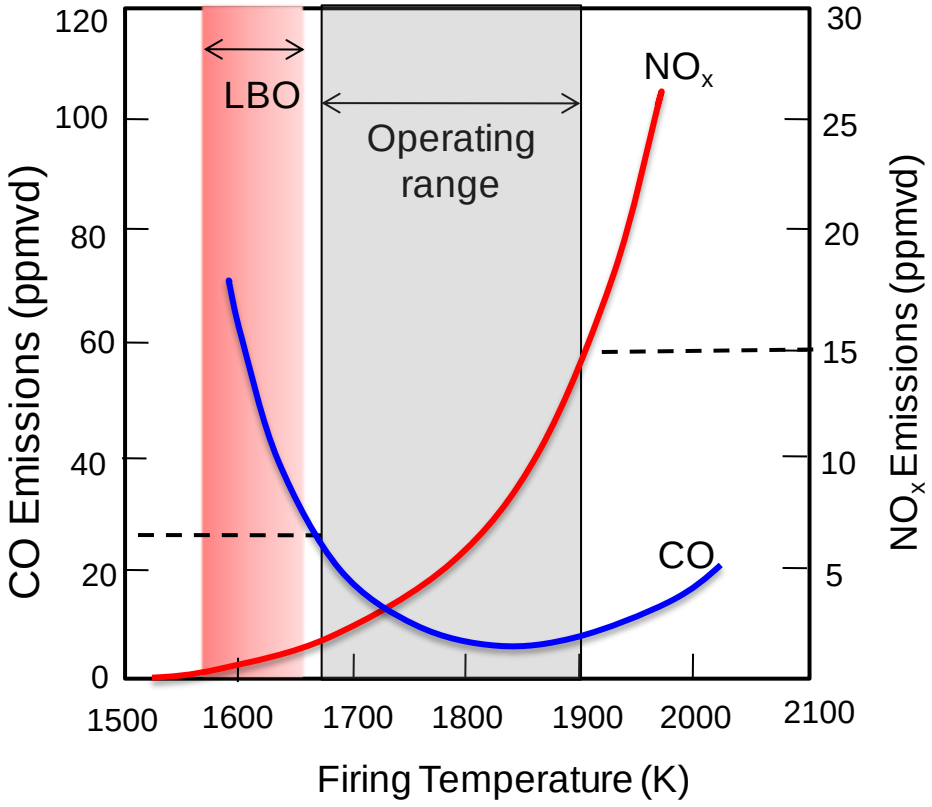

Figure 1. NO_x and CO emissions in a Dry Low NOx (DLN) combustion system as

For aero engines, NO_x is regulated at low altitudes (take off, approach and landing). Though not currently regulated at cruise altitudes, NO_x at cruise may have the greatest environmental impact, as engines operate for the most time at cruise. For

achieving low emissions using lean combustion, radial staging using a dual annular combustor [11] or staging within swirlers using multiple swirlers [12] are often employed to provide sufficient turndown. The combustor configuration can also consist of a pilot and a main region. The pilot operates alone at low power levels, and at high power levels, it acts to stabilize the leaner main section. An illustration of average primary zone (a region without secondary air dilution) equivalence ratios of the pilot and main regions are shown in Figure 2. In addition, an example LBO margin and LBO limit are shown. The LBO limit can be expected to decrease with engine power, as higher compressor exit pressures and temperatures would tend to lower the equivalence ratio where LBO occurs. For minimizing NO_x at the operating points of interest, e.g., cruise or full power take-off, the design points should be at the lowest possible equivalence ratio. However this can result in other operating points, e.g., idle or where the main region switches, falling below the required LBO safety margin. Hence the constraint of having minimum required LBO margin over the entire operating range of an engine results in non-optimal emission performance at points where NO_x has to be reduced. An LBO control system that ensures stable engine operation at these off-design conditions would allow reduced LBO margins and therefore lower NO_x emissions at the design points. At the off-design conditions, the LBO control system would likely be free to act without the constraint to minimize NO_x emissions.

In aero engines, LBO can occur during steady-state operation or during power reduction transients, i.e., deceleration. To decrease power, fuel flow to a combustor is reduced, resulting in lower gas temperatures/velocities entering the turbine and reduced turbine work. This slows down the shaft rotational speed as the turbine cannot provide sufficient torque to drive the compressor at the same speed. The reduced rate depends on the inertias of the compressor, turbine and connecting shafts, and on the torque deficit on the compressor. The mass flow rate of air through the compressor depends on the compressor shaft speed for a given flight Mach number. While fuel flow can be reduced

quickly to reduce power, air flow rate drops rather slowly. This results in lower combustor equivalence ratios, which push the combustor closer to LBO. This process is illustrated in Figure 3, where pilot primary zone equivalence ratio is plotted as a function of engine power during steady-state operation and a fast deceleration transient from full power to idle. For illustrative purpose, only the pilot zone equivalence ratio is shown, as the pilot is the main stabilization mechanism.

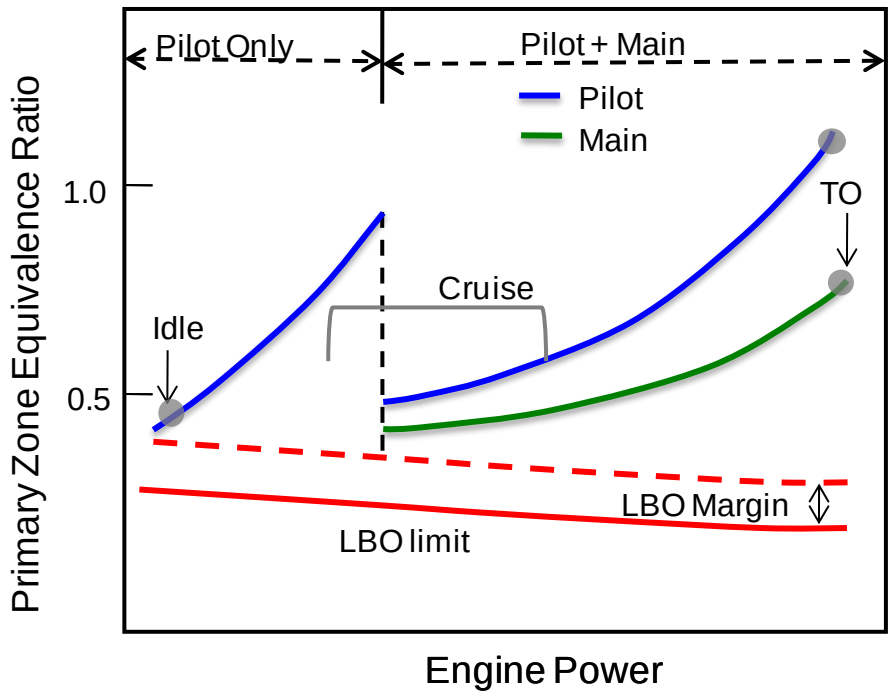

Figure 2. Variation with engine power of pilot and main primary zone equivalence ratios of a lean-operation aero engine combustor.

Due to the uncertainty in LBO conditions, the minimum allowed equivalence ratio during a deceleration transient is kept well above the LBO boundary, i.e., a large LBO margin is used (20% above the LBO limit in [13]). This is achieved by a slower fuel flow rate drop or raising the minimum allowed equivalence ratio limit in the engine controller. In either case, the result is a slower engine transient response. With LBO margin detection sensors, LBO margins can be decreased, improving deceleration transient response. The improved deceleration response can have multiple benefits, for example,

faster aircraft descent or enabling engines to be used more effectively as backup flight control in case control surfaces, such as the rudder, fail.

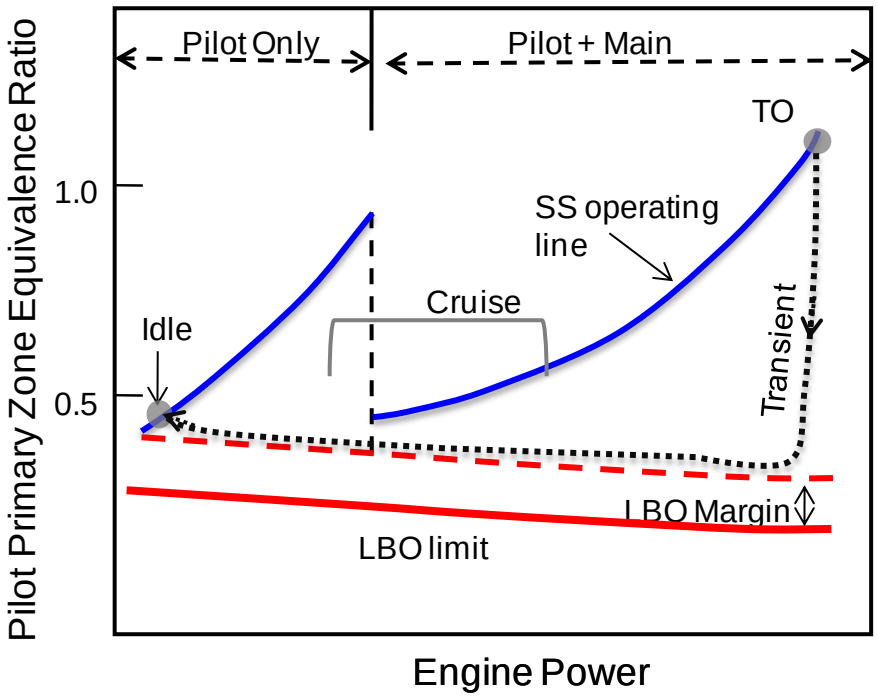

Figure 3. Variation of pilot primary zone equivalence ratio during a rapid transient from full power to idle.

In land-based gas turbines used for electric power generation, generator shaft rotational speed has to be kept nearly constant in order to maintain the electrical frequency, e.g., 50 or 60 Hz. When load on the generator is rapidly shed, shaft rotational speed increases, causing an increase in the frequency or excessive turbine speed. A higher electrical frequency can result in a power trip, whereas excessive turbine speed can result in mechanical damage to the gas turbine. In both cases, shaft speed has to be reduced rapidly to ensure safe operation. Similar to the aircraft engine decelerations described above, shaft speed is reduced by lowering fuel flow, thus pushing combustors towards LBO. By employing lower LBO margins, fuel flow rate can be reduced further and shaft speeds can be reduced faster, thus preventing power trips and avoiding engine damage.

From these examples, it is clear that having an LBO proximity sensor would improve performance and reliability of gas turbine engines. It would permit reduction in minimum required LBO margins, allowing for reduced NO_x emissions and improved transient response. Ideally, the sensor would be simple in construction, non-intrusive and capable of working in harsh engine conditions. In addition, the sensor should have good sensitivity, time response and be robust to varying operating conditions. Therefore the main objective of this study is to develop a robust sensing methodology capable of warning of imminent LBO in real time.

1.2. Previous Work

For reliable flame blowout prevention, it is essential to understand the physical process governing the blowout phenomenon. Such understanding may aid in developing sensors for blowout prevention. In combustors, blowout can be caused by various fluid mechanic and chemical process depending on the combustor configuration, flame stabilization method, and other operating conditions. Generally combustion cannot be sustained below an extinction limit, where heat release during the residence time of the gases in the combustor is not sufficient enough to increase the reactant energy (temperature) above the minimum activation energy required for combustion. Well-stirred reactor models employing this property sometimes successfully predict blowout conditions [14]. Most turbine engine combustors use flow recirculation as a primary method for flame stabilization. Blowout occurs when the flame stabilization mechanism is not adequate to hold a flame. For example, flow turbulence may induce unsteady flame stretch sufficient enough to cause local extinctions for lean flames. These extinctions may result in decreased temperature/radical concentration in the recirculation zone and ultimately cause blowout [15]. In addition, LBO could occur due to insufficient time for ignition of reactants in a high velocity stream. High velocities of reactants in the shear layer between the recirculation zone and free stream would result in small residence

times compared to chemical time scales making the reactants hard to ignite. This phenomenon has been employed in bluff body stabilized flames using Damkohler number for LBO prediction [16]. Though there is a considerable amount of literature regarding blow off in bluff body stabilized flames, in swirl stabilized flames there is only a limited amount of previous work.

Combustor blowout is often observed to be non-abrupt and preceded by transient unsteady phenomenon. For example in swirl flames near blow out, some unsteady behavior is often observed in terms of flame area, flame shape or heat release. Hedman et al. [17] observed oscillations near blowout between a flame that is attached around the recirculation zone and one that is lifted off from the recirculation zone. In addition, they observed the oscillating flame condition to be stable for a high swirl case, but it would occasionally extinguish for medium swirl conditions. Griebel et al. [18] observed oscillations in flame postion, shape and length oscillating prior to blowout. Similar unsteady flame behavior was observed in a non-premixed, swirl stabilized combustor by Sturgess et al. [19, 20]. They observed flame liftoff and subsequently sever intermittency with equivalence ratio reduction. Further reduction in equivalence ratio resulted in large scale axial flame movement before blowing out. The severe unsteady nature of the flame indicates the complexity of the blow out process, making it hard to capture by modeling. The unsteady behavior occurring with a sufficient margin, e.g., in equivalence ratio, above the blowout limit can provide a means for real-time prediction of approaching LBO.

Based on this unsteady behavior prior to LBO, Thiruchengode et al. [21] sensed approaching lean blowout in a premixed, gas-fueled swirl combustor operating at atmospheric pressure. The unsteady behavior was found to be associated with partial flame extinction around the inner recirculation zone followed by its re-ignition. The extinction and re-ignition events were called LBO precursor events as they precede LBO

and ultimately lead to LBO. These events were detected in flame optical [21] and acoustic [22] emissions using simple non-intrusive sensors. The precursor events were observed to occur more often as the combustor's stability margin (Φ-Φ_{LBO} or Φ/Φ_{LBO}) was reduced. Hence, the average occurrence rate of precursor events was shown to provide a measure of the combustor's proximity to blowout. Active control of LBO was also demonstrated by actuating a pilot fuel responding to number of events occurring in a unit time window.

Spectral methods based on estimation of relative spectral power at low frequencies, e.g. 5-50 Hz, was also demonstrated to provide a measure of LBO margin by Nair and Lieuwen [22] and Prakash et al. [23], in the same gas fueled combustor employed by Thiruchengode et al. [21]. Precursor events having relatively long durations (20-50 ms) and with low occurrence rates (2-5 sec^{-1}) contribute to increased power at low frequencies. A similar approach, low frequency tone increase in the acoustic signature from the combustor of a ground based gas turbine engine, was used to estimate the probability of incipient blowout of the engine by Taware et al. [24].

Both event based and spectral methods were shown to be capable of approaching LBO detection in a non-premixed liquid-fueled combustor operating at atmospheric pressure [25, 26]. In addition standard deviation of the optical signal was also shown to indicate LBO proximity in a liquid-fueled combustor by Yi and Gutmark [27]. An alternate sensing technique to optical and acoustic emissions was explored by Thornton et al. [28]. They used detection of changes in the combustion products' electrical properties to detect LBO precursor events. They monitored the current through low voltage electrodes integrated into the fuel nozzle. During precursor events, there is presumably a decrease in the ionization level, producing a decrease in the current. Li et al. [29] employed a tunable, diode laser absorption sensor to detect LBO margin in a lean, partially premixed model turbine combustor. They monitored temperature fluctuations

associated with the localized and temporary extinction events and used a spectral power approach (0-50 Hz) to analyze the sensor output. For the most part, these techniques rely on the increased unsteadiness of the heat release associated with the occurrence of precursor events.

Among all the possible methods for LBO margin sensing, the event based method is preferable as it has the best time response. Statistical and spectral methods require signal data over sufficient time for reliable LBO margin sensing. On the other hand, events can be detected as soon as they occur and better time response can be achieved.

In addition to LBO (static instability), lean combustion often gives rise to thermoacoustic combustion instabilities (dynamic instability). Dynamic instabilities are associated with high amplitude pressure oscillations resulting from closed-loop coupling between pressure oscillations and heat release oscillations. Lean operation with a high degree of premixing creates a higher risk of dynamic instability problems. For example, combustors employing lean combustion are designed to operate with mostly primary air. This reduces the area of the dilution holes that help damp acoustics [30]. In addition, the combustion process has increased sensitivity to perturbations in equivalence ratio at lean conditions near blow-out [31]. In a premixed system operating very close to blowout, equivalence ratio oscillations have been shown to cause periodic flame extinction giving rise to low frequency oscillations with high amplitudes [30]. Though combustion dynamics are suppressed to acceptable levels by careful design of practical combustors, moderate to low levels of dynamics may continue to exist.

The high amplitude dynamic instabilities that can exist near LBO can also trigger LBO. For example, Snyder and Rosfjord [32] observed that decreasing fuel flow rate increased instability amplitudes and subsequently caused blow off in a turbine engine. In stationary gas turbines, low frequency dynamics (0-100 Hz) often referred to as chug or LBO tone are observed to cause LBO [10, 33]. Similarly in a backward facing step

combustor, Cohen and Anderson [34] observed that reducing the equivalence ratio can produce low frequency instability, with amplitudes rising gradually until blowout occurred. Besides the dynamic instability itself, control methods used to suppress dynamics, such as fuel flow rate modulation and fuel spatial distribution control, could also lead to blow out.

1.3. Overview of Present Work

This thesis is motivated by the goal of improving the robustness of LBO margin sensing by investigating it under a wider range of scenarios. LBO margin sensing studies, until now, were conducted under dynamically stable operating conditions. However as lean combustion often has pronounced dynamic instabilities, even near blow out limits, LBO margin sensing in the presence of high amplitude dynamic instability needs to be investigated. In addition, most of the previous LBO margin sensing studies have been performed at atmospheric pressure under non-realistic engine operating conditions, primarily in premixed, gas-fueled combustors. Hence, LBO margin sensing needs to be studied under more realistic engine operating conditions, i.e., at elevated pressure and preheat operation. The thesis addresses these issues by investigated LBO margin sensing in more complex scenarios, i.e., under dynamically unstable conditions and elevated pressure and preheat operation. LBO margin sensing under dynamically unstable conditions is investigated in a in a premixed, swirl-stabilized combustor similar in design to ground power gas turbine combustors, operating at atmospheric pressure. LBO margin sensing at elevated pressure and preheat temperature is examined in a liquid-fueled low NO_x design combustor similar to future aircraft engine combustors.

Though in previous studies, LBO margin sensing and control was demonstrated during slow transients in combustor operating conditions, its limitations during fast transients have not been investigated. Since precursors are discrete events occurring at a small non-constant rate (typically 1-10 per second in the previous studies), it is not clear

whether any event would occur before LBO in a sufficiently fast transient. Therefore, the thesis develops a methodology to estimate the limits on transient rates such that precursor events occur before LBO. As mentioned earlier, employing LBO margin sensors can potentially improve transient response of engines during rapid decelerations. To this end, the thesis examines the transient response improvements and tradeoffs in implementing precursor event based LBO margin sensing in a model turbofan engine during rapid deceleration transients.

Chapter 2 of the thesis gives a more detailed background on swirl combustion, lean blowout, previous LBO margin sensing studies and conventional LBO prevention in turbine engines. Chapter 3 describes the experimental setups and modeling approaches used in the present study. In Chapter 4, LBO margin sensing under dynamically unstable conditions and at elevated pressure and temperature operation using optical (chemiluminescence) signals is investigated. Chapter 5 investigates the issues in using acoustic signals for LBO margin sensing. In Chapter 6, new approaches are presented for examining LBO margin sensing during rapid transients, and the results of one such analysis are reported. Chapter 7 presents conclusions and contributions of the current work along with suggestions for future investigations.

CHAPTER 2

BACKGROUND AND PREVIOUS WORK

This chapter provides a review of issues related to lean blowout and its margin sensing in swirl-stabilized combustors. The first section describes flow field and flame configurations in swirl combustors. The second section discusses the physical mechanisms associated with lean blowout. The third section describes previous work in LBO margin sensing. The fourth section discusses combustion dynamics and the fifth section covers issues related to control of aero engines.

2.1. Swirl Stabilized Combustion

Practical combustion systems are usually designed to produce high heat release rates in compact volumes, i.e., high power densities, in order to reduce size, weight and cost. In addition, combustors need to be stable over a wide range of combustor loadings and operating conditions. Moreover, high combustion efficiency with low emissions is required. Designers are faced with the challenge of optimizing a combustor to meet all these objectives.

To achieve high power densities, practical combustors often employ high pressures along with high reactant velocities. For gas turbines, the high pressures are also necessary to increase cycle efficiencies; typical gas turbine combustors operate at pressures up to 30-40 bar and employ average flow velocities in the range 10-35 m/s [7]. Flame stabilization in high velocity flow can be challenging. Generally, a premixed flame can be stabilized if flame speed can be matched to flow speed at some point in the flow. However laminar flame speeds, having a range of about 10-100 cm/sec [35], are much lower than typical flow velocities. Therefore, additional stabilization approaches are required to ensure flame stability.

For high velocity flows, flow recirculation is usually employed for flame stabilization. Recirculation regions hold hot products and radicals and promote mixing of reactants with them. Thus recirculation provides a continuous supply of heat and radicals for ignition of reactants and increased flame speed. Combined, these effects lead to enhanced flame stabilization. Commonly used recirculation configurations are: 1) flow recirculation created by vortex break down of a swirling flow; 2) the wake of a bluff body; and 3) sudden expansion created by a step increase in flow area. Other novel methods that do not rely on recirculation are also being investigated for flame stabilization, for example the low swirl burner [36]. It uses low velocity regions created by divergence of flow with a low amount of swirl for flame stabilization.

Gas turbine main combustors predominantly employ swirl-stabilization because swirl: 1) improves flame stability; 2) achieves fast mixing between fuel and air; 3) produces high entrainment of ambient combustor fluid [37]; and 4) results in high power densities. Swirling flows produce high levels of turbulence [8, 38], which increase turbulent burning velocities producing high heat release in a small volume. In addition, the high turbulence levels help faster fuel-air mixing, reducing emissions. The tangential velocity component of the swirl increases aerodynamic forces on fuel spray resulting in faster spray breakup and smaller droplets. The recirculation zone of the swirling flow creates low velocity regions, and stagnation points where flame speed can match flow speed, for improved stabilization [39].

Swirl is created by imparting a tangential velocity component to the flow using swirl vanes, axial plus tangential flow entry or pure tangential flow entry in to a chamber [8]. The strength of a swirling flow is characterized by its swirl number (S), defined as the ratio of axial flux of tangential momentum to the axial flux of linear momentum. For sufficiently strong swirl ($S>0.6$), flow reversal in the vicinity of the central axis is created forming an inner recirculation zone (IRZ). In combustors, formation of an IRZ is usually

triggered by employing a sudden expansion geometry. Formation of the IRZ occurs through the following physical processes [40]. Swirling flow creates a radial pressure gradient due to centrifugal forces having low pressure near the axis. As the flow expands through the sudden expansion geometry, axial decay of tangential velocity and the radial pressure gradient occur. The process creates an adverse axial pressure gradient around the axis, which in turn causes flow reversal. Formation of a recirculation zone is commonly referred to as vortex breakdown. Vortex break down is defined as an abrupt change in the structure of the swirling vortex core resulting in stagnation points and flow recirculation [41]. Vortex breakdown can take several forms depending on swirl strength and Reynolds number. For example, bubble, spiral and helical modes of vortex breakdown have been observed [42, 43]. The type of vortex breakdown characterizes the recirculation zone and evolution of the flow field further downstream. The bubble type of vortex break down is the most common form observed in combustors.

An illustrative swirling flow field having bubble type vortex breakdown is shown in Figure 4 for a typical combustor configuration commonly employed in low NO_x premixed combustion systems. The combustor has an annular swirling flow, around a cylindrical center body, issuing into a sudden expansion [7, 44]. The flow field consists of an inner recirculation zone (IRZ) created by bubble type vortex breakdown. In addition, it consists of an outer recirculation zone (ORZ) over the expansion region (e.g, a backward facing step). Along the boundaries between recirculation zones and the swirling jet, sharp gradients in axial and tangential velocity exist, creating regions of high flow shear. These high shear regions are called the inner and outer shear layers (see Figure 4). The IRZ may be closed, i.e., backward flow only over a short distance, or the backward flow may extend throughout the length of the combustor tube, around the central axis. Employing a converging geometry for the flow exit affects the extent of backward flow region, and suppress it [45]. Besides the IRZ structure shown in Figure 4 with reverse flow in the entire IRZ region, in some cases IRZ may have a two cell

structure with forward velocity in the vicinity of the central axis [42]. In addition to the IRZ created by vortex breakdown, a recirculation zone is formed in the wake of the center body. The center body recirculation may merge with the IRZ forming a continuous reverse flow region. The flow fields seen for isothermal (and isodensity) flow fields can be significantly altered by the heat release associated with combustion, mainly due to dilatation effects. Combustion decreases effective swirl strength, i.e., swirl number, by increasing axial velocity. It reduces the strength of the recirculation zone by lowering the amount of the recirculating fluid [8]. In addition, combustion may suppress the existence of backward flow over a long distance [45] or it may promote the formation of a two cell IRZ.

The flow structure discussed above is based on time average characteristics. Due to high shear in axial and azimuthal shear layers, large scale spatial and temporal fluctuations in the flow field occur [8]. In the shear layers, large scale coherent structures are formed, due to Kelvin-Helmholtz (K-H) instabilities, resulting from the combined effect of axial and azimuthal shear layers [46]. The coherent structures consist of concentrated vortex rings that convect downstream in a helical fashion. The coherent structures modify the flow field and combustion process. For example, the coherent structures have been observed to induce large asymmetry in the flow about the axis [47]. In addition, they can modify the combustion process by wrapping the flame around them, resulting in an increase in unsteady burning. As they travel downstream, the coherent structures break down into smaller, less organized turbulent structures. Besides the coherent structures, swirl flows are often observed to produce precessing vortex cores (PVCs). PVCs are associated with the CRZ precessing around the geometrical axis of the combustor. They are helical in nature, with low pressure in the core, and are wrapped around the CRZ. The occurrence of PVCs is mainly dependent on swirl number and combustor geometry. In addition, the heat release, the type of combustion, i.e., premixed or non-premixed, and the degree of flow confinement influence PVCs. PVCs strongly

affect the flow field, for example they displace the swirling vortex core off the axis and result in non-uniform azimuthal velocities with higher velocities near the combustor wall. They typically exist for a downstream distance of 1-2 combustor diameters, starting from the inlet, before breaking up. In addition to the organized structures, the flow includes a high degree of random turbulent velocity fluctuations, with peaks in the inner and outer shear layers.

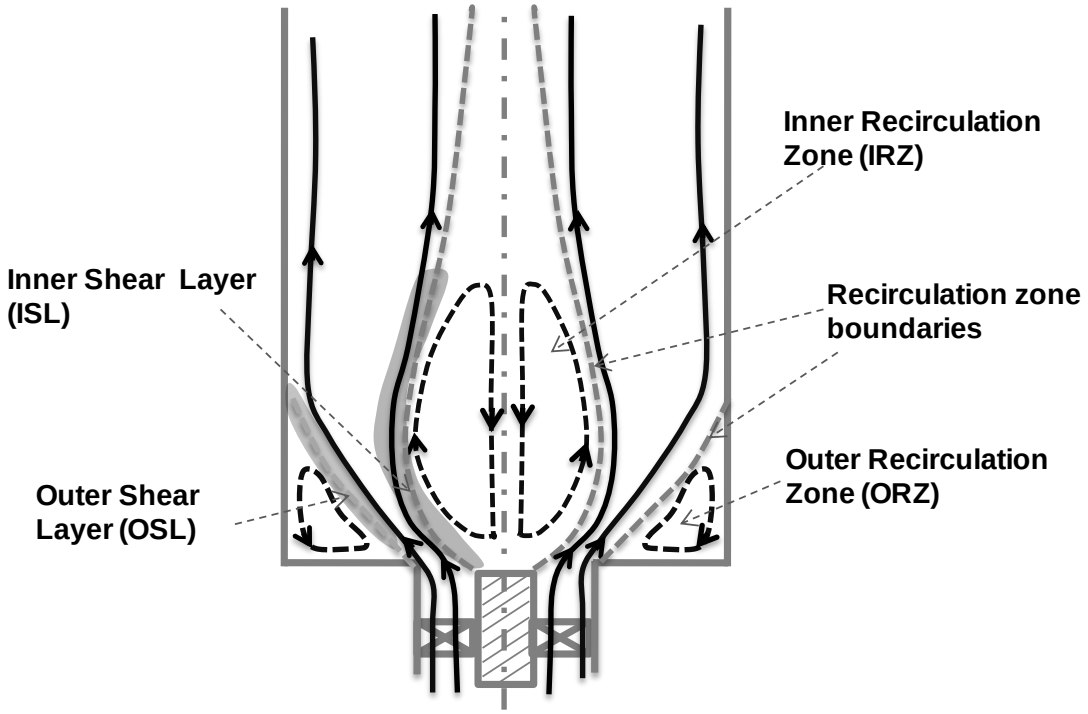

Figure 4. Illustration of a swirling flow field structure.

Depending on the combustor geometry, reactant mixture properties and operating conditions, different flame configurations exist in swirl-stabilized combustors. The configurations often have a pronounced effect on flame static and dynamic instability, emissions and wall heat transfer. Example flame configurations in premixed operation, for the combustor geometry in Figure 4, are shown in Figure 5. In configuration (a), a flame is present in inner and outer shear layers. The flame separates cold reactants in the swirling jet from hot products in recirculation zones. The flame is attached to the center body due to stabilization by the recirculation zone of the center body or by the shear

layer. In configuration (b), there is no flame in the outer shear layer, while there is an inner shear layer flame similar to that in configuration (a), though longer in length to burn all the fuel. For sufficiently lean mixtures, configurations (c) and (d) have been observed. Shifts between flame configurations during combustor operation may occur due to changes in equivalence ratio, fuel composition, preheat temperature and other conditions. The primary cause of configuration shift is due to variation of reactant mixture flame speed or extinction strain rate with changing conditions. The shifting process is often observed to be sudden [48] and sometimes with oscillations [49]. For example, the flame can shift from configuration (a) to (b) when equivalence ratio and preheat temperature are reduced. The configuration can shift back for opposite changes in the conditions. By reducing equivalence ratio, flames have also been observed to shift from configuration (a) to (d), progressively [49, 50]. These flame configurations are on a time-average basis. Instantaneous flame shapes will have severe corrugations due to turbulent, vortical structures wrapping the flame around them [51, 52]. With non-premixed combustion, flame configurations are more complex, influenced by fuel-air mixing. Generally, the flame surface may envelope the inner recirculation zone.

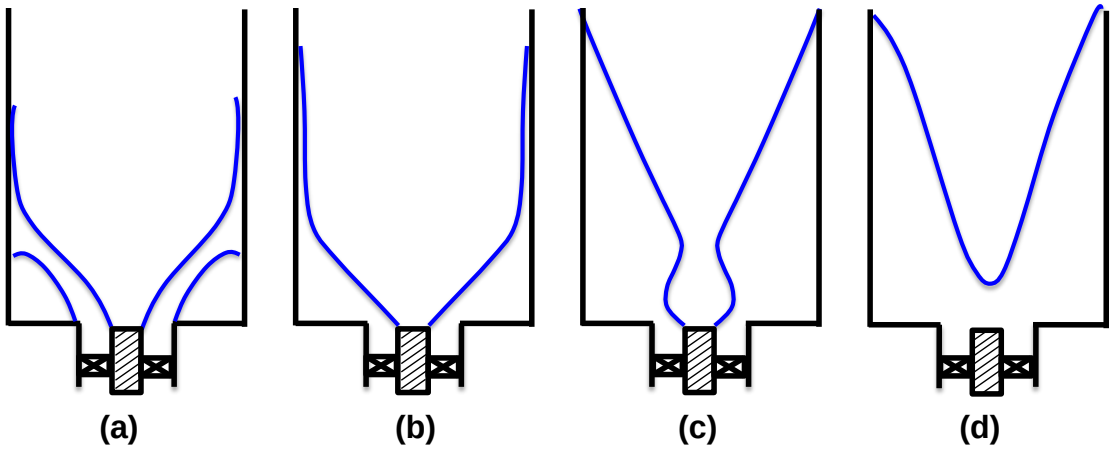

Figure 5. Illustrative flame configurations in premixed swirl combustors.

Shifts in flame configurations can be analyzed from the perspective of strain rates experienced by flames relative to extinction strain rates of the reactant mixture. Flame

straining is essentially caused by species and thermal diffusion non-aligning with flow stream lines and resulting in enthalpy and stoichiometry modification, locally. Such conditions occur due to flame curvature or flow shear upstream of a flame [53]. As an example, a flame can develop local curvature due to vortical turbulent structures whereas velocity gradients cause flame aerodynamic shear. Flames can withstand strain only up to a certain level, denoted the extinction strain rate. Extinction strain rate tends to decreases with reduction in equivalence ratio below stoichiometric conditions. Therefore lean conditions conducive to low NO_x operation produce flames that are more susceptible to extinction. Extinction strain rate of a lean, laminar, methane air flame varies from 500 to 100 s^{-1} between equivalence ratios of 0.6 to 0.5 [53] . The swirl flames described above experience high strain rates in the inner and outer shear layers, sufficient to cause extinction of lean flames. For example Wicksell et al. [51] and Stohr et al. [54] observed strain rates of the order of 1,000 s^{-1} in shear layers. Flame extinction in stabilizing regions due to high strain rate would result in flame configurations shift. The flame may find new stabilizing locations where it experiences low strain rates.

2.2. Lean Blowout

The operating conditions that influence flame blowout in a combustor include fuel-air ratio, pressure, preheat temperature, velocity and fuel composition. In addition, blowout limits vary greatly with combustor design. Identification and understanding of the key physical processes responsible for LBO can help in developing better margin sensing approaches.

The amount of heat released from chemical reactions inside a combustor is a function of the residence time of the flow inside the combustor, due to the finite time required for completion of chemical reactions. The finite chemical rate can be characterized by a chemical time scale. If the heat released within the flow residence time inside a combustor fails to increase reactant energy (temperature) above the minimum

activation energy required for combustion, it gets extinguished. This approach has been used for predicting blowout conditions using well stirred reactor (WSR) models [55]. The two important time scales of the problem are the flow residence time and the chemical time. Dahmkohler number, defined as ratio of flow residence time to chemical time, can typically capture blowout trends. The applicability of well stirred reactor models for swirl combustion requires that reactants are mixed with products, such as combustion in the distributed reaction zone regime [56] of turbulent combustion. It has been speculated that high turbulence levels in the inner recirculation zone and shear layers of a swirl-stabilized combustor result in nearly perfect mixing of reactants and products. Few studies report successful prediction of blowout conditions using well stirred reactor models [14, 57]. In addition, Domkohler number scaling has been reported to be useful in blowout predictions [58, 59]. However, a study by Sloan and Sturgess [60] using well stirred reactors at small scales in a complete simulation, failed to predict flame liftoff and blowout conditions in a non-premixed swirl combustor.

Flame blowout may also occur due to insufficient time for ignition of reactants in the shear layer between a recirculation zone and reactant stream [16, 61, 62].It has been suggested that hot gases in the recirculation zone mix with reactants in the shear layer, auto igniting them, and thus provide a flame stabilization point [63]. If the ignition delay time is large compared to the contact time of reactants with hot gases, blowout will occur. The physics can be scaled using a Damkohler number defined as the ratio of flow residence time to the ignition delay time, for blowout prediction. This methodology has been mainly applied in bluff body stabilized flames.

A third alternative mechanism considers extinction of flames in a turbulent flow. The basis for the approach comes from recent observations that practical combustors typically operate in flamelet or thin reaction zone regimes rather than in the distributed reaction zone regime [64]. Studies employing planar laser induced fluorescence of CH and OH reported clear existence of laminar or thickened flamelets even in highly

turbulent flows [65]. Thickened flamelets are caused by small scale eddies (for example eddies on the Kolmogorov scale), penetrating the preheat zone and transporting cold reactants to it. If the turbulence is high enough, the smallest eddy scales can penetrate the reaction zone and mix products with reactants, creating distributed reaction zones. However, evidence for the existence of distributed reaction zones is rare [64]. Therefore, well stirred reactor models which assume mixing of products with reactants may not describe the controlling physics. An appropriate physical description for blowout should consider extinction of flamelets and subsequent alterations in the flow field leading to blowout.

In a turbulent combustion, local flame extinction occurs due to two processes. The first is straining of flamelets by flame-vortex interactions and the second is quenching by turbulent transport. Medium and large scale eddies in a turbulent flow impose severe flame strains due to wrinkling and shearing of the flame. The strain may cause local extinctions if it is imposed for a sufficiently long time. Flames can withstand instantaneous strain rates, much above the extinction strain rate (obtained from steady state data) if only imposed for a brief period [64]. Another process of flame quenching by turbulence is due to smallest scale eddies penetrating the reaction zone and quenching the flame by transporting cold reactants in to the reaction zone. Such conditions occur if the turbulence intensity is high or the mixture is lean enough, such that the size of small scale eddies is about the thickness of the reaction zone. If the smallest scale eddies could only penetrate the preheat zone, extinction may not occur. By reducing equivalence ratio, extinction strain rate decreases and flame thickness increases, increasing the likelihood of strain extinction and turbulence extinction respectively. By increasing mean velocity turbulence levels usually increase, increasing both strain and turbulence extinction. Of these two extinction mechanisms, strain induced extinction may dominate, as few studies reported local extinction of thin reaction zones before broadening by turbulence [66].

Prior to blowout, local extinctions can randomly occur in a flame, which may grow in size or shrink and may be convected by the mean flow. Though there is no direct interaction between the recirculation zone and the flame during a normal continuous flame sheet, interactions become important when holes appear in the flame sheet. For example, the recirculation zone may help in re-ignition of reactants at the hole locations, restoring the flame. On the other hand, holes allow (cold) reactants into the recirculation zone, which may weaken it. If the rate of supply of reactants into the recirculation zone exceeds their rate of conversion to products , cooling of the recirculation occurs. This would reduce its ability to restore flame along the holes, thereby further increasing the supply of reactants into the recirculation zone. An ultimate condition would be reached when the holes cannot be restored and complete extinction of the flame sheet occurs, leading to blowout.

In a bluff body stabilized flame, Chaudhuri et al. [67] observed that a flame front, which usually envelopes the shear layer during a stable condition, enters the shear layer near blow off. The flame in the shear layer is subject to severe straining by shear layer vortices resulting in local extinctions. Fresh reactants enter the recirculation zone, forming flame pockets which in turn can re-ignite the flame in shear layers. Such extinction and re-ignition processes can happen several times, and complete blowout occurs when the flame pockets fails to re-ignite the shear layer flame. Similar observations were made by Kariuki et al. [68] in a bluff body stabilized flame, where they observed entrainment of fresh reactants into the recirculation zone from downstream, severe local extinctions in the flame front and formation of flame pockets inside the recirculation zone. They observed that total flame blowout occurred when the flame at the bluff body edges was lost.

2.3. LBO Margin Sensing: Previous Work

Local flame extinctions and re-ignitions occur in lean conditions before blowout [69]. However the local extinctions do not lead to immediate and complete flame blowout. Local extinctions can result in large scale unsteadiness in the flame [15, 70]. The extinctions and the associated unsteadiness have been used for detecting the proximity to LBO.

Based on flame partial extinctions, i.e., local extinctions, followed by re-ignition prior to LBO, Thiruchengode [69] sensed approaching LBO in a premixed swirl combustor. He observed intermittent large scale partial extinction of flame in the inner shear layer and its subsequent re-ignition before LBO. The partial extinction and re-ignition resulted in large scale unsteadiness in the flame configuration. A stable flame during nominal combustor operation and a temporary extinction and re-ignition process, observed in high speed flame images are shown in Figure 6. Near LBO, combustor operation is characterized by a stable flame with intermittent extinction and re-ignition events. During an extinction and re-ignition event, there is a large scale flame loss at the bottom of the combustor and most of the fuel is burnt downstream of this region. Frequent occurrence of such events preceded complete flame blowout. Therefore these were called LBO precursor events.

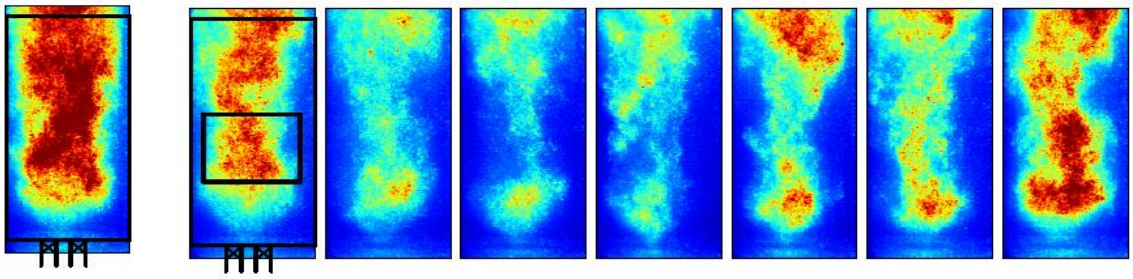

Figure 6. (a) Stable flame during nominal operation (b) Sequence of flame images during an extinction and re-ignition event; image separation 4 ms. (Ref [69])

The precursor events were detected non-intrusively by monitoring flame OH^* chemiluminescence emissions. Sample precursor events in the OH^* optical signal time trace are shown in Figure 7. In the figure, signal features with a conspicuous drop in signal amplitude are precursor events, as extinctions result in a decrease in heat release and the amount of light emitted by species created through chemical reactions. In this previous work, events were detected using a double thresholding approach. An event is declared to start when the signal drops below a first (lower) threshold, and is declared to end when the signal rises above a second (higher) threshold. With a single threshold, inherent noise in the signal can cause the signal to cross the threshold multiple times, causing a single event to be counted as multiple (shorter) events. A minimum event duration constraint was also imposed for more robust event detection. The threshold levels are based on recent signal outputs, i.e., a threshold is given by μ-$\kappa\sigma$, where μ is the time-localized signal mean, σ is the time-localized signal RMS and κ is a constant. Setting the threshold relative to the signal mean makes the event sensing approach less sensitive to "slowly" varying conditions such as engine power and sensor drifts. Making the threshold a multiple of the signal RMS also reduces false event detection that could be caused by combustion or detector noise.

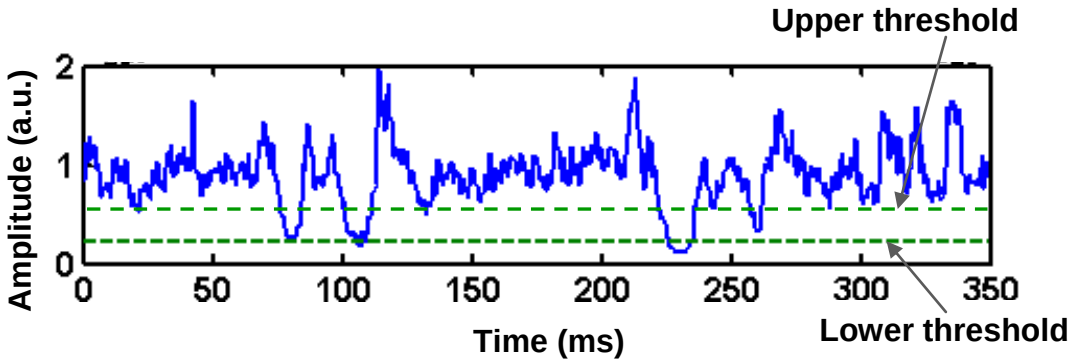

Figure 7. Precursor events in the OH^* optical signal along with thresholds. (Ref. [69])

Results of event identification, with the double thresholding method, time averaged, are shown in Figure 8. The number of events occurring in a given time period,

on average, increase as the combustor gets closer to its LBO limit. Therefore event occurrence rate can be used as a measure of a combustor's proximity to blowout.

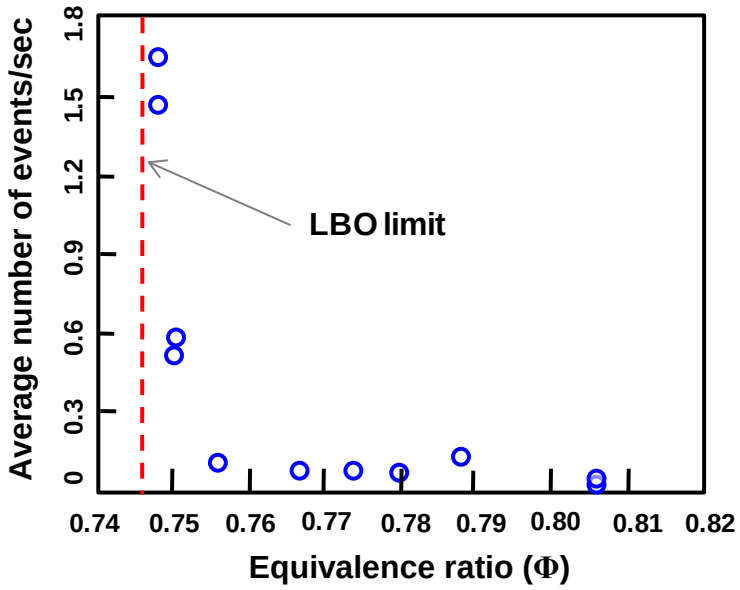

Figure 8. Variation of average number of precursor events with equivalence ratio. (Ref. [69])

In addition to using flame chemiluminescence, acoustic radiation generated by the flame has also been used for LBO margin sensing [71]. Acoustic emission from the combustion process is proportional to the time derivative of heat release rate. During extinction and re-ignition events, the sudden drop and then rise in heat release produces a corresponding acoustic signal. A representative precursor event in the acoustic signal is shown in Figure 9. The time scale of this precursor event feature is ~5 ms. As with optical sensing, acoustic detection allows for non-intrusive sensing with a simple sensor, which is advantageous for practical considerations. Event occurrence rate can be determined either by simple thresholding or by first applying filtering techniques such as a wavelet transformation of the signal using a first order Gaussian wavelet, as this has a similar shape to the precursor event [71].

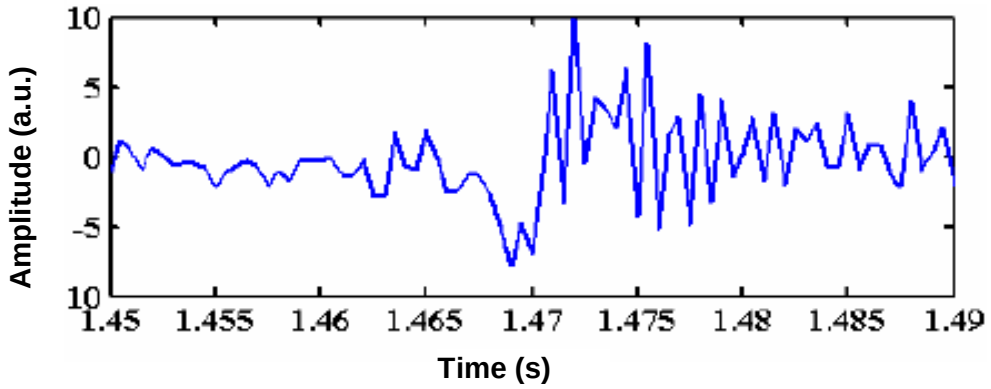

Figure 9. Precursor events in the acoustic signal. (Ref. [71])

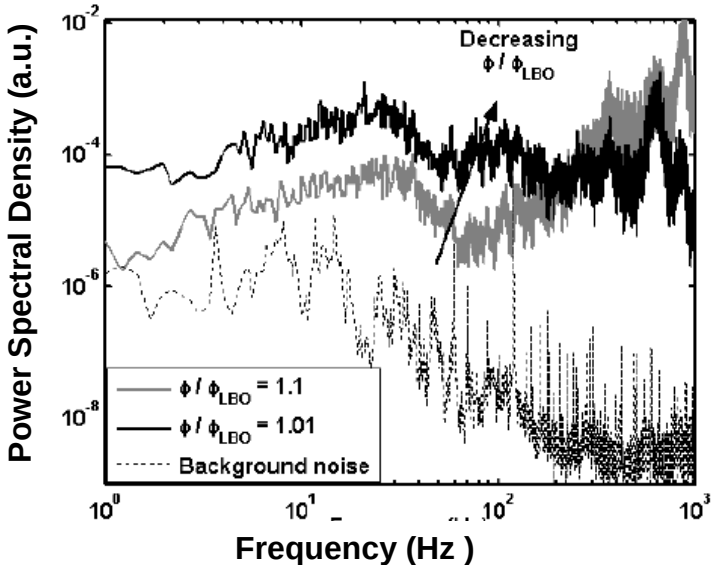

Figure 10. Power spectra of acoustic signals in a premixed swirl combustor. (Ref. [71])

In addition to event identification based methods, spectral methods have also been demonstrated to be capable of LBO margin sensing [23, 69, 71]. The relative spectral power in the low frequency range, e.g., 0-50 Hz, of the optical and acoustic signals was shown to increase near LBO. Precursor events usually have long durations and low occurrence rates. These two factors contribute to a relative increase in spectral power at low frequencies. Thus monitoring of the fractional power in the low frequency range has been suggested as a LBO proximity parameter [71].

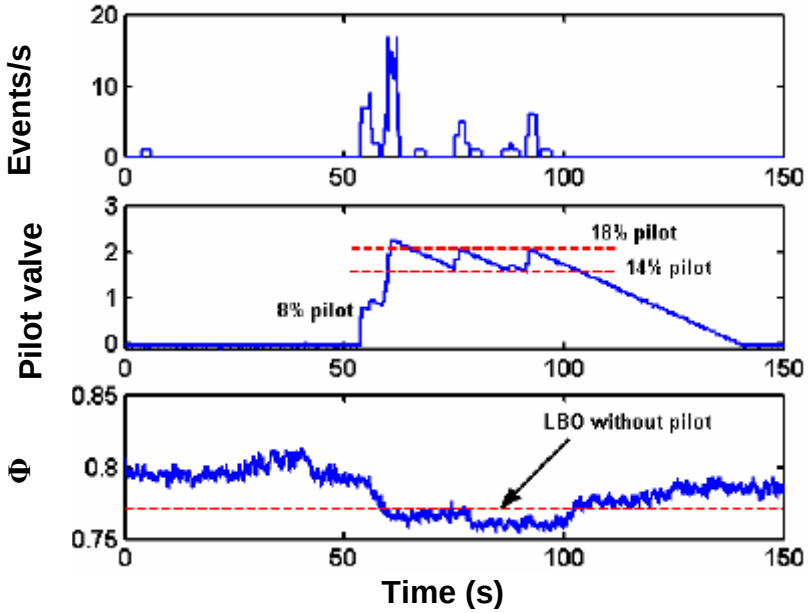

Figure 11. Response of an LBO control system to varying operating conditions. (Ref. [69])

An example of LBO control using precursor event detection is shown in Figure 11 [69] . The control system consists of a pilot fuel valve and responds to precursor event count. Here the combustor equivalence ratio was reduced slowly below its normal LBO limit. However, the event count increased as the combustor got closer to the LBO and the control lsystem opened the pilot fuel valve to stabilize the combustor.

2.4. Combustion Dynamics

Combustor operation in lean conditions, including near the LBO limit, can sometimes include significant levels of dynamic instability. Self-sustained oscillations in pressure and velocity near natural acoustic frequencies of the combustion chamber, produced by closed loop coupling between unsteady heat release and pressure fluctuations, are referred to as dynamic instability. In lean premixed gas turbine combustors, coupling between pressure oscillations and heat release oscillations takes place mainly by flame-acoustic interactions or acoustic-fuel feed system coupling [72]. Flame and acoustic wave interactions involve perturbations in flame area, position or

stretch, resulting in heat release perturbations, which provide feedback to the acoustics. Instability mechanisms involving the fuel feed system result from modulation in fuel flow rate caused by pressure oscillations in the fuel injection/premixing section. Fuel flow rate oscillations result in equivalence ratio oscillations, which get convected to the flame in the combustor resulting in heat release oscillations. It should be noted that an instability mechanism involving equivalence ratio oscillations could simultaneously exhibit flame-acoustic interactions.

2.5. Passive Control of LBO in Aircraft Engines

Current aircraft engines employ a passive control method for avoiding LBO, as the actual LBO limit cannot be determined. The method essentially takes a measure of combustor equivalence ratio and compares it with a predetermined LBO limit. For engines in service, the fuel flow rate can be metered accurately. However, the airflow rate through the combustor is not measured directly [73]. The combustor airflow rate can be estimated using compressible flow properties of the turbine inlet nozzle guide vanes. Flow through the inlet guide vanes is nearly choked over most of the operating range of an engine [74]. Therefore, the mass flow rate of air through the combustor is proportional to $P/\sqrt{T}$ where P and T are the combustor exit static pressure and temperature. Typically, combustor exit static pressure is not measured due to high temperatures. Nevertheless, compressor exit static pressure can be approximated by the combustor inlet static pressure, due to the relatively small pressure drop within the combustor. While the combustor exit temperature can be monitored, the measurement has a slow time response due to heat shielding of thermocouples [75]. However, due to relatively smaller changes in $\sqrt{T}$ compared to P over the operating range of an engine, airflow rate is approximately proportional to compressor exit static pressure. Thus, the ratio of fuel flow rate to the compressor exit static pressure (often denoted as the Ratio Unit, RU) provides a measure

of fuel-air ratio (see Appendix A for the derivation). Engine control systems commonly employ a minimum limit (RU limiter) on this ratio to prevent LBO [75, 76].

The primary function of the aircraft engine control systems is to achieve a desired thrust while keeping the engine with in its safe limits. Since thrust cannot be measured directly, shaft speed is usually taken as a measure of the thrust. The control system varies fuel flow rate (control variable) to achieve the desired shaft speed (controlled variable). The control system architecture consists of a set point controller, to achieve the desired shaft speed, and several protection logic controllers to keep the engine within safety limits. Set point controllers commonly use proportional-integral (PI) control logic, which takes an error in the shaft speed as an input and outputs fuel flow rate. Instead of fuel flow rate, the control systems usually use RU as the control variable due to its better control performance [77]. RU multiplied by the current compressor exit static pressure is commanded as the fuel flow rate for the next time step.

As described in Chapter 1, combustors get closer to LBO limit during power reduction deceleration transients as the fuel flow is reduced without a proportional reduction in the air flow. An engine control scheme during a deceleration transient, along with the acceleration transient, is illustrated in Figure 12. Engines go through deceleration transients when the throttle setting is reduced, demanding a lower speed than the current speed. The negative speed error results in the set point controller commanding a lower RU and moving the engine along the path 1-2. At point 2, the minimum RU limit is reached, and a MAX select strategy chooses the maximum of the fuel flow rates given by the set point controller and the minimum RU limiter. The engine moves along 2-3, until it reaches a point where the set point controller commands a higher fuel flow rate than the fuel flow rate corresponding to the minimum RU limiter. At this point the control switches back to the set point controller and the final desired speed is achieved.

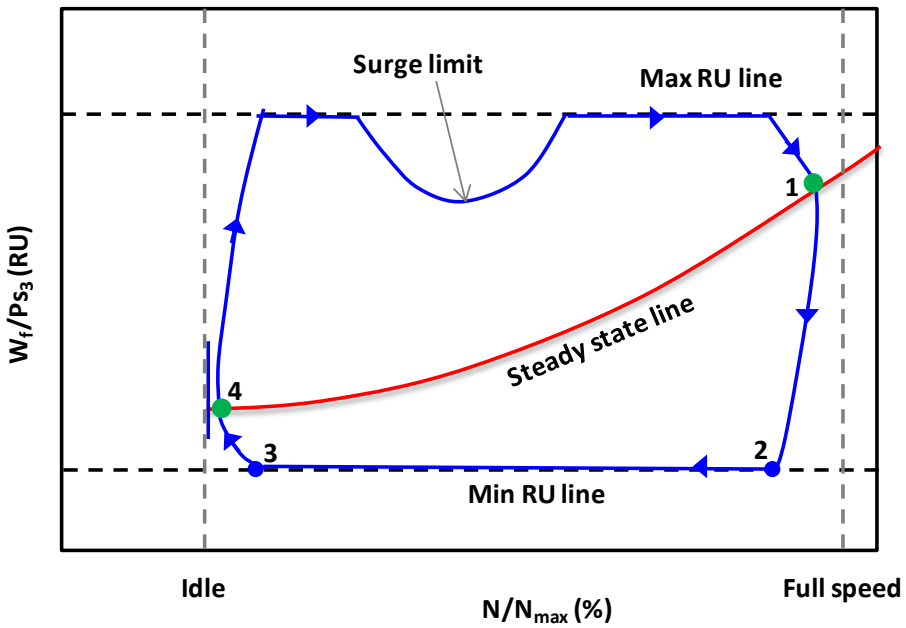

Figure 12. Illustrative engine control schedules during transients. (Ref. [75])

CHAPTER 3

EXPERIMENTAL AND MODELING APPROACHES

This chapter describes the equipment and approaches used to conduct the experiments described in this thesis, as well as the modeling methods employed in the current study. LBO margin sensing is examined in two different types of combustors. The first is a gas-fueled (natural gas) combustor, emulating a single burner in a ground-based gas turbine combustor. The second is a liquid-fueled Lean Direct Injection (LDI) combustor more representative of next-generation low NO_x aeroengine combustors. The first section describes the gas-fueled combustor experiment. The second section describes the liquid-fueled combustor setup. The third section describes the model used to simulate a turbofan engine and control system for exploring the impact of LBO margin sensing on deceleration transient time response.

3.1. Gas-Fueled Combustor Setup

3.1.1. Combustor Design and Flow Facility

In order to study LBO margin sensing in the presence of combustion dynamics, a gas fueled combustor is employed. The combustor is swirl and dump stabilized and operates at atmospheric pressure. A schematic diagram of the combustor setup is shown in Figure 13. Air enters the combustor through a choked valve in order to isolate the air supply from combustor disturbances, specifically pressure oscillations. The air passes through a 22 mm diameter tube, having two axial swirlers with straight blades. The first swirler has a vane angle of 35°, while the second has a higher vane angle of 50°. Thus the theoretical swirl number of the inlet flow is 0.842 [8]. The swirlers are placed 80 mm apart with the second swirler 25.4 mm from the combustor dump plane. Each swirler has an outer diameter of 22.8 mm and a hub diameter of 6.3 mm. The inlet also incorporates a 10 mm diameter (cylindrical) centerbody having a length of 25 mm for enhanced flame

stabilization. The combustor liner is formed by a quartz tube, which can sustain high wall temperatures and permits transmission of ultraviolet (UV) radiation. It has an inner diameter of 70 mm and outer diameter of 75 mm with a length of 600 mm. The quartz tube sits inside a groove made around the combustor inlet, permitting optical access to the entire flame.

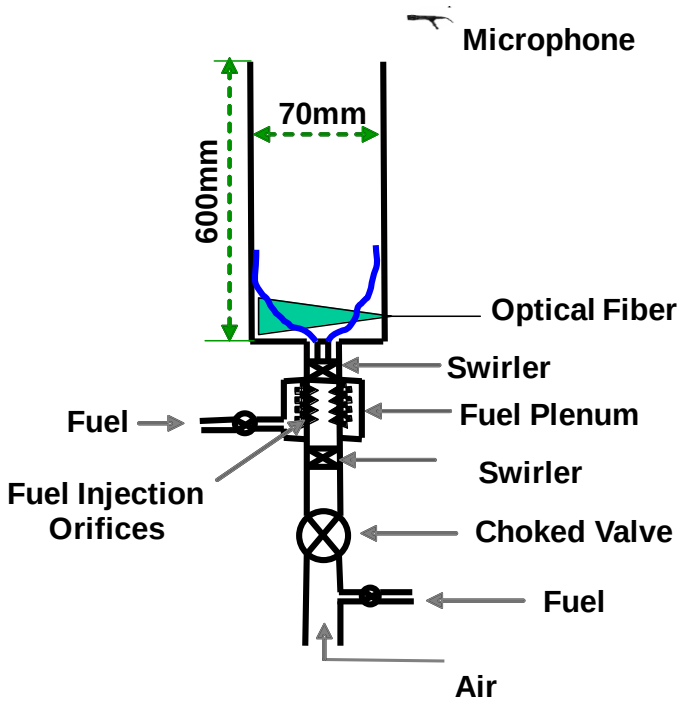

Figure 13. Schematic diagram of the gas fueled combustor setup.

This combustor was used as it can exhibit dynamic instability in lean conditions near blowout. The combustor is configured to have combustion instabilities of two kinds: with and without equivalence ratio oscillations. This is achieved through two types of fuel injection. Gaseous fuel can be injected into the air stream either far upstream before the choked orifice, or after the choked orifice just upstream of the second swirler. By injecting fuel before the choked orifice, pressure perturbations cannot excite fuel-air ratio oscillations. In addition, the large distance between the combustor and the injection location produces well-mixed reactants. In the second method, fuel enters the air stream

between the two swirlers, through multiple injection orifices, none of which are choked. The orifice module has three rows of orifices along the axis with 12 orifices in each row spaced symmetrically around the axis. This arrangement gives a total number of 36 orifices (see Figure 14). The distance between orifice rows is 3.8 mm and each orifice has a diameter of 2.5 mm. The closest row of orifices to the combustor inlet is located 68 mm upstream of the dump plane. The large number of injection orifices is intended to achieve substantial premixing, while still allowing for feedback from combustor oscillations to perturb the fuel flow rate and therefore the incoming equivalence ratio.

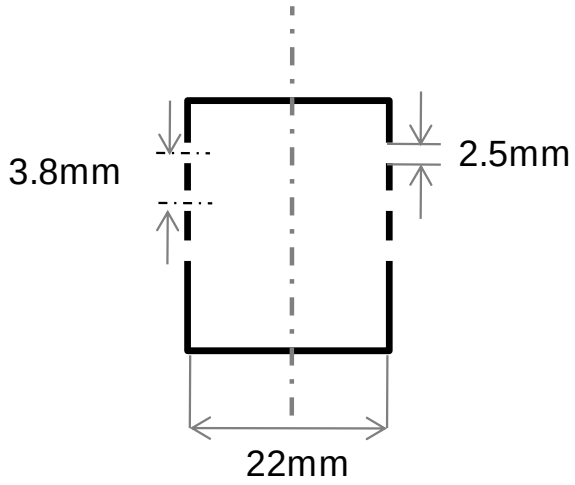

Figure 14. Fuel injection orifice module.

Combustion air flow is delivered from the building air supply line at 250 psig, with a pressure regulator used to ensure a constant supply pressure. Similarly, natural gas comes from the building supply at 125 psig and then passes through a pressure regulator. In cases where methane is used, it is supplied from compressed gas bottles connected to the combustor's standard fuel supply line. A schematic diagram of the flow supply, control and monitoring system is shown in Figure 15. Air and fuel flow rates are measured with rotameters and with pressure gauges monitoring line pressures. For fine control of fuel flow rate during combustor operation near LBO, a rotameter with a resolution of 0.24 SLPM (0.5 SCFH) is used in parallel with the main fuel rotameter,

which has a resolution that is ten times coarser. For the nominal airflow rates used in the experiments, the equivalence ratio resolution is approximately 0.003. The fuel supply line is split into two paths with a three-way valve to rapidly switch between far upstream injection and close injection modes without shutting down the combustor. The nominal average cold flow axial velocity in the combustor is 4.5 m/s, and the nominal combustor power is 32 kW (0.11 MBTU/hr). Based on complete combustion and no heat losses, the bulk average exit axial velocity of the product gases would be 23 m/s.

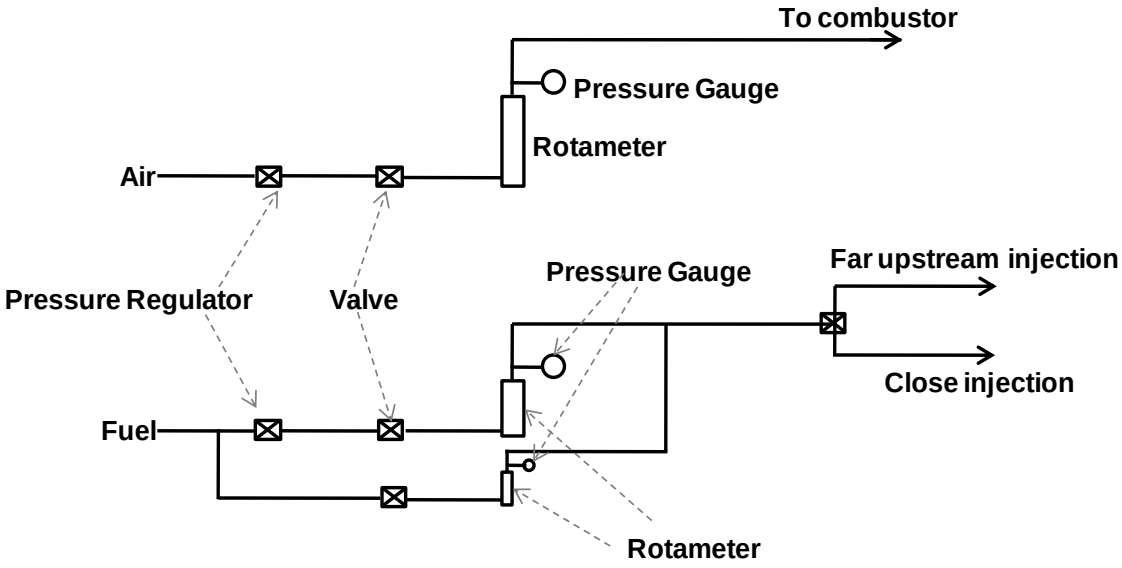

Figure 15. Schematic diagram of fuel and air supply, control and monitoring setups.

The combustor exhibits three distinct flame configurations based on equivalence ratio and flow velocity. The three configurations for different equivalence ratios at a fixed air flow rate (corresponding to a cold flow combustor velocity of 2.5 m/s) are shown in Figure 16. For these images, the combustor was made dynamically stable by reducing the combustor tube length to 300 mm from the standard (600 mm) value, and by employing the far upstream fuel injection mode. However, even during dynamically unstable conditions, the basic flame configurations are essentially the same.

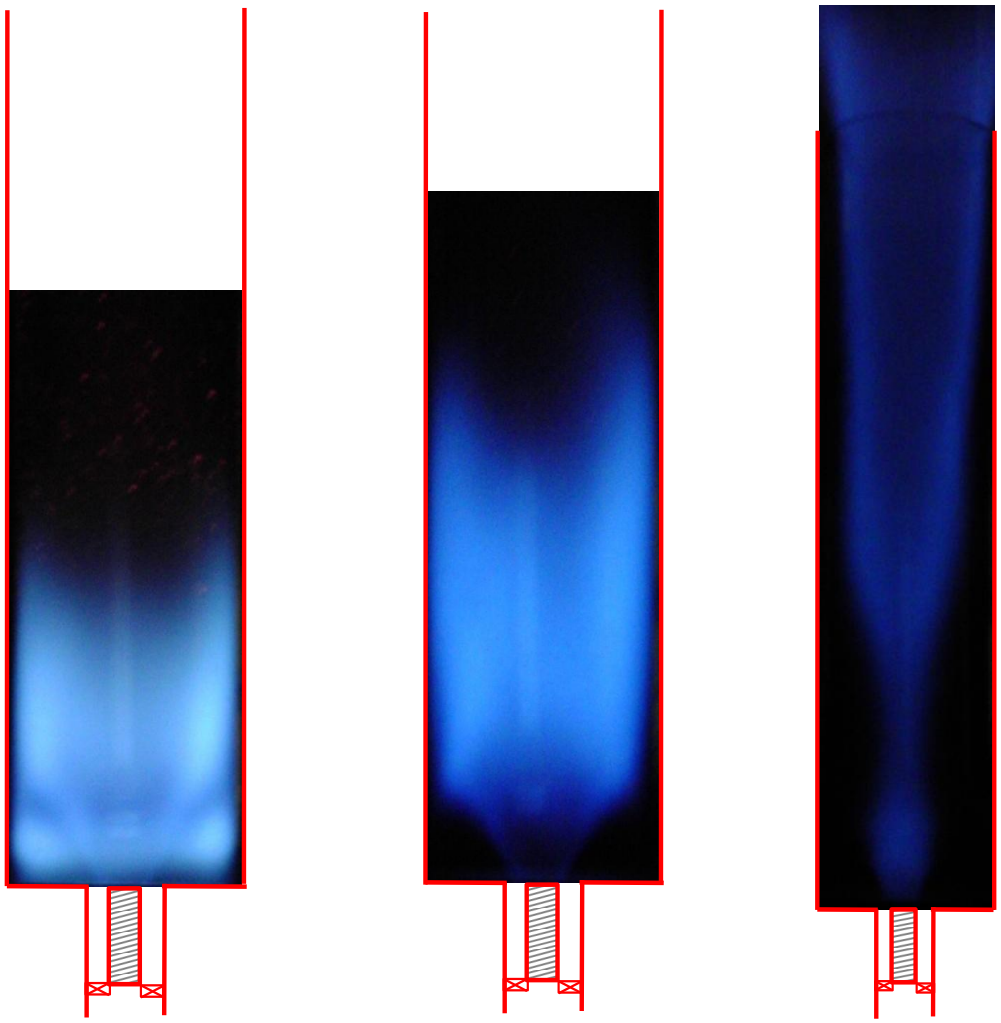

Figure 16. Flame configurations in the combustor for different equivalence ratios at a cold flow velocity of 2.5 m/s: (a) Φ=0.88, (b) Φ=0.79, (c) Φ=0.66.

For equivalence ratios above 0.88, the flame exists in both the inner and outer shear layers as shown in Figure 16(a). In this configuration, the flame is attached (or sits very close) to the centerbody. When the equivalence ratio is reduced slightly below 0.88, the flame in the outer shear layer intermittently extinguishes at a low frequency. When the equivalence ratio is further reduced to 0.79, the outer shear layer flame completely disappears leaving only the inner shear layer flame as seen in Figure 16(b). In this configuration, the flame is longer. By decreasing equivalence ratio further, the flame shifts to the configuration shown in Figure 16(c), where it is quite long and extends

beyond the exit of the combustor. With a sufficiently short tube, e.g., 150 mm, this flame is not stable and blows out. With increasing flow velocity, the equivalence ratios where the configuration transitions occur shift to higher values. Similar flame configurations have been observed in other studies using similar combustor geometries. For example, Muruganandam [69], Bradley *et al.* [49], and Chterev *et al.* [50] reported similar flame configurations.

3.1.2. LBO Sensing and Diagnostics

Optical and acoustic radiation signals are acquired from the combustor along with simultaneous high speed chemiluminescence images. A fused silica optical fiber, with a diameter of 365 μm and a cone angle of 24° was used for collection of optical emissions from the combustor. With the fiber located 60 mm from the center of the combustor, the optical detection region extends across the width of the combustor and 23 mm in the axial direction at the centerline (see Figure 13). The optical radiation first passes through an interference filter centered at 308 nm with a full-width-half-maximum (FWHM) of 10 nm, which corresponds to the primary region of OH^* emission. A miniature metal package photomultiplier (PMT, Hamamatsu H5784-04), with a built-in amplifier, is used to detect the optical signal.

Acoustic radiation from the flame is monitored with a condenser microphone (Bruel and Kjaer type 4939, flat frequency response up to 40 kHz) located 0.30 m above and 0.5 m radially offset from the center of the combustor exit. The output of the PMT and microphone are captured with a National Instruments A/D conversion board using the LABVIEW program.

High-speed flame imaging is also employed to elucidate the flame behavior. The camera is an intensified, high-speed CMOS camera (Videoscope International Ultracam3), capable of taking up to 20,000 frames/sec with variable intensifier gating. The intensifier of the camera has a spectral response from ~200 to 700 nm and hence captures all the visible light from combustion.

3.2. Liquid-Fueled Combustor Setup

3.2.1. Combustor Design and Flow Facility

LBO margin sensing studies for combustor operation at elevated pressure and inlet air temperature are carried out in a liquid-fueled Lean Direct Injection (LDI) combustor. Regarding the appropriate operating conditions, the question of what can be considered realistic operating conditions arises. For example, one can consider ground level (take off) or cruise conditions. A motivating aspect of the current work is low NO_x engines for future supersonic passenger aircraft, which would operate at high altitudes (stratosphere) around 18.2 km (60,000 ft). Even with very high compressor pressure ratios, e.g., 40, combustor inlet static pressures would be between 2-5 atm. Hence in the present work, an LDI combustor operating nominally between 2-5 atm and with an inlet air temperature of ~700 K (800 °F) is used. In addition, LBO is usually a problem at part power operation or near idle where compressor pressure ratios are low. Therefore 2-5 atm is close to the combustor pressure for part power operation at cruise altitudes or idle operation at ground level, for conventional commercial passenger aircraft.

The LDI injector used in the experiments is a single element configuration of a 9-element LDI injector, developed by NASA Glenn Research Center [5]. The 9-element LDI injector is shown in Figure 17. The 9-element injector has nine air swirlers with a fuel injector in the middle of each swirler in a 76.2×76.2 mm^2 overall area. In the present injector configuration, only the center element is present. To partially match the performance of a 9-element injector, the surrounding injectors are replaced by co-flowing air, using a perforated plate.

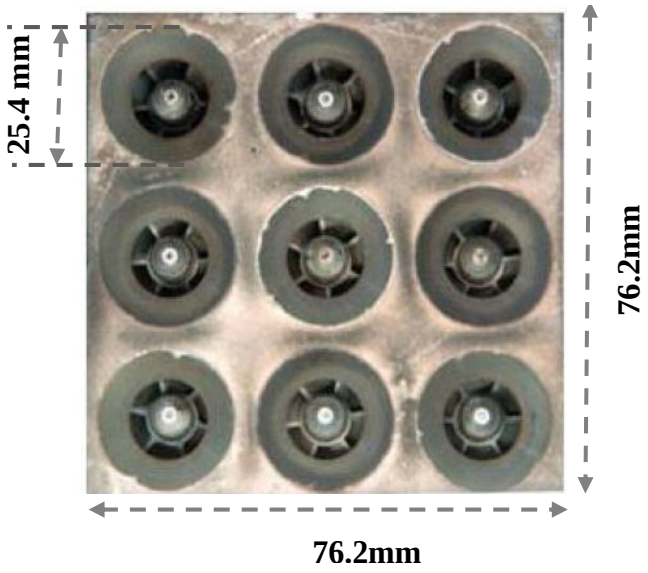

Figure 17. NASA 9 element LDI injector. [5]

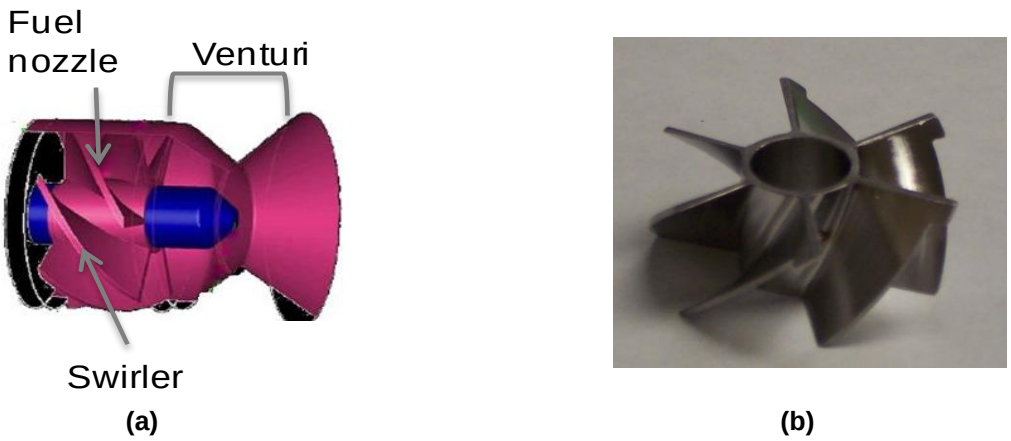

Figure 18. (a) LDI element assembly with venturi, swirler and fuel nozzle. (b) swirler.

An LDI element assembly consisting of a swirler, fuel nozzle and a converging diverging venturi section is shown in Figure 18(a). The swirler has helical axial blades, as shown in Figure 18(b), with a vane angle of 60°. It has an outer diameter of 22 mm and hub diameter of 9.4 mm. Its theoretical swirl number is 1.02 [8]. The swirler is provided with tip protrusions so that it can be mounted inside the venturi firmly, at a known and fixed angular orientation. A cross sectional view of the venturi, with dimensions in millimeters is shown in Figure 19(a). The exit diameter of the venturi is

22 mm. Both converging and diverging sections are inclined at an angle 40° with respect to the axis. A schematic cross sectional view of the fuel nozzle stem is shown in Figure 19(b). It is a simplex type, pressure-swirl atomizer. The nozzle is nominally located slightly behind the venturing throat, and includes a filter in order to prevent any foreign matter from blocking the narrow flow passages, such as the exit orifice. It incorporates an air gap created by a tube with slightly higher inner diameter than the fuel supply tube, in order to prevent fuel coking (as the heated air flows around the fuel nozzle). The minimum required pressure differential across the nozzle is 30 psi in order to produce an acceptable quality spray. The LDI injector was slightly modified from the version supplied by NASA, but performance tests indicated the same spray behavior as the original, unmodified version (see Appendix B for more details).

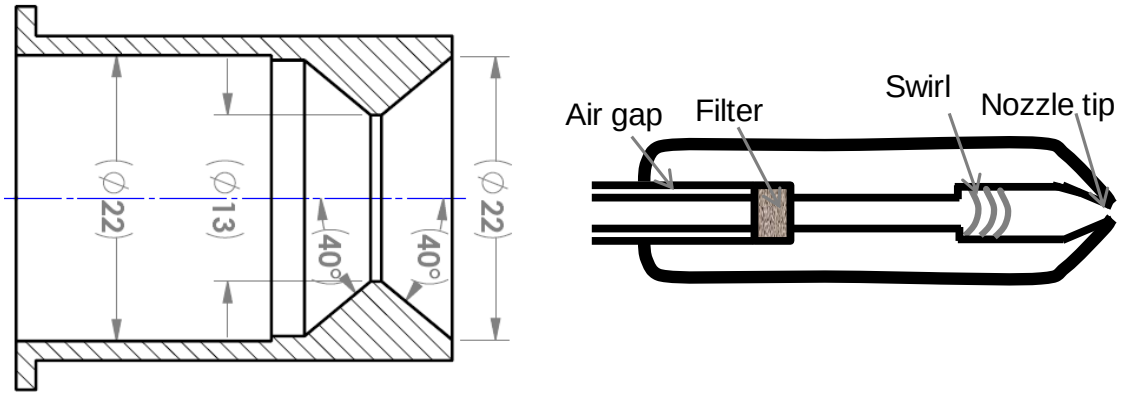

Figure 19. (a) Cross sectional view of converging-diverging venturi section (all dimensions in mm) and (b) fuel nozzle stem cross sectional view.

The single element LDI injector configuration uses co-flow created by a perforated plate around the flow through the LDI element. The co-flow is employed in order to simulate the effect of surrounding elements, absent in a single element configuration. The perforated plate, along with the venturi, is shown in Figure 20. It has 2.38 mm diameter holes spaced symmetrically around the axis, with equal distance

between any two adjacent holes. There are a total of 114 holes, producing an 88% geometric area blockage.

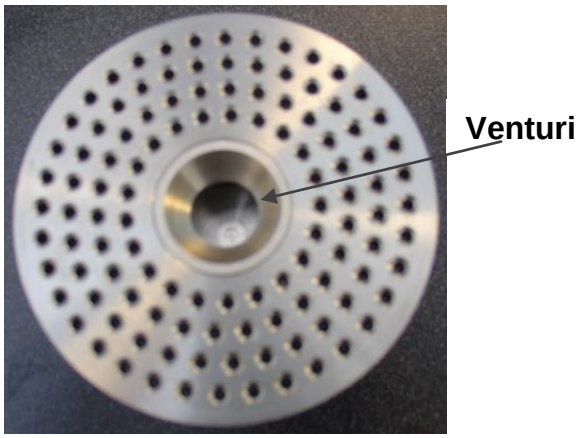

Figure 20. Perforated plate.

A cross sectional view of the single element LDI injector assembly mounted to a quartz combustor liner is shown in Figure 21. Airflow flow through the LDI element and the co-flow are supplied from a common plenum. The airflow split ratio between the two paths is determined by their effective areas. The fuel nozzle is held in a precise position with a nozzle holder connected to the injector casing. The fuel line outer tube, used for creating the air gap, is coated with ceramic lining in order to give additional thermal protection against coking. A hydrogen pilot flame, ignited by a sparking electrode, is used to ignite the combustor. The pilot fuel tube and the igniter electrode are mounted on the injector casing lip as shown in the figure. In order to measure acoustic pressure inside the combustor, access is provided by a 6.35 mm diameter standoff tube mounted on the injector lip. A cylindrical quartz tube with 80 mm inner diameter and 85 mm outer diameter acts as the combustor liner. The quartz liner sits in a groove at the injector lip and is held in place using a metal ring mounted at its downstream end.

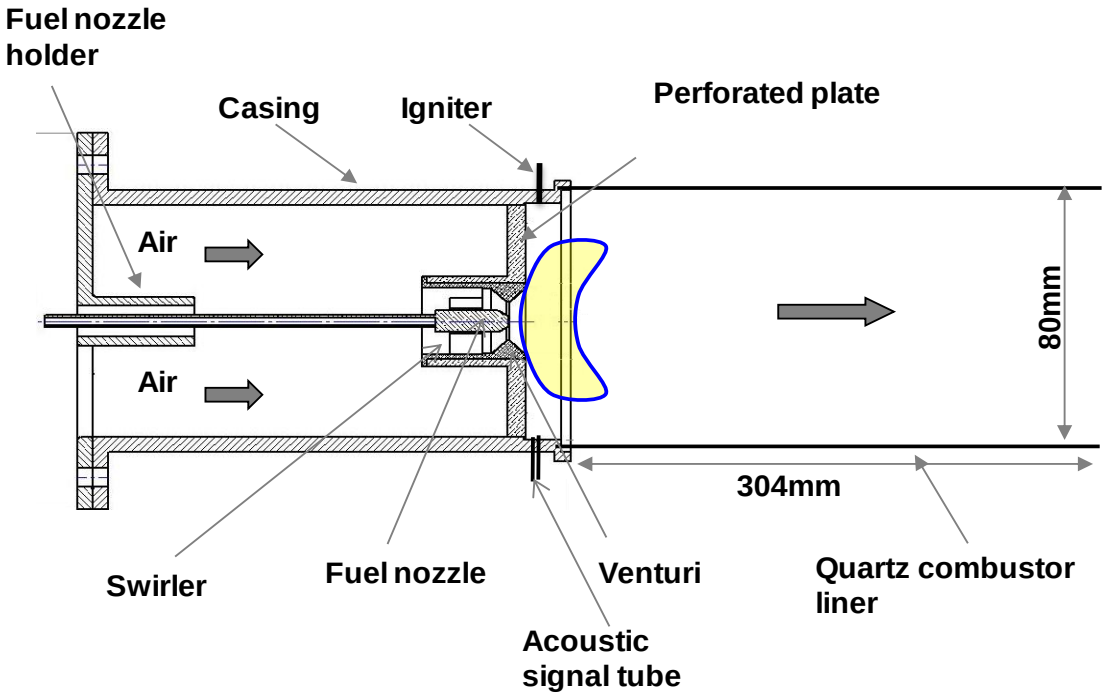

Figure 21. Cross sectional view of the single element LDI combustor.

The LDI combustor is mounted inside a high pressure test rig that can operate up to at least 20 atm. A cross-sectional view of the high pressure test rig with the LDI injector mounted is shown in Figure 22. The pressure vessel takes the high test pressure with no pressure difference across the quartz combustor liner. The vessel has an inner diameter of 0.193 m and a length of 0.495 m. It is equipped with quartz optical windows permitting optical signal acquisition and flame visualization. Cooling air at room temperature passes between the quartz liner and pressure vessel. A gradually converging section is attached downstream with an orifice at the end to achieve pressurization. The test rig is controlled remotely from a control room due to safety requirements.

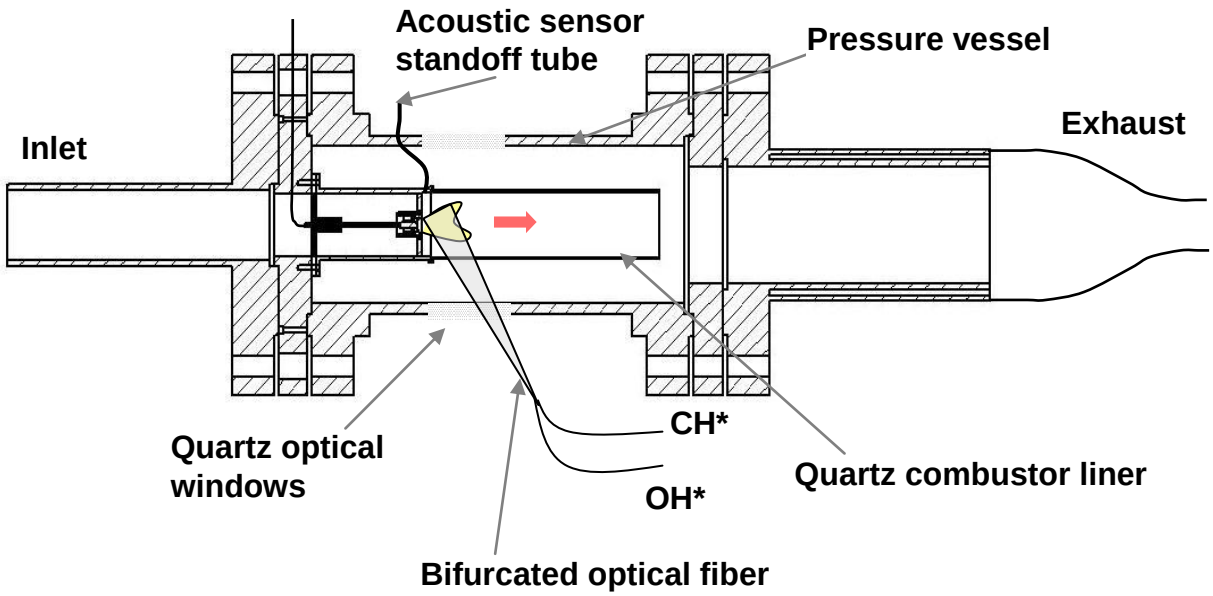

Figure 22. LDI combustor in the high pressure test rig.

A schematic diagram of the fuel supply and control setup is shown in Figure 23. Fuel is pressurized and supplied using a constant displacement fuel pump, with a return circuit for unused fuel. The pump, driven by an electric motor, can pressurize fuel up to 2000 psig. A pressure regulator is used after the pump to reduce the pressure to a required maximum value. A pneumatic actuated valve is used to control the fuel flow. The control valve takes a 4-20 mA signal as input and requires an air pressure between 15-20 psig for actuation. A turbine flow meter (OMEGA Engineering Inc, Model: FTB9502) is used for measuring fuel flow rate. The output of the flow meter is a pulsed signal, with pulse rate non-linearly proportional to flow rate. Hence a linearizing flow computer (OMEGA Engineering Inc, Model: FC-21) is used to convert the non-linear output from the flow meter to a voltage signal that is linearly proportional to flow rate. The flow meter was calibrated for measuring Jet-A by direct measurement of the total fuel volume for a known flow time. In addition to the primary turbine flow meter, the fuel line pressure before the nozzle is also measured in order to provide a second estimate of fuel flow rate (see following paragraph). A solenoid valve located just upstream of the nozzle permits rapid on/off control of the fuel flow. To prevent fuel coking due to residual fuel in the

nozzle and supply tube, a fuel purge system using nitrogen gas is employed. Residual fuel is purged out immediately after fuel to the combustor is turned off. Air mass flow rate through the combustor is measured using a differential pressure orifice meter. Combustor operating pressure and inlet air temperature are measured using transducers mounted on the inlet section of the test rig, just before the combustor.

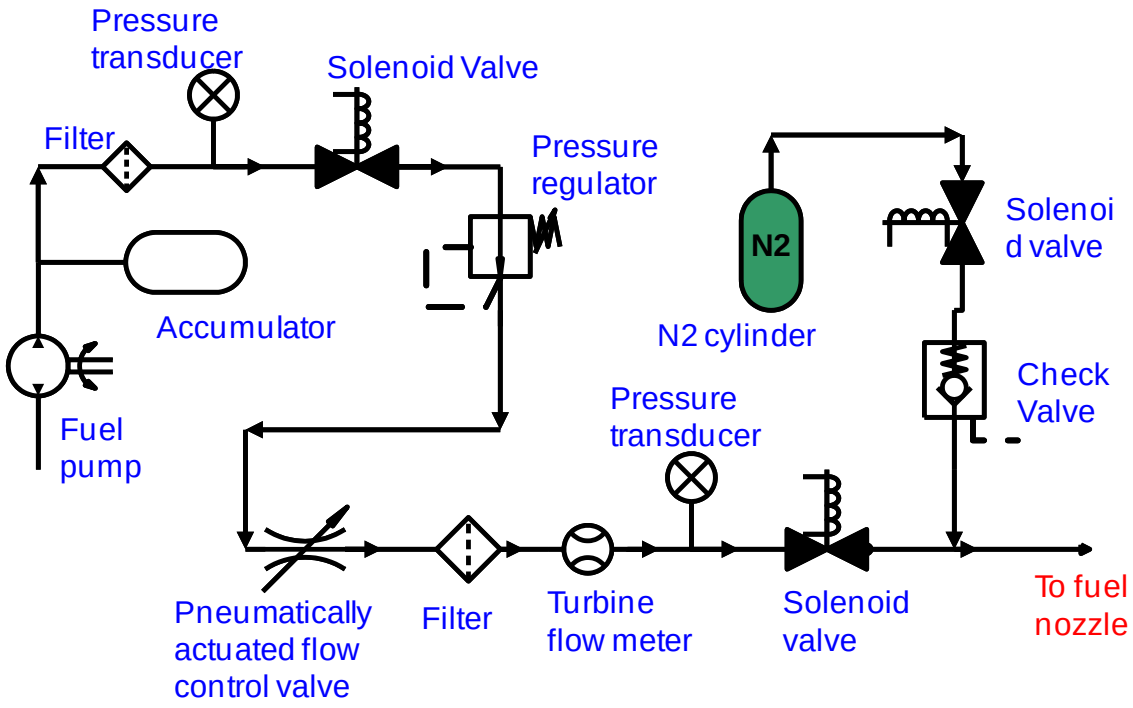

Figure 23. Schematic diagram of fuel supply and control setup.

The fuel nozzle was calibrated to obtain the relationship between its pressure drop and the Jet-A mass flow rate, or essentially its Flow Number (FN) as defined in Eq. (3.1). The experimental results, along with a linear fit, are shown in Figure 24. As expected for an incompressible flow, the flow rate is linearly proportional to the square root of pressure difference across the nozzle. The slope gives FN, with a value of 0.683. This information was used to choose appropriate settings for fuel supply line pressure, and to support the flow rate measured by the turbine flow meter.

$$FN = \frac{\dot{m}(\text{lb/hr})}{\left(\Delta P(\text{psi})\right)^{0.5}} \tag{3.1}$$

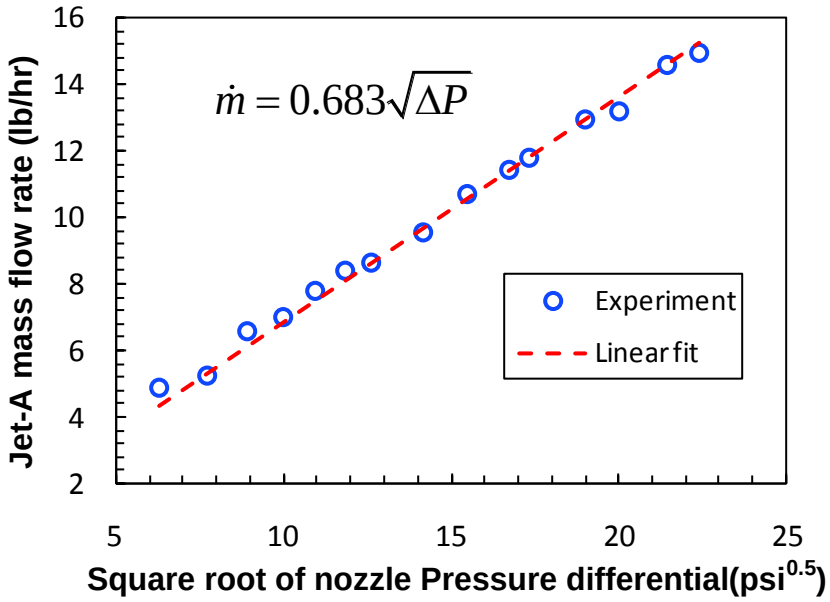

Figure 24. Pressure dependence of fuel nozzle mass flow rate for Jet-A.

The average velocity in the combustor (the quartz tube) in the absence of combustion was in the range 9-15 m/s to match practical engine combustor conditions. For example, combustor velocity is limited to prevent excessive pressure loss due to heat addition, which increases as a function of square of combustor reference velocity [7]. Based on the typical fuel flow rates (1.0-1.76 g/s) employed, the thermal loading of the combustor was between 28 and 74 kW. While the fuel and air flow rates were measured, the combustor equivalence ratio is difficult to define. It is possible that some part of the fuel spray from the central injection region penetrates into the co-flow and burns there. The amount of this fuel cannot be determined easily and the penetration into the co-flow likely varies with operating conditions, e.g., fuel nozzle pressure differential and combustor pressure. Hence, the primary zone equivalence ratios is not known. Therefore only overall equivalence ratios, based on the total combustor air flow, are used here to describe the operating conditions. This is acceptable for the present study, as the actual

flame equivalence ratios are not important; only the combustor's operating stability margin (Φ/Φ_{LBO}) is relevant.

The single element LDI injector is intended to produce a lean, partially premixed flame like the original nine element NASA LDI injector in order to produce low emissions. In addition, when operating as desired, the single element injector should qualitatively reproduce the shape and size of the flame associated with each element of the multi-element injector. As the NASA single-element injector design had not been tested previously, considerable amount of effort was made to test and develop the single element LDI injector in order to meet the performance goals. The efforts were focused on modifying: the flow split ratio between the perforated plate and the LDI element, the co-flow velocity profile, and the fuel nozzle position relative to the venturi throat. More details of the combustor development are given in Appendix C.

The LDI injector is more likely to produce a nearly premixed flame at higher operating pressures where higher fuel flow rates are required, and thus the pressure differential across the fuel nozzle is higher, which results in a finer fuel spray. At relatively lower pressures, and near LBO, the flame might not be as well premixed due to lower pressure differentials across the fuel nozzle. However, the current conditions represent low power, part load operation where LBO is likely an issue.

Flame images obtained with a digital color camera at the end of development process are shown in Figure 25, for combustion operation at atmospheric pressure and elevated pressures. The images show a blue flame indicating low emission operation. In addition, the flame is quite short in length with slightly higher width then the LDI element diameter, indicating adequate confinement by the co-flow.

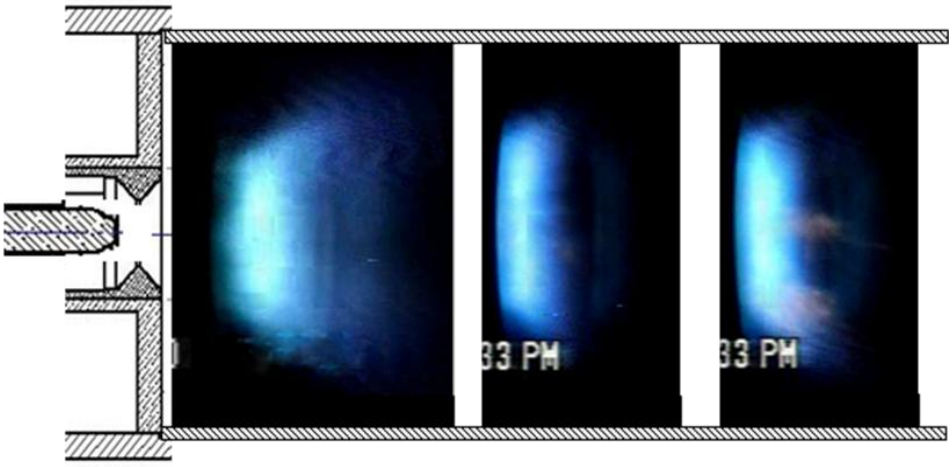

(a) (b) (c)

Figure 25. Flame in the LDI combustor at (a) p=1 atm, v=14 m/s, T= 663 K , $\Phi_{overall}$=0.41; (b) p=2 atm, v=10.6 m/s, T=682K, $\Phi_{overall}$=0.28; and (c) p=4 atm, v=12 m/s, T=733 K, $\Phi_{overall}$=0.23 .

3.2.2. LBO Sensing and Diagnostics

A bifurcated optical fiber with an acceptance cone angle of 32° is used for collection of the optical radiation from the combustor. The fiber is placed nominally at an angle of 45° with respect to the combustor axis, viewing most of the flame (see Figure 22). The collected light is split into two parts by the bifurcated fiber: one part passes through an interference filter centered at 308 nm corresponding to OH^* emission and the other through a 419 nm filter corresponding CH^* emission. The same type of photomultipliers used in the gas-fueled setup is also used here to detect the optical signals.

Acoustic radiation from the flame is monitored with a Kistler piezo-electric pressure transducer. The transducer is side-mounted onto a long (~10 m) standoff tube connected to the combustor.

High-speed flame images are acquired with a CMOS camera (Photron, FASTCAM) fitted with an optical band-pass filter that transmits over a range of ~320-600 nm. A Schott glass (BG 28) filter with a transmission range of ~325-600 nm was

placed in front of the camera lens. The camera views the combustor from a downstream direction, at an angle of about 45° similar to the optical fiber. Images are acquired at a rate of 1000 fps and an exposure of 1 ms, and are synchronized with the optical and acoustic sensor data recording.

3.3. Turbofan Engine Model and Control

In engines, LBO could occur during rapid power reduction (deceleration) transients. When fuel is decreased sharply to reduce power, air flow through the engine drops rather slowly, as compressor speed slowly decreases due to inertia of the rotating turbomachinery. This results in lower combustor fuel air ratios, which could result in flame blowout. To prevent LBO during deceleration transients, current aircraft engine control systems commonly use a passive method which puts a minimum allowed limit on Ratio Unit (RU), defined as *Wf/Ps3*, where *Wf* is fuel flow rate and *Ps3* is combustor inlet static pressure. Due to uncertainly in the LBO limit, the RU limiter is much higher than the actual RU limit where LBO would occur, which limits the transient response. An active LBO margin sensor based on precursor event detection would allow using lower RU limiter, thus improving the transient response.

In order to investigate the possible improvements in transient response along with the limitations in implementing precursor event based active LBO margin sensors, a high bypass turbofan engine, similar to commercial aero engines, is modeled using the Numerical Propulsion System Simulation (NPSS) package. The engine model is similar to the model used in NASA engine control simulation software C-MAPSS40K [76, 78]. The engine model also includes a controller designed for full power to idle transient at sea level static conditions.

3.3.1. High Bypass Turbofan Engine Model

The engine model is a high bypass ratio turbofan engine with two spools producing a maximum thrust of 35,000 lbs at standard sea level static conditions. A

schematic of the engine along with the flow paths is shown in Figure 26. The engine consists of six main components; fan, low pressure compressor (LPC), high pressure compressor (HPC), combustor, high pressure turbine (HPT) and low pressure turbine (LPT). In addition, it consists of an inlet, bypass duct, nozzle and various cooling bleeds. The HPT and HPC are connected through a high speed shaft, whereas the LPT, LPC and the fan are connected through a low speed shaft (fan shaft). For modeling purposes, the fan hub and the LPC are combined together into one unit where the fan hub acts as an additional stage for the LPC. Flow through the fan tip passes directly in to the bypass duct.

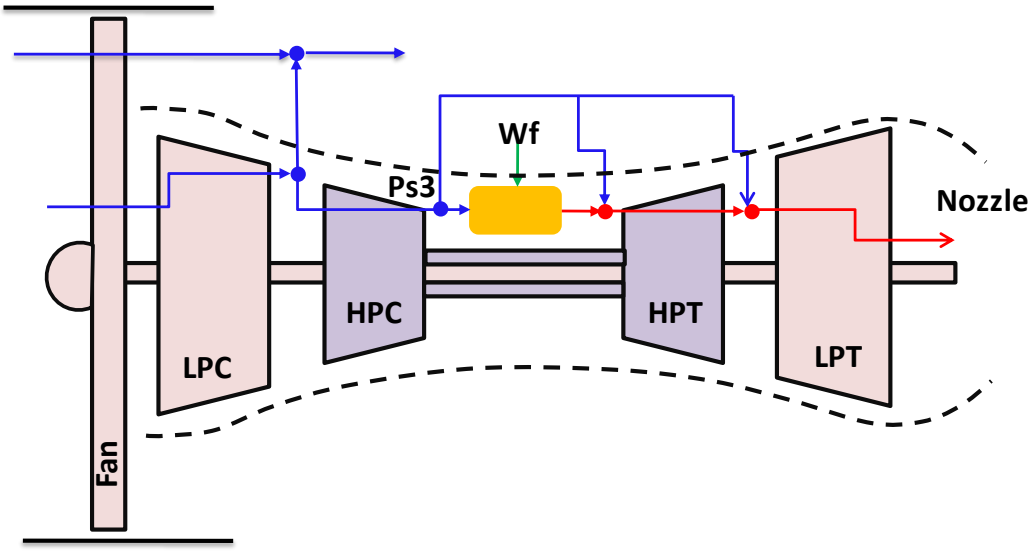

Figure 26. Schematic of the simulated turbofan engine with flow paths.

The engine model is implemented in NPSS. The model is a zero-dimensional, physics-based component level model. The model essentially computes output properties of each component using inputs (pressure and temperature) at a given a mass flow rate. The five turbomachinery components are characterized by their maps relating pressure ratio, corrected mass flow rate and adiabatic efficiency, which are parameterized with corrected shaft speeds. The combustor is characterized by its combustion efficiency and

pressure drop. Various flow ducts are characterized by their pressure losses. The model requires design point specifications for calculating engine performance at off-design operation.

The design point for the engine is considered to be full power operation at sea level static conditions (Altitude=0, Mach number=0). The specifications for various components at the design point are given in Table 1. Maps for the five turbo machinery elements are taken from the example maps provided with NPSS.

Table 1. Design point specifications of the turbofan engine.

Component	Parameter	Value
Fan	Pressure ratio	1.66
	Bypass ratio	5.53
	Efficiency	0.86
Low-pressure compressor	Pressure ratio	2.37
	Efficiency	0.87
High-pressure compressor	Pressure ratio	12.22
	Efficiency	0.85
High pressure turbine	Pressure ratio	4.42
	Efficiency	0.87
Low pressure turbine	Pressure ratio	3.84
	Efficiency	0.89
Combustor	Fuel flow rate	3.62 lbm/s
	Efficiency	0.98
Low-speed shaft (fan shaft)	Inertia	106 lbf-ft^2
	Rotational speed	4039 rev/min
High-speed shaft	Inertia	21.5 lbf-ft^2
	Rotational speed	11868 rev/min
Inlet	Airflow rate	104 lbm/s

3.3.2. Engine Control

The engine controller is primarily designed for thrust reduction from full power to idle, and implemented in NPSS. Power lever angle (PLA) position (80°: full power - 40°:

idle) is given as an input to the controller and it is converted to fan shaft speed demand. The PLA position is mapped linearly to thrust, whereas it is non-linearly mapped to the shaft speed, as the shaft speed and thrust are not linearly related. The fan shaft rpm is controlled to achieve a desired thrust by varying the fuel flow rate. The control system architecture is shown in Figure 27. The system consists of a proportional-integral (PI) controller to achieve desired shaft speed. The PI controller takes error in shaft speed as input and outputs the required change in RU. RU is used as the control variable as it is the common control variable in engines. RU is multiplied by the current value of *Ps3* to obtain the required fuel flow rate. To prevent LBO during deceleration, an RU limiter is employed similar to conventional engine control systems. The limiter is a constant and not scheduled. The maximum of the fuel flow rates given by the PI controller and the RU limiter is commanded to the fuel actuator.

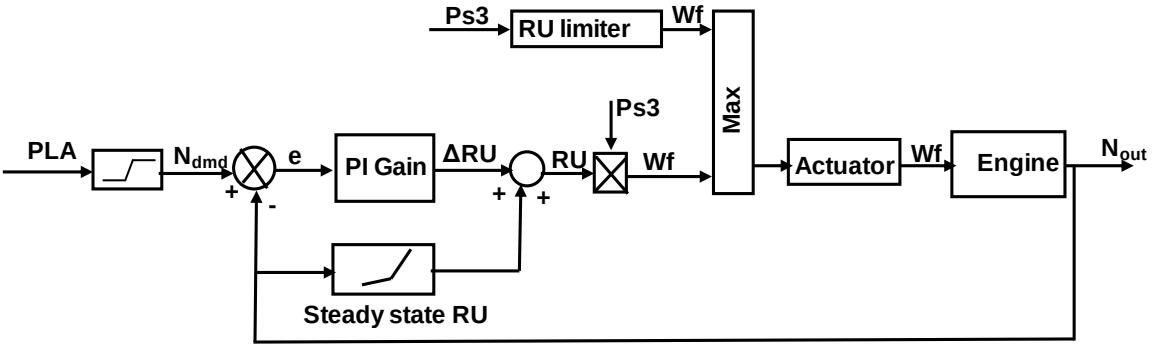

Figure 27. Architecture of the engine control system.

Turbine engines are highly non-linear systems from control perspective, as they behave differently at different operating points. However they can be considered linear in a limited range around an operating point [77]. This allows a set of simplistic linear controllers (e.g., PI) to be used for controlling non-linear engine systems. The control usually requires scheduling and interpolation of control gains each set tuned for a specific

operating point. Since only a rapid transient is considered, only two sets of gains, one near full power and the other near idle, were found to be adequate for the current study.

The PI control gains were tuned such that rapid time response is achieved without considerable overshoot. This was achieved by obtaining a transfer function from RU to shaft speed using system identification process in MATLAB. A chirped fuel input signal was given to the engine and its shaft speed response was obtained in order to estimate the transfer function. The transfer function is assumed to be second order and given by Eq. (3.3). The parameter values of the transfer function are given in Table 2. Using the engine transfer function, PI controller gains were tuned in MATLAB to produce optimal control response. The gains at full power are K_p=6.2 lb/s/psi, K_i=12.3 lb/s/psi/s and at idle K_p=23.5 lb/s/psi, K_i=9.62 lb/s/psi/s, where K_p is the proportional gain and K_i is the integral gain (Eq. (3.2)). The actuator transfer function is assumed to be the first order response given by Eq. (3.4) with K_e=1 and T_{p1}=0.02 s.

$$U = K_p e(t) + K_i \int_0^t e(\tau) d\tau \tag{3.2}$$

$$G(s) = \frac{K_e (1 + T_z s)}{(1 + T_{p1} s)(1 + T_{p2} s)} \tag{3.3}$$

$$A(s) = \frac{K_e}{1 + T_{p1} s} \tag{3.4}$$

Table 2. Engine transfer function parameters at full power and idle

Operating point	***K_e (rpm/lb/s/psi*10^{-3})***	***T_z(s)***	***T_{p1}(s)***	***T_{p2} (s)***
Full power	0.117	0.391	1.03	0.535
Idle	0.12	0.362	1.83	0.910

During the deceleration transient control when the RU limit is reached, control switches from the PI controller to the RU limiter. Since the PI control would be inactive when the limiter is on, the integral error term keeps accumulating due to the integration action, and is known as an integral windup problem [77]. The integral windup results in excessively large outputs which fails the PI controller. Integral windup protection is usually employed to reduce the integral error when the PI controller is not active. In the present controller, windup protection was implemented by modifying the integral error term using Eq. (3.6), where e_w is the error between RU commanded to the engine and RU calculated by the PI controller (3.5). A value of 3.0 lb/s/psi/s for K_w was observed to produce the desired results.

$$e_w = \left(RU_{out} - RU_{PI} \right) \tag{3.5}$$

$$\text{intErr} = \int_0^t \left(e + \frac{K_w}{K_i} e_w \right) dt \tag{3.6}$$

3.3.3. Example Control Results

Example control results for full power to idle transient, initiated at t=1 s by moving the throttle angle from full power (80°) to idle (40°) are shown in Figure 28. The time step between successive simulation runs was 10 ms. The RU limiter is taken to be 15.12 lb/hr/psi, which is slightly below the steady state idle RU of 17.6 lb/hr/psi. From the thrust response, it can be seen that the control produces a smooth transition to idle without any undershoot, taking up to 7 s to reach idle.

The controller decreases fuel flow rapidly at the beginning and thereafter slowly decreases it, governed by the rate at which the air flow rate (i.e., *Ps3*) drops. From the RU limiter on/off plot, the limiter comes on within 150 ms after the transient initiation and stays on for 4.7 s. Therefore most of the deceleration is achieved while keeping the RU at the minimum limit. From the RU plot, RU is maintained constant during the time when

RU limiter is on, and starts to increase when the engine is sufficiently slowed down in order to match the final desired speed. The equivalence ratio is calculated by assuming 27% of the flow through the combustor passes through the primary zone.

This well-behaved simulation of the aeroengine, including the controller, is used to provide the basis on which the LBO margin sensing approach is tested for its applicability to control of rapid engine transients in Chapter 6.

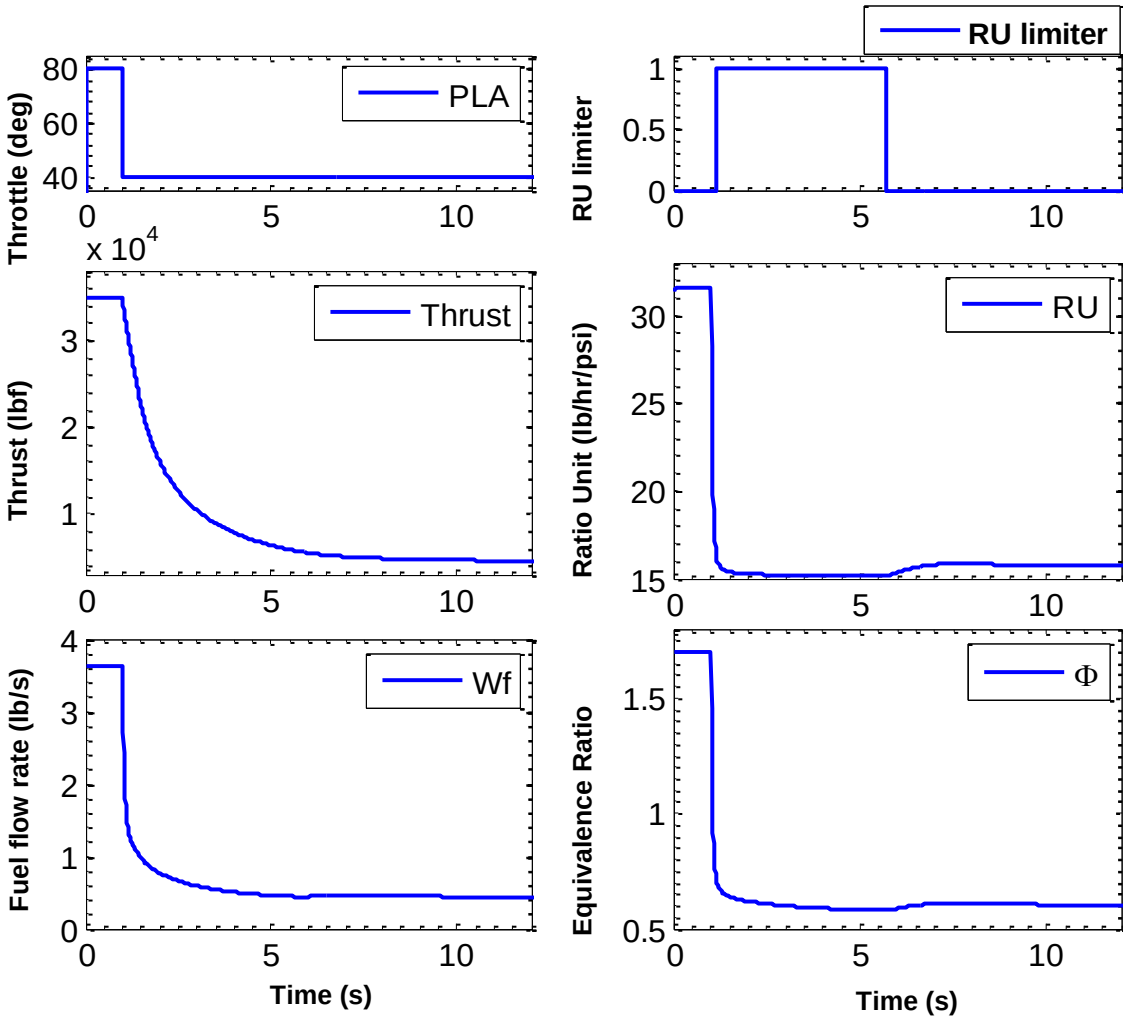

Figure 28. An example full power to idle transient starting at t=1 sec.

CHAPTER 4

LBO MARGIN SENSING: OPTICAL DETECTION

This chapter details results for LBO margin sensing based on analysis of optical emissions. The margin sensing approach is mainly by detection of flame partial extinction and re-ignition events occurring near LBO in flame chemiluminescence signals. Results are presented for combustors operating under dynamically unstable conditions, and at elevated pressure and temperature. Section 4.1 covers LBO margin sensing under dynamically unstable conditions in a gas-fueled combustor. Section 4.2 describes margin sensing at elevated pressure and inlet temperature in a liquid-fueled LDI combustor. The final section summarizes the results.

4.1. LBO Margin Sensing in the Gas-Fueled Combustor

LBO margin sensing under high amplitude dynamic instability is investigated in a gas fueled combustor that can produce instability through at least two distinct mechanisms: instability without equivalence ratio oscillations (w/o Φ') and instability with equivalence ratio oscillations (w/ Φ'). Heat release oscillations for instability w/o Φ' are mainly due to flame-vortex interactions, whereas both flame-vortex interactions and equivalence ratio oscillations contribute to heat release oscillations in the case of instability w/ Φ'. The study was focused on these two mechanisms, as they are the two main instability mechanisms in lean premixed combustors [72]. Besides the dynamically unstable conditions, results from dynamically stable operation are also presented in order to compare them with the unstable conditions. The combustor is described in Chapter 3. For the dynamically unstable experiments all operating conditions were identical, except for the fuel injection location. For examining combustor behavior as it approaches LBO, air flow rate was kept constant and fuel flow rate was reduced. Average cold flow

velocities were 4.2 m/s and the equivalence ratios where blowout occurred were: 0.688 for dynamically stable operation, 0.678 for instability w/o Φ′, and 0.694 for instability w/ Φ′. OH* chemiluminescence signals were recorded for a period of 30 s at each operating condition.

4.1.1. Instability Characteristics

In order to study LBO margin sensing under dynamically unstable conditions, a significant level of dynamic instability in lean conditions including near LBO is required. The current combustor meets this requirement by exhibiting pronounced dynamic instability in lean conditions, over a wide range of equivalence ratios, including very close to blowout, for both kinds of instability mechanisms. The dynamic instability of the combustor is characterized in Figure 29, which shows acoustic signals recorded by a microphone outside the combustor. Signals are shown for the combustor operating near LBO for each of the fueling cases (w/ and w/o Φ′). For the two cases, all combustor operating conditions are identical except for the fuel injection location. Both signals clearly exhibit periodic oscillations without much noise, illustrating the existence of pronounced dynamic instability near LBO. In addition, the sound pressure level outside the combustor at the microphone location is about 130dB. Though not measured, the pressure level inside the combustor would be much higher. A clear difference between the two traces is the presence of strong amplitude modulations for instability w/ Φ′. In addition, the dynamic instability is more pronounced w/ Φ′, as indicated by the higher peak-to-peak amplitudes compared to the w/o Φ′ trace.

Power spectra corresponding to the acoustic signals of Figure 29 are shown in Figure 30. The spectra are obtained by ensemble averaging multiple spectra each having a resolution of 0.3 Hz (data were recorded for 30 sec and broken into 3 sec segments). Most of the acoustic power emitted is emitted in a relatively narrow region, with very low power due to broadband combustion noise. The instability peaks are located at 265 Hz

(w/o Φ') and 245 Hz (w/ Φ'). These frequencies are close to the axial quarter wave acoustic mode frequency of the combustor. Assuming a bulk uniform product temperature of 1000 K, the quarter wave mode frequency is 263 Hz. The instability frequencies are slightly different and in addition, instability w/ Φ' has a broader peak, which corresponds to the significant amplitude modulation seen for that case. In addition the broad peak suggests that the amplitude modulations are not periodic. If they were periodic, a clear second peak in the spectrum should be evident.

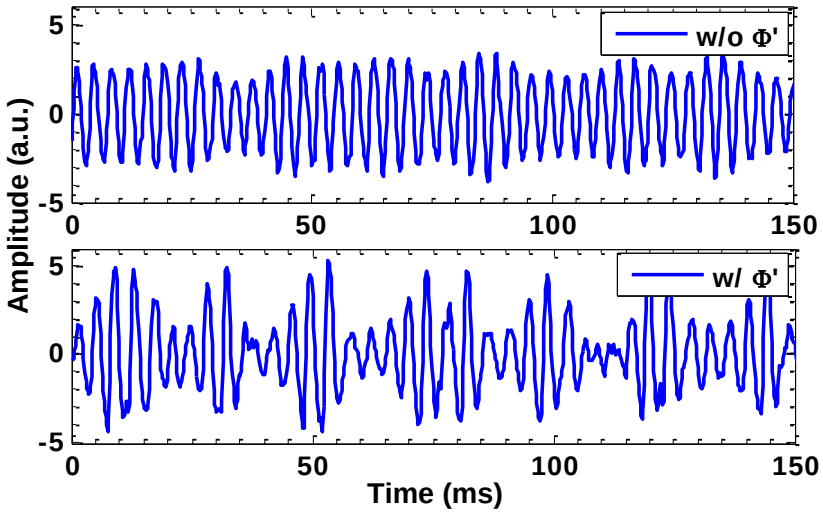

Figure 29. Acoustic signal time traces for combustor operation near LBO, at Φ=0.71 for instability w/o Φ′ Φ=0.72 for instability w/ Φ′.

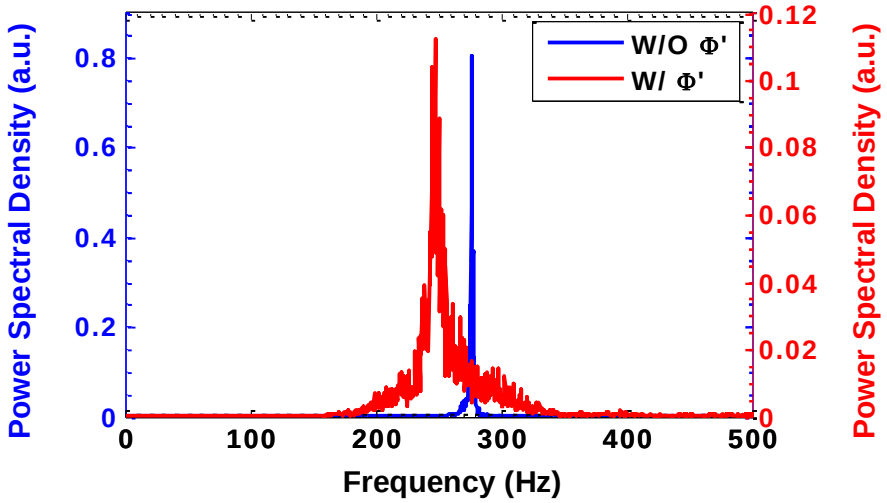

Figure 30. Power spectra of acoustic signals for combustor operation near LBO at Φ=0.71 for instability w/o Φ′ Φ=0.72 for instability w/ Φ′.

Based on these results, it can be concluded that the instability characteristics are noticeably different for the two fueling methods. The disparities provide evidence that fueling the combustor just upstream of the final swirler does add complexity and modifies the instability mechanism, adding equivalence ratio variations.

4.1.2. LBO Precursor Events

In previous LBO approach detection studies in a premixed swirl combustor, the flame was observed to exhibit partial extinction and re-ignition events near LBO. These events, called LBO precursor events, were observed to occur more often as the combustor's stability margin (Φ-Φ_{LBO}) was reduced, thus providing a measure of combustor's proximity to LBO. The LBO approach detection with event identification provides better time response compared to other approaches such as low frequency spectral content estimation or standard deviation estimation, due to finite time required for their evaluation. Therefore the present study focused mainly on the LBO precursor event identification approach. As described in Chapter 2, precursor events in optical (chemiluminescence) signals are characterized by a drop in signal amplitude from the time of extinction to the time of re-ignition.

Before examining optical LBO precursor events under dynamically unstable conditions, an example precursor event under dynamically stable conditions is shown in Figure 31. The combustor was made dynamically stable by using a shorter tube with a length of 300 mm instead of the standard 600 mm tube. Shortening the tube length increases the natural frequency of the (longitudinal) acoustic mode, to ~530 Hz. For this case, fuel was injected far upstream. The resulting chemiluminescence signal shown in Figure 31 was acquired from a region of about the combustor diameter in length above the combustor inlet. The signal does not exhibit sinusoidal oscillations. There is evidence of some low amplitude, quasi-periodic fluctuations with a period of ~25 ms. The amplitude is only a few times greater than the level of the combustion noise. However,

the corresponding frequency, 40 Hz, does not coincide with the natural frequency of the combustor based on the combustor's length. Based on these observations, we denote this mode of operation as dynamically stable, especially in comparison to the other cases where dynamics were very strong. The local mean amplitude of the signal starts to drop at around 100 ms and takes about 50 ms to recover. This feature is similar to precursor events observed in earlier studies, under dynamically stable conditions, in a premixed swirl combustor with a slightly different geometry [69].

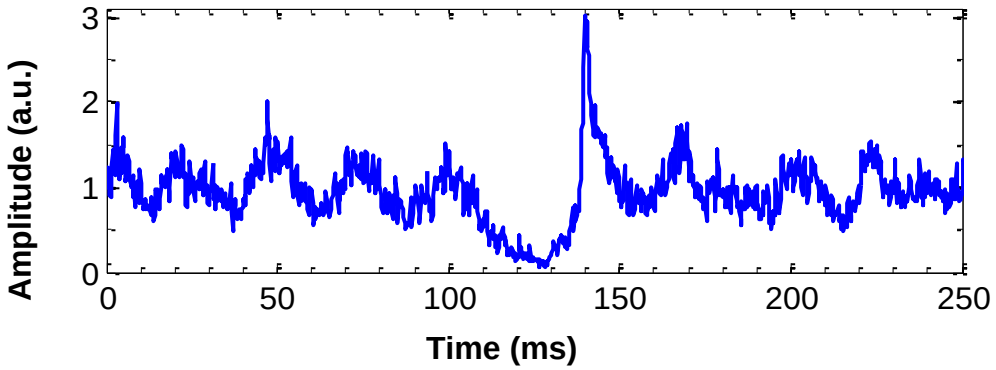

Figure 31. OH^* chemiluminescence signal time trace with a precursor event occurring between 100-150 ms for dynamically stable operationat Φ=0.704.

Figure 32 shows OH^* signal time traces during dynamically unstable operation, near LBO, for instability w/o Φ' and w/ Φ'. For instability w/o Φ', there are usually large amplitude modulations due to the instability, and the minima of the oscillations are well above zero. Between 130-160 ms, there is a precursor-like feature characterized by a large drop in signal amplitude for a duration of about 30 ms. During this period, amplitude modulations are diminished and resume only after complete re-ignition, i.e., after the apparent precursor event has ended. The signal behavior during this period is somewhat similar to the precursors in dynamically stable conditions. Also this type of characteristic signal feature was observed only when the combustor was operating near LBO, indicating that they are indeed LBO precursors.

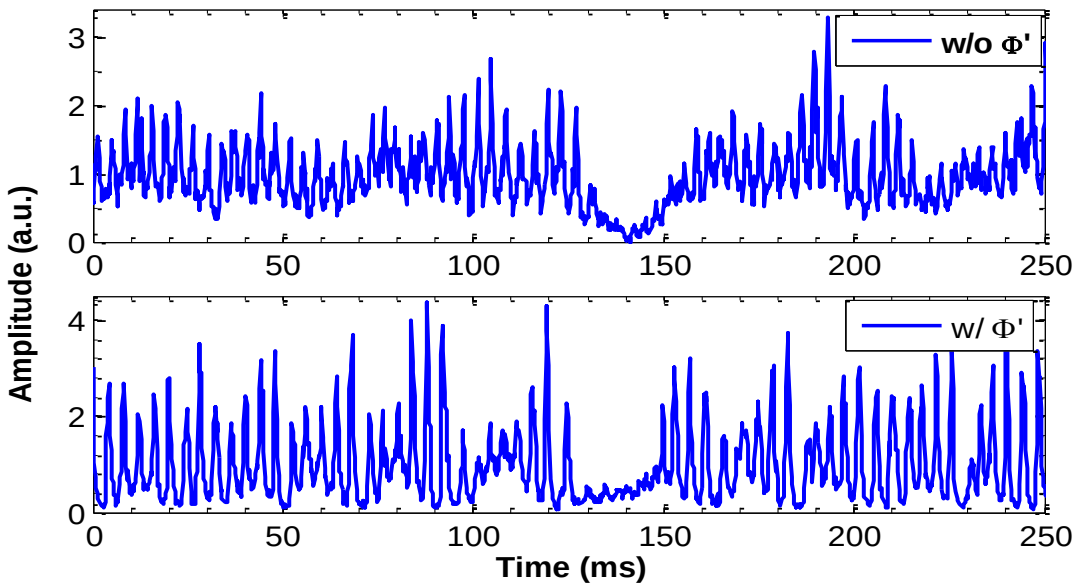

Figure 32. OH* signal time traces with precursor events for dynamically unstable operation w/o Φ' and w/ Φ'. Mean equivalence ratios: 0.698 (w/o Φ'), 0.714 (w/ Φ').

Unlike the w/o Φ' mode, instability w/ Φ' has amplitudes dropping to zero during each instability cycle (see Figure 32), independent of whether the combustor is operating near LBO. Thus low amplitudes (optical signals near zero) alone cannot be taken as an indication of proximity to LBO. However there are other instances in the signal that could be precursor events. For example between 125-150 ms, there are no amplitude modulations, and the local signal mean stays well below the normal (long term) mean of the signal. Such events were observed only close to LBO, indicating that they are precursors. The event has a duration of about 25 ms, similar in time scale to the precursor for instability w/o Φ'. As the two events look qualitatively different, the event identification analysis would require different strategies for the two modes of operation.

High speed flame chemiluminescence imaging was carried out in order to examine the flame behavior near LBO during precursor events. High speed images during combustor operation near LBO, for instability w/o Φ' are shown in Figure 33. Images were captured at 1900 frames/s with an exposure time of 200 μs for each frame. Grayscale images were scaled with intensity based color maps, as indicated in the figure.

An outline of the combustor is superimposed on each image. The images are broadband chemiluminescence images without any spectral filtering. The images in the top row of the figure correspond to normal combustor operation, while the bottom row images correspond to a precursor event, similar to the one in Figure 32. Both image sequences are from the same run, with the bottom row sequence starting 200 ms after the end of top row sequence.

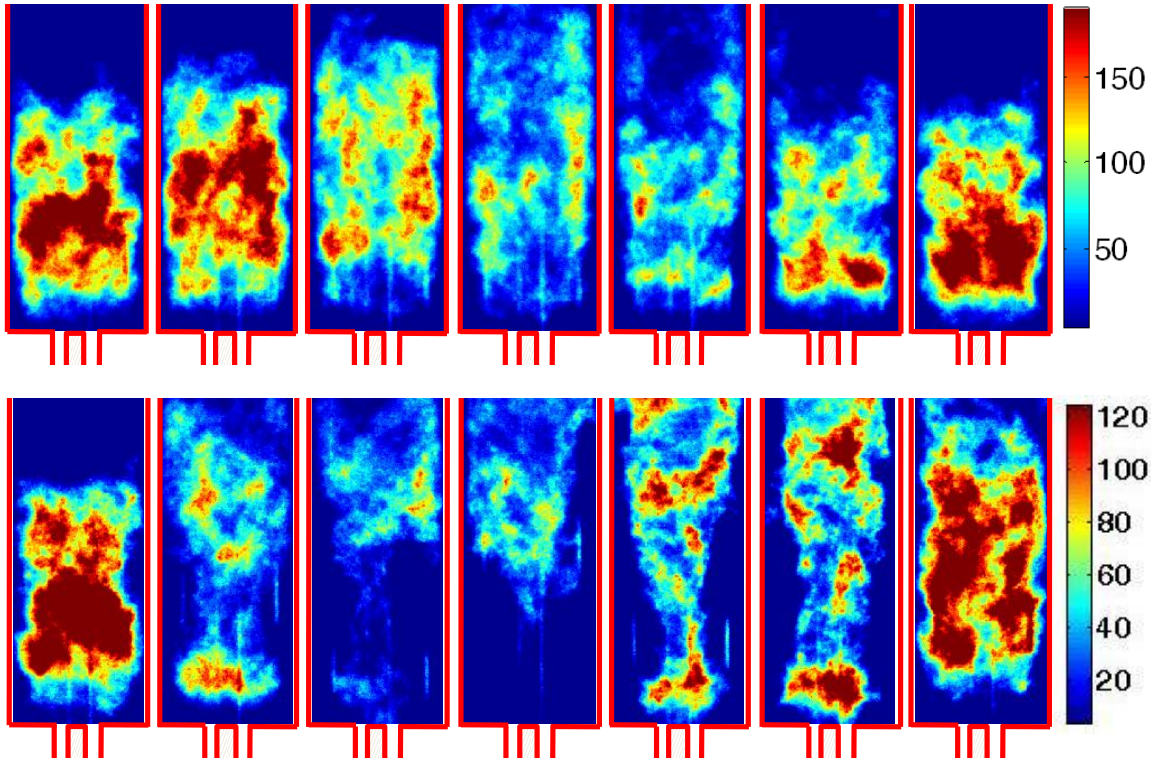

Figure 33. High speed flame chemiluminescence images for instability w/o Φ', Φ =0.698. (Top row) Images during normal combustion over an instability cycle with an image separation of 0.526 ms. (Bottom row) Images during a precursor event, every 13th image shown (effective image separation of ~6.8 ms). In the color bar red, represents the highest chemiluminescence emission intensity and blue represents the lowest.

Normal combustor operation (top row images) is characterized by instability cycles, and the top row images show roughly one full cycle, starting from a peak and ending at a peak in a heat release oscillation cycle. The flame length and radiation intensity are clearly modulated over a cycle. Bright and short flames correspond to high heat release, whereas long and weaker (lower radiation intensity) flames correspond to

low heat release in a cycle. High speed images for the combustor operating at equivalence ratios far from LBO exhibit similar periodic instability cycles.

In the bottom row of Figure 33, which corresponds to a precursor event, large scale flame extinction around the inner recirculation zone is seen, followed by its recovery. From other frames in the sequence, the normal flame was observed to extinguish gradually followed by a gradual recovery. Most of the time during the extinction period, there is a small region of heat release just above the center body. However on occasion, this center body flame was also lost, as seen in the 4^{th} frame. During the period of extinction, the flame switches to a lifted configuration, where most of the burning occurs downstream. The stable flame around the inner recirculation zone and the temporarily lifted flame can be considered two different flame modes. Precursor events in this combustor are associated with flame switching between these two modes. Similar flame shifting to lifted mode was observed in prior LBO margin sensing studies on a geometrically similar, gas-fueled combustor, under dynamically stable conditions [69].

High-speed flame chemiluminescence images during normal combustion and a precursor event, for instability w/ Φ' are shown in Figure 34. As before, both image sequences are from the same run. The images were acquired at 1000 frames/s with 500 μs exposures. In the images, a region of about 25 mm above the combustor was not optically accessible, unlike the images in Figure 33. The precursor event image sequence (bottom row) starts about 1.4 s after the end of the normal combustion image sequence.

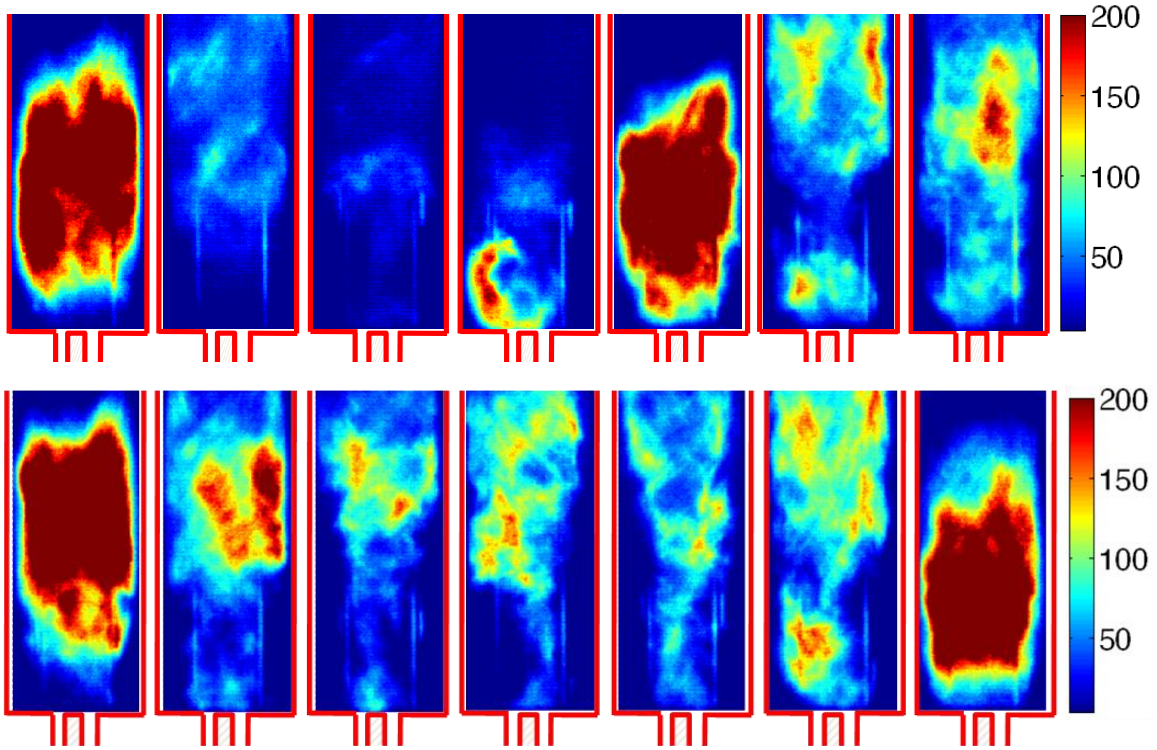

Figure 34. High speed flame chemiluminescence images for instability w/ Φ', average Φ =0.711. (Top row) Images during normal combustor operation with the first four images during a high amplitude instability cycle, separated by 1 ms; last two frames during a period of low instability. (Bottom row) Images during a precursor event with an image separation of 6 ms.

In contrast to the w/o Φ' case, normal combustor operation w/ Φ' is characterized by unsteady instability cycles, i.e., regular growth and decay in instability amplitude. Figure 35 displays an optical signal time trace (from the fiber optic sensor) acquired simultaneously with the high speed images during normal operation (top row in Figure 34). In Figure 35, the times corresponding to each high-speed image are indicated by circles. The first five images in the top row are during a high amplitude instability cycle, and the next two are during a period of low instability. During instability cycles, flame length and intensity modulations are evident, similar to instability w/o Φ'. However, the modulations in intensity are much larger (the same image intensity scaling is used in the figure for both cases), suggesting that equivalence ratio oscillations are significant.

Higher equivalence ratios during an oscillation cycle would make the flame brighter, whereas low equivalence ratios make it weaker. During the period of reduced instability (last two frames), the flame is longer on average, with small oscillations in intensity and length. From the 2nd and 3rd images, during troughs of an instability cycle, some amount of flame extinction is observed. This apparent extinction along with a weak flame results in the optical signal amplitude dropping close to zero during the troughs of the instability cycle. Though partial extinction is occurring during these instability cycles, they should not be considered LBO precursors as the combustor shows no tendency to blowout and can operate continuously. Such statically stable operation could result from the instability amplitude decaying after its initial growth, thus leading to a more stable flame as seen in the last two frames. If the instability amplitude were continue to remain the same, or even rise, it might lead to complete flame loss and blowout.

In contrast to the short duration extinctions, the bottom row in Figure 34 contains a sequence of images with extinction occurring for a much longer duration (~23 ms) with more pronounced extinction. The extinction is around the inner recirculation zone, similar to the extinction during precursors for instability w/o Φ'. Such long duration extinctions were found to occur only near LBO, and hence can be considered precursors.

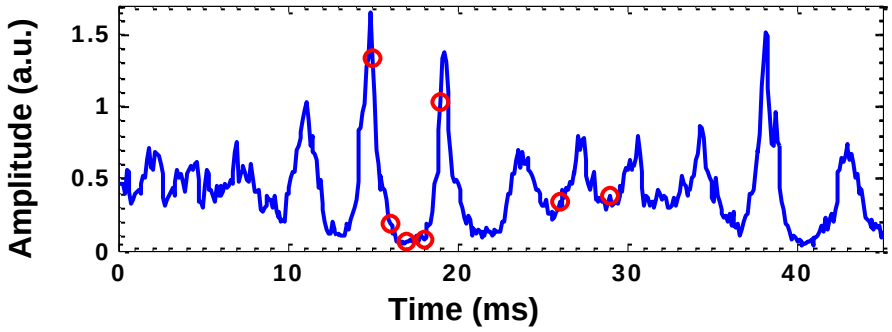

Figure 35. Optical signal time trace acquired simultaneously with the high-speed images in Figure 34 (top row images), for instability w/ Φ'. Image locations are indicated by circles.

4.1.3. Precursor event detection

For robust LBO margin sensing, precursors should be detected reliably, i.e., without missing events and not detecting false events. Precursor events can be detected using the double thresholding method used in earlier work, along with a time constraint. The method consists of a lower and upper threshold evaluated using recent signal statistical properties, signal mean (μ) and standard deviation (σ). An example precursor event along with the thresholds is shown in Figure 36. The lower threshold is set sufficiently below the minima of the nominal signal to detect the amplitude drop during a precursor event. The upper threshold is set close to the signal mean such that noise or instability during a precursor does not cross this threshold, which otherwise would result in a single event counted multiple times. An event starts when the signal level drops below the lower threshold and ends when it rises above the upper threshold. A minimum time constraint can also be imposed on the duration a precursor spends between the two thresholds for more robust event detection. Both the lower and upper thresholds are determined from the relation μ-$\kappa\sigma$, where κ is a constant. The upper threshold is set with a smaller value of κ compared to the lower threshold.

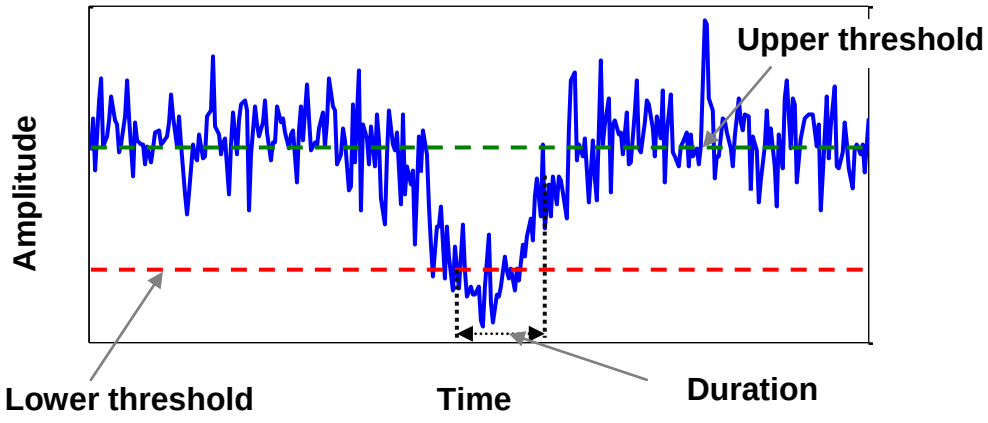

Figure 36. An example precursor event in optical signal along with the thresholds used for its detection.

As noted above, precursor events during dynamically stable conditions and during instability w/o Φ' look qualitatively similar. The signal amplitude drops below the nominal signal minima during a precursor. However, the nominal signal minima are considerably lower during the instability due to high coherent modulations in the signal. The double thresholding method could be used for event identification in both the cases; however, it would require different κ values. For example, if the same κ were used for instability w/o Φ' as for the dynamically stable case, it would result in the lower threshold having negative values, which is not helpful. Moreover, precursors for instability w/ Φ' look qualitatively different from the other two cases; the signal amplitude does not drop below the nominal signal minima, because the nominal signal minima are very small, close to zero. Hence, the lower threshold, used for detection of amplitude drop below the nominal signal minima, is not useful. However, the events could be detected in other ways, for example, when the signal amplitude stays below the signal mean for more than a specified duration. In summary, the three cases (dynamically stable, instability w/ Φ' and w/o Φ') would require different event identification algorithms to analyze the raw signals.

In practical combustors, operation can switch between dynamically stable and unstable operation. In addition, the dynamic instability mechanism, frequency and amplitude may change with operating conditions. These changes would require using multiple LBO precursor identification algorithms and algorithm switching based on the status of the dynamic instability e.g., amplitude and frequency. However, such an elaborate approach requires careful development and validation, and may fail to work reliably. A single algorithm that could work regardless of the status of dynamic instability is desirable for robust LBO margin sensing. It can be speculated that getting rid of the instability component, as it is not associated with precursor events, could make a single event detection algorithm work robustly under all conditions.

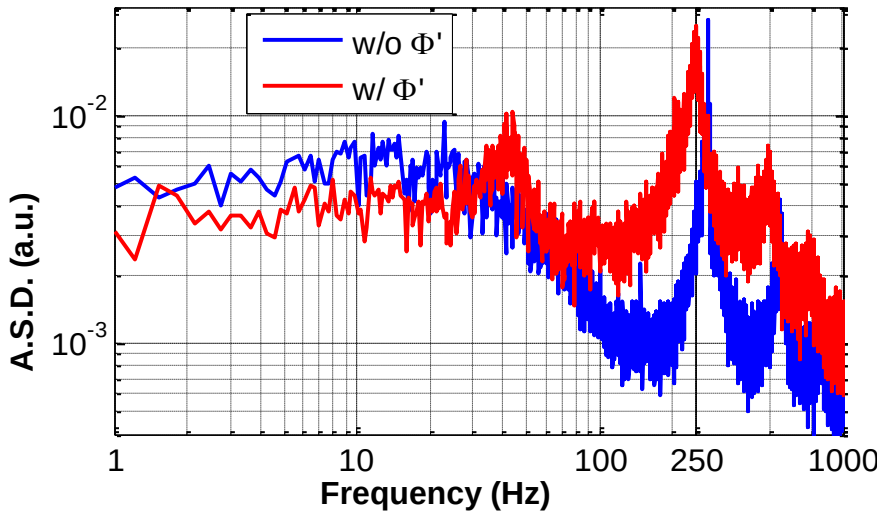

Figure 37. Amplitude spectra of optical signals for instability w/ Φ' and w/o Φ'. Equivalence ratios: 0.698 (w/o Φ'), 0.714 (w/ Φ').

From precursors in the optical signals, the duration of the events in this combustor are between 30-50 ms. On the other hand, the dynamic instability period for the combustor is about 4 ms, much shorter than the precursor duration. Amplitude spectra of the optical signals, for the time series data used in Figure 32, are shown in Figure 37 for both instability cases. The spectra are ensemble averaged over several individual spectra. Besides the instability peak around 250 Hz, the amplitude spectral density is nearly constant in the range 1-30 Hz for instability w/o Φ' and 1-50 Hz for instability w/ Φ' and starts to drop before rising near the instability frequency. The relatively high power in the low frequency range (1-50 Hz) is most likely due to precursor events due to their longer time scales. Since the spectral content of the events and the instability are widely separated, signal processing techniques such as low-pass filtering can be used for suppressing the dynamic instability.

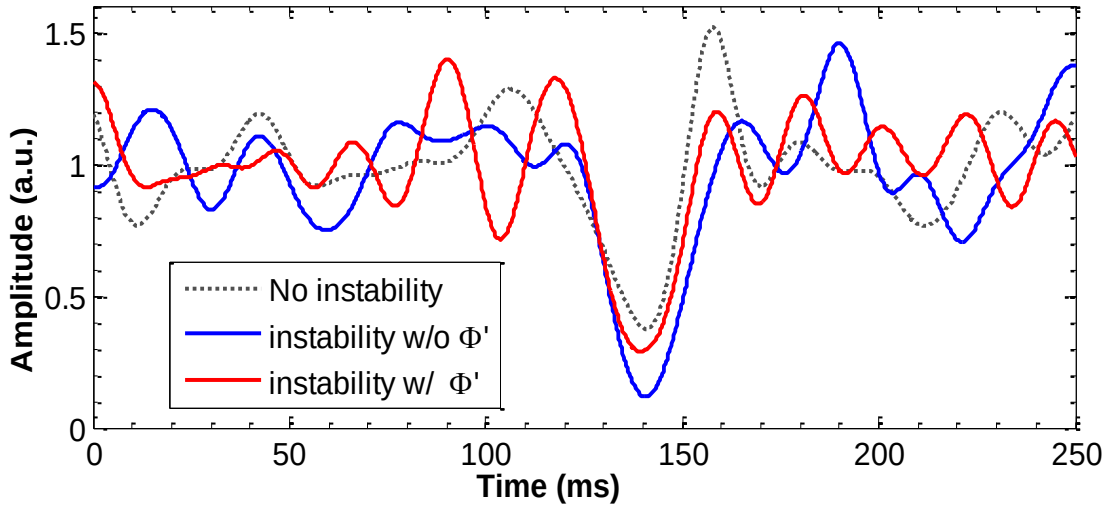

Figure 38. Precursor events in low-pass filtered (50 Hz) optical signals for dynamically stable and unstable w/o Φ' and w/ Φ' conditions.

Low-pass filtered optical signals during precursor events for dynamically stable and unstable conditions are shown in Figure 38. These filtered time traces correspond to the raw traces shown in Figure 31 and Figure 32. Low-pass filtering was performed at 50 Hz with a 4-th order digital Butterworth filter. The cutoff frequency was chosen based on the observation precursors have spectral content up to 50 Hz in the w/ Φ' instability case. In addition, due to the slow roll off of the Butterworth filter, the cutoff frequency should be sufficiently below the instability frequency. However, cutoff frequencies anywhere in the range 20-100 Hz have been observed to work equally well. The filter is an infinite impulse response filter, with the group delay, i.e., time delay, a function of the frequency. In this case the delay is about 8 ms in the pass band, and goes to a maximum of 12 ms at 110 Hz. For the precursors, the filtering causes a delay of about 9 ms. Several other filter types or different filter orders have been observed to produce similar results. After filtering, all three precursors have a similar characteristic shape of slow amplitude drop and recovery.

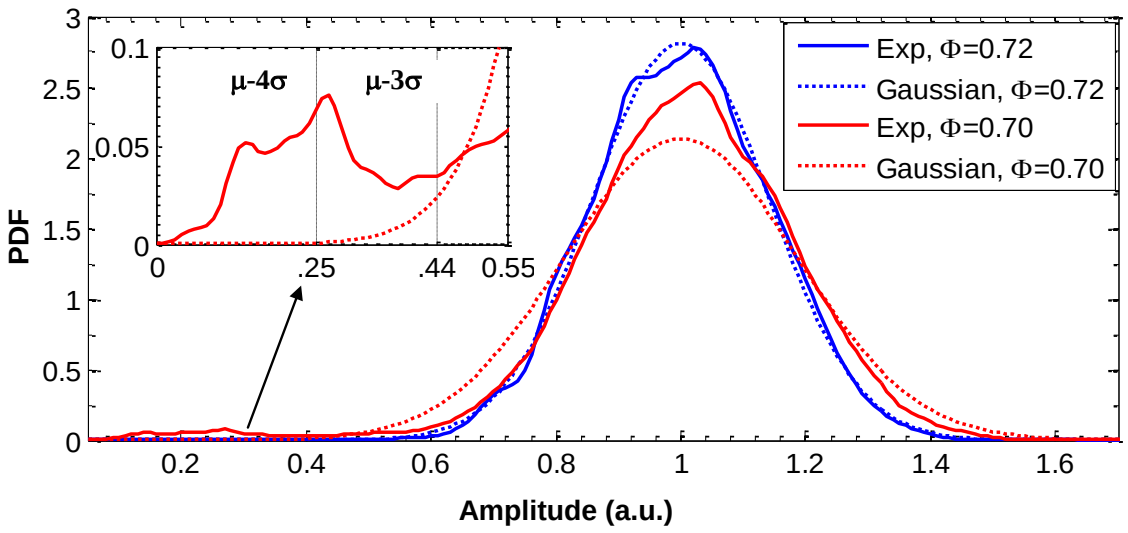

Figure 39. PDFs of low-pass filtered optical signals along with corresponding Gaussian PDFs for far from LBO and near LBO operation for instability w/o Φ'. An inset plot with reduced X and Y scales for near LBO case is also shown.

Such similarity should enable use of a single event identification algorithm, such as the double thresholding approach, over the full range of operating conditions, regardless of the dynamic instability characteristics. The lower threshold selection for detection of precursor events should be based on the signal's noise characteristics and the amplitude drop during precursor events. To help in selection of this threshold setting, probability density functions (PDF) of the low-pass filtered optical signals at two equivalence ratios, along with the corresponding Gaussian PDFs for instability w/o Φ' are shown in Figure 39. The Gaussian PDFs are calculated using the mean and standard deviation of the corresponding filtered optical signals. The signal PDF closely matches the Gaussian PDF at operation far from LBO (Φ=0.72). This implies that a lower threshold below μ-3σ has a very small probability of signal dropping below the threshold under normal operation, and such a threshold would produce only a few false events. Near LBO, the PDF somewhat deviates from the Gaussian, having a smaller width with a higher probability for low amplitudes. This behavior can be attributed to precursor events. For the near LBO PDF, an enlarged version is also shown in the inset plot with X

and Y axis scales reduced. The probability starts to increase below μ-3σ and peaks at μ-4σ. Therefore, the lower threshold setting for precursor detection should be at least below μ-3σ, whereas μ-4σ may work better. Similar results were observed for instability w/ Φ'.

4.1.4. LBO Margin Detection

Average event occurrence rates obtained with different lower threshold settings in the range μ-3σ to μ-3.75σ for instability w/o Φ' are shown in Figure 40. The upper threshold and the minimum duration constraint are kept at μ-1σ and 10 ms respectively. The threshold level at a given time is calculated from signal data over the previous one second period. The results are from low-pass filtered optical signals at 50 Hz and are averaged over 29 s at each equivalence ratio. In evaluating the μ and σ for the threshold calculation, signal data during precursor events are omitted as it has been observed to lower the thresholds if large duration precursors or more precursors occur in the evaluation time window. In addition, any deviation above and below the μ-3σ limit is also excluded. From the figure, all the threshold settings produce low event rates far from LBO and high event rates near LBO. This suggests the robustness of event detection to moderate changes in threshold setting. However, an optimal threshold setting should produce almost no events far from LBO, to minimize false alarms. On the other hand, events should be the maximum possible near LBO (detection of all events) for a better indication of LBO margin. The thresholds, μ-3.0σ, μ-3.25σ and μ-3.5σ produce somewhat non-zero events far from LBO whereas μ-3.75σ produces zero events far from LBO. Therefore a lower threshold of μ-3.75σ is an appropriate choice for event identification.

Since the precursor event durations are sufficiently large, they are well above the nominal noise time scales. Hence event sensing has been observed to be not sensitive to

the duration constraint. In addition, as the upper threshold is mainly used for imposing the duration constraint, it is not independent from the duration constraint.

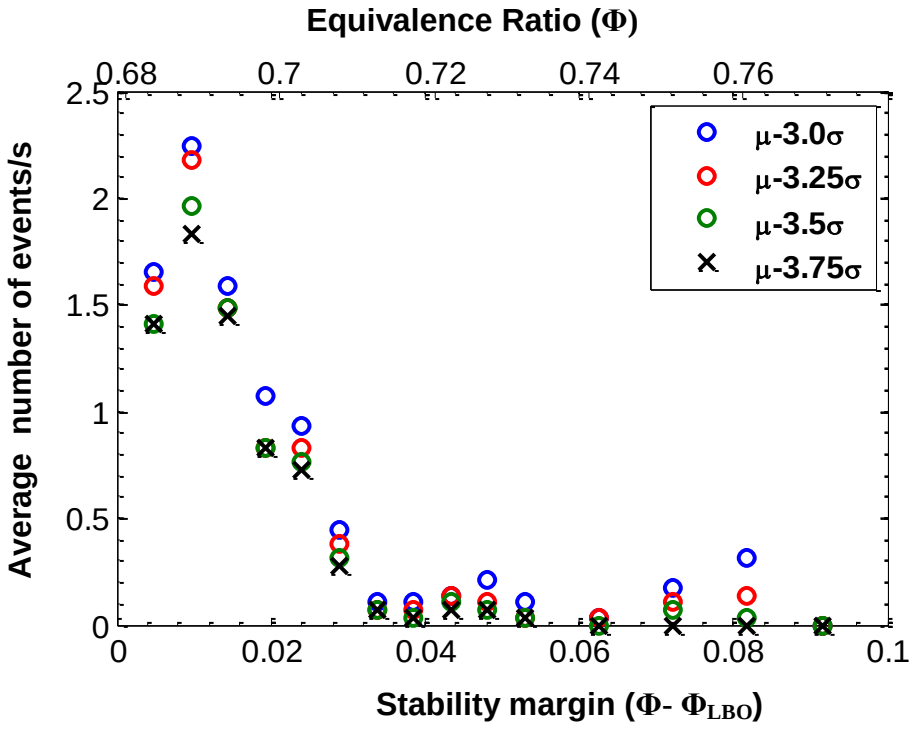

Figure 40. Average number of events per second for different lower threshold settings for instability w/o Φ'. Upper threshold=μ-1σ and minimum time constraint=10 ms.

Results of event identification for the three operational modes of the combustor, i.e., dynamically stable, unstable w/o Φ' and w/ Φ', are shown in Figure 41. Similar to the above results, the events are obtained from low-pass filleted optical signals (@ 50 Hz) and are averaged over 29 s. The optimal threshold settings for instability w/o Φ', lower threshold of μ-3.75σ upper threshold of μ-1.0σ and a minimum time constraint of 10 ms, are also used for the other two cases. Similar to the observations in previous work, the average event occurrence rate increases as the combustor approaches the LBO limit. Therefore, the number of events occurring per unit time is a reasonable measure of proximity to LBO. A single event identification algorithm produced an acceptable event rate trend for all the three cases. This further demonstrates the ability of low-pass filtering to allow for one, universal event identification algorithm to be successful regardless of

the state of dynamic instability. As shown in the figure, events start to occur around a stability margin of 0.03 (early warning margin) and the average event rate is between 0.2-2 events/s. In addition, the event rate increases somewhat monotonically with reduction in stability margin. However, it drops slightly just before LBO for both the dynamically unstable cases. Relatively large duration precursors have been observed to occur just prior to LBO and the event rate drop can be attributed to this. For both the dynamically unstable cases, event rates are similar, whereas it is nearly half for the dynamically stable case. This behavior could be attributed to the increased likelihood for an event to occur because of large perturbations in velocity and equivalence ratio during instability.

The duration of precursor events is an important feature of the precursors, and in prior studies it was observed to increase towards LBO. The average duration of a precursor, obtained by averaging over all the precursors detected at given equivalence ratio, is shown in Figure 42 for the three operational modes of the combustor. Since low-pass filtering smoothens signal, the actual duration of precursors cannot be obtained from the filtered signals. Therefore, unfiltered signals were used to determine the event durations. For this analysis, the duration is defined as the time spent by the signal below the local mean during a precursor. The precursor event detection algorithm was different for the three cases as a single algorithm could not be used for all, due to different characteristics of the precursors. For the dynamically stable mode, events were detected using the constraints: signal should spend at least 10 ms between successive crossings of the mean and during this period the signal level should drop below μ-3.0σ threshold at some instance. For instability w/o Φ', similar approach was used, with the threshold changed to μ-1.25σ as the nominal σ of the signal is large due to high modulations in the signal due to instability. For instability w/ Φ', the only constraint used was that the signal should spend at least 10 ms below the local mean between successive crossings. Each algorithm was observed to detect precursors reliably and produced similar events rates as

the filtered signals. In Figure 42, it can be seen that the average event duration increases as LBO is approached, for all the three cases. Near LBO, when a considerable number of events start to occur (stability margin < 0.03), event durations are in the range 15 - 45 ms. For the w/ Φ' instability case, event durations are considerably lower compared to the w/o Φ' and dynamically stable modes. It is possible that for instability w/ Φ', the oscillations create stratification in the equivalence ratio, specifically regions of high equivalence ratio that could promote re-ignition, thus lowering precursor duration.

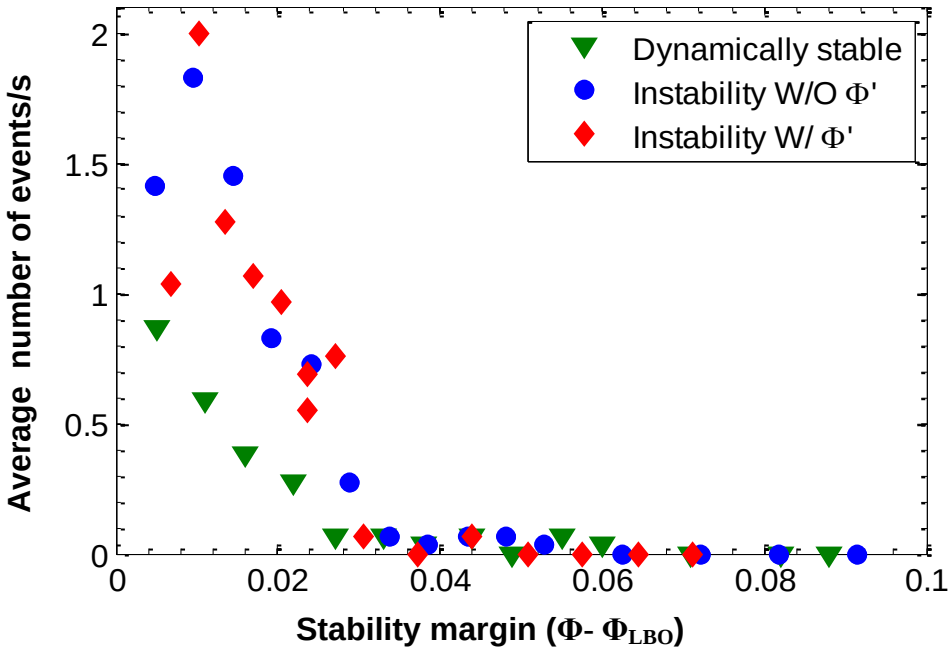

Figure 41. Average event occurrence rates obtained from low-pass filtered optical signals for dynamically stable, dynamically unstable w/o Φ' and w/ Φ'.

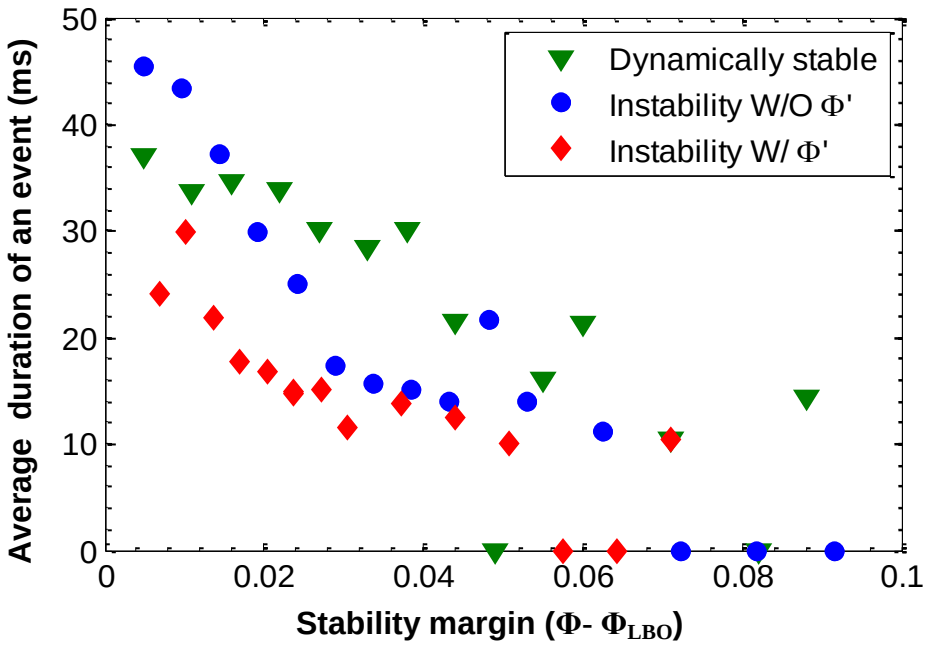

Figure 42. Average event duration obtained from un-filtered optical signals for dynamically stable, dynamically unstable w/o Φ' and w/ Φ'.

In addition to the event occurrence rate and event duration, the modulation depth of events might also be expected to increase as LBO approaches, as the the extinctions are likely to become larger in spatial extent. Therefore, these three signal features (number of events, duration and modulation depth) can be combined into one single parameter for robust estimation of LBO margin. The parameter, denoted Stability Index (*SI*), is defined in Eq (4.1). Here *C(t)* is the chemiluminescence signal at time *t*, $\bar{C}$ is the signal local mean, T_{window} is the time window used for integration and δ_{event} is used to include data only when an event is occurring (1 during events and 0 otherwise). A discretized form of this expression could be used for *SI* evaluation from sampled data. From the definition, *SI* is non-dimensional, and it is essentially the integrated signal loss below the mean during events. In physical terms, *SI* represents the fractional loss in local heat release due to precursors. This approach weighs the LBO proximity parameter by the strength of an event, instead of weighing all the events equally as in the use of event occurrence rate.

$$SI = \frac{1}{T_{\text{window}}} \int_0^{T_{\text{window}}} \left(\frac{\bar{C} - C(t)}{\bar{C}} \right) dt \, \delta_{\text{event}} \tag{4.1}$$

The Stability Index and the event rate, normalized with corresponding averaged values in the Φ-Φ_{LBO} range 0.034-0.053, are compared in Figure 43 for instability w/o Φ'. The *SI* is calculated from low-pass filtered optical signals at 50 Hz and averaged over 29 s at each equivalence ratio, similar to the event rate. In the plot, an additional vertical-axis scale (on the right hand side) for the actual values of *SI* is also shown. *SI* clearly provides a higher dynamic range compared to the event rate, and in that sense, a better LBO proximity parameter. Near LBO, *SI* varies between 1-7%, suggesting there is a similar level of reduction in the heat release due to precursors in the region viewed by the sensor.

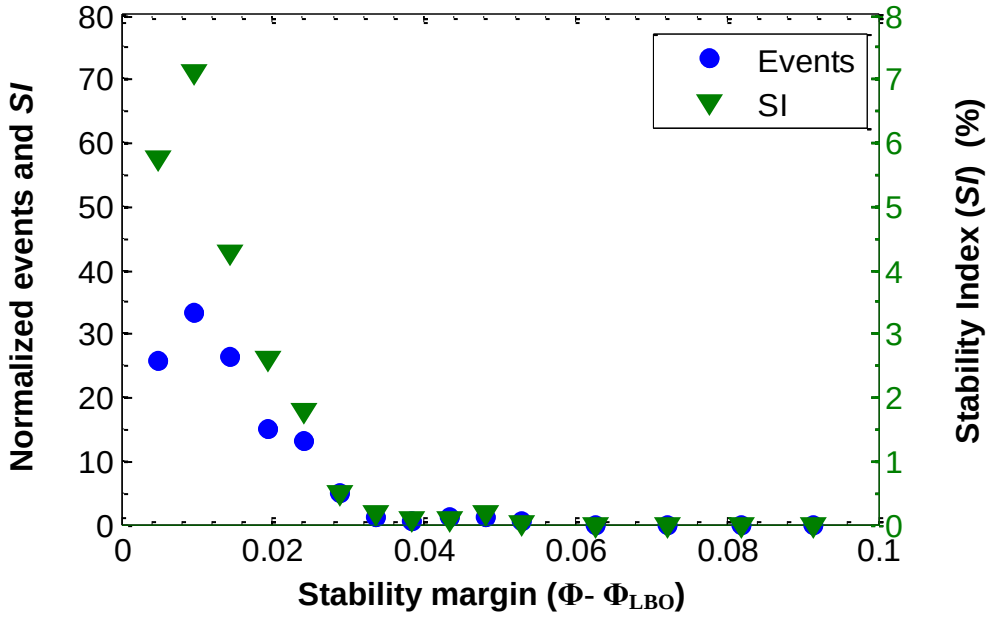

Figure 43. Average event rate and Stability Index (*SI*) for instability w/o Φ' obtained from low-pass filtered optical signals. Left vertical axis scale: event rate and *SI* normalized with average event rate *SI* in the range Φ-Φ_{LBO} = 0.03-0.05. Right axis scale: actual scale for *SI*.

A similar comparison of *SI* and occurrence rate for instability w/ Φ' is shown in Figure 44. Here, event rate and *SI* are normalized with corresponding values in the Φ-

Φ_{LBO} range 0.023-0.044. Again, *SI* produces a higher dynamic range. Compared to the results for the w/o Φ' case, instability w/ Φ' has lower values (1-5%), likely due to the shorter event durations. Though the results presented above (Figure 40 - Figure 44) are based on one data set, several other data sets acquired at different times were observed to produce similar results.

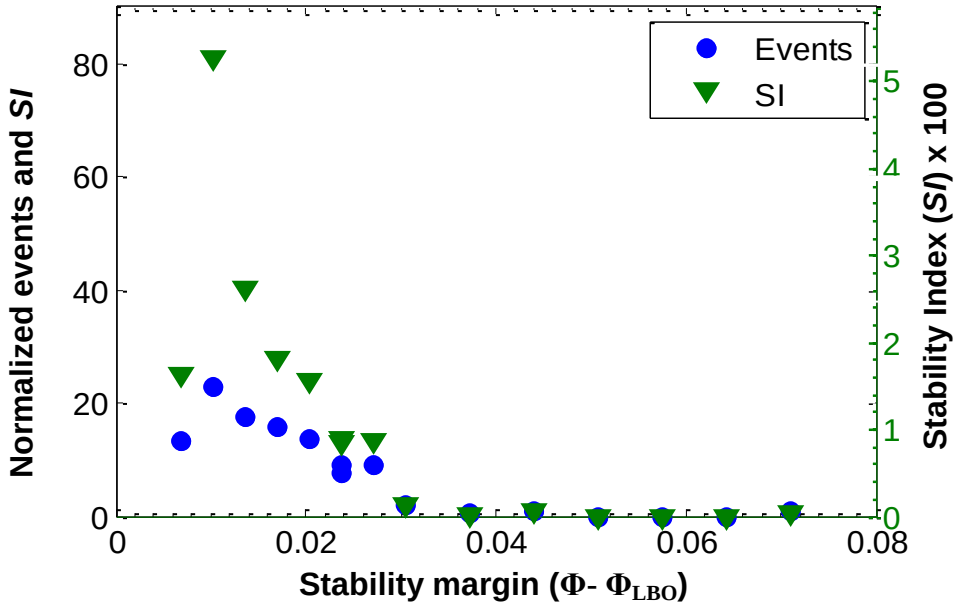

Figure 44. Average event rate and Stability Index (*SI*) for instability w/ Φ' obtained from low-pass filtered optical signals. Left axis scale: event rate and *SI* normalized with average event rate *SI* in the range Φ-Φ LBO = 0.023-0.044.

4.2. LBO Margin Sensing in the LDI Combustor

In order to investigate the robustness of the LBO margin sensing approach, tests were also performed in the liquid-fueled, single-injector LDI rig at elevated pressure (described in Chapter 3). The following results correspond to combustor operation at 2 and 4 atm, with a focus on the 2 atm case. Average un-burnt flow velocity in the combustor was about ~10 m/s, with ~700K inlet air. To examine the combustor behavior versus LBO margin, the air flow rate was kept constant and the fuel flow rate was decreased in steps until LBO occurred. As the exact equivalence ratio of the combustion could not be determined due to the presence of co-flow (see Chapter 3), results are

presented as a function of equivalence ratio normalized by the equivalence ratio where LBO occurs (Φ/Φ_{LBO}). For 2 atm operation LBO occurred at an overall equivalence ratio of 0.23 and for 4 atm it occurred at 0.19. Both OH^* and CH^* chemiluminescence signals were recorded. In the following results, CH^* signals are mainly presented.

4.2.1. Instability Characteristics

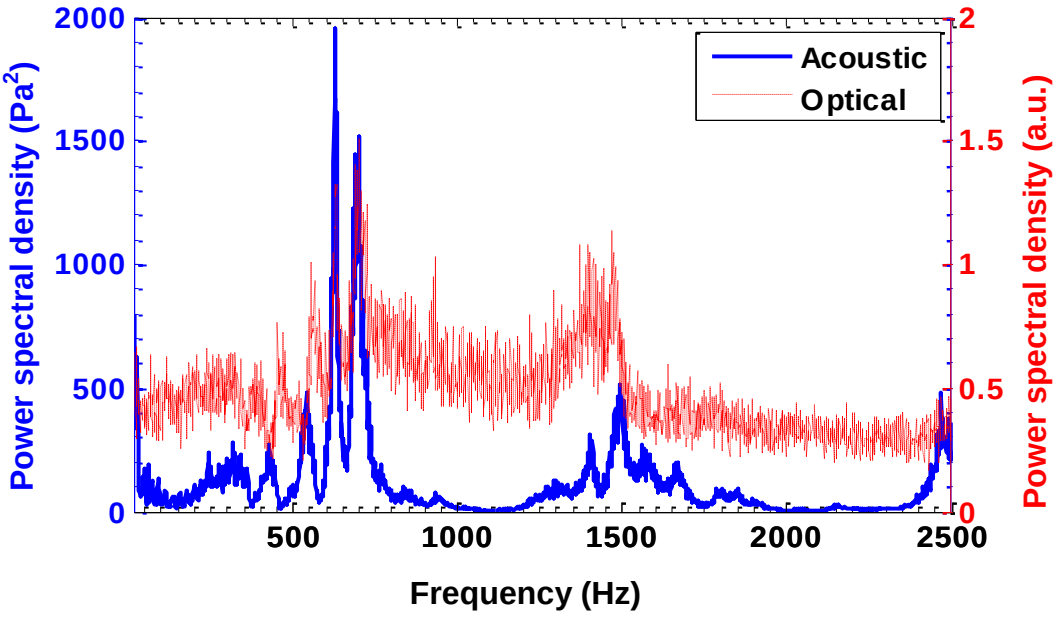

Figure 45. Power spectra of CH^* signal and acoustic signals for LDI combustor operation near LBO at Φ/Φ_{LBO} = 1.09; combustor pressure = 2 atm.

The power spectrum of the CH^* chemiluminescence signal from the LDI combustor is shown in Figure 45 for combustor operation at 2 atm near LBO (Φ/Φ_{LBO}=1.09). For characterization of the dynamic stability of the combustor, a spectrum is also shown for the acoustic pressure (recorded simultaneously). The spectra are obtained by ensemble averaging the Fourier transforms of 40 data sets, each having a spectral resolution of 1 Hz and a Nyquist frequency of 2500 Hz. The LDI combustor appears to exhibit a moderate level of dynamic instability, as evidenced by the narrow peaks in the power spectra of the optical (CH^*) and acoustic signals. The acoustic power spectrum illustrates the complexity of the dynamics, as there are multiple local peaks in

the spectrum. For example, there are multiple modes (peaks) at approximately 580, 660 and 725 Hz, as well as their harmonics. The strongest mode at 660 Hz corresponds to the axial quarter wave mode of the combustor, based on an assumed uniform gas temperature of ~1700 K. It has a sound pressure level of nearly 120 dB. In the optical power spectrum, the power is distributed over a similar broad range of frequencies, with a lower fraction of the power at the instability frequencies. For more pronounced combustion dynamics, nearly all the power would be expected to be in narrow ranges around the instability frequencies, similar to the spectra in the gas-fueled combustor. While only 2 atm results are shown here, 4 atm operation produces a similar behavior.

4.2.2. Precursor events

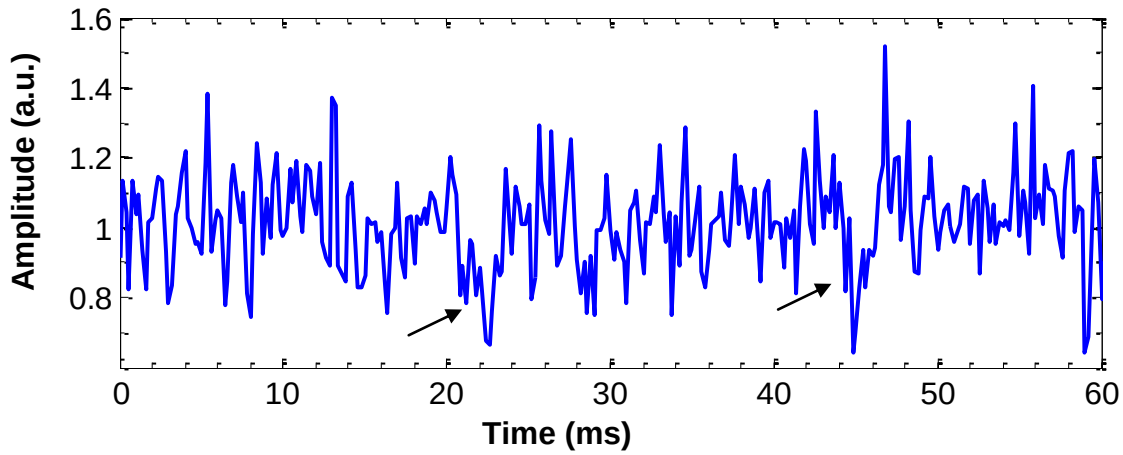

Figure 46. CH^* signal time trace with precursor event features indicated by arrows for combustor operation close to LBO at $\Phi/\Phi_{LBO} = 1.02$.

Figure 46 displays a CH^* time trace for combustor operation at 2 atm just prior to LBO (at $\Phi/\Phi_{LBO} = 1.02$) with precursor event-like features indicated by arrows. The signal features are characterized by temporarily low amplitude, for an extended duration, compared to the neighboring region; this is the expected behavior for LBO precursors. However, the amplitude drop is not significantly lower than the nominal signal minima. Thus the precursor signatures observed here are less pronounced than those observed in the gas-fueled combustor. The duration of these precursors is about 2-3 ms, much smaller

than the ones in the gas fueled combustor (15-45 ms). Similar short duration precursors (~6 ms) were observed in prior LBO sensing studies in a conventional (non-LDI) liquid fueled combustor [25]. Besides, unlike the gas fueled combustor, signal amplitude stays well above zero during precursors. The smaller durations and modulation depths of precursors result in smaller precursor signatures. The smaller signatures require a careful selection of the event detection algorithm to prevent false detection of events.

Precursors with much weaker signatures (smaller durations and modulation depths) than the ones shown in Figure 46 were also observed, especially for conditions not so close to LBO, e.g., Φ/Φ_{LBO}=1.09. For providing LBO warning with a sufficient margin, such events have to be detected, without producing false events far from LBO. Reducing the "noise" (any amplitude modulation other than the precursor) can be expected to minimize false events. The "noise" in the optical signal has contributions from both dynamic instability and turbulent combustion generated noise. While the turbulent noise is broadband, the instability modes have periods in the range 1.4-1.7 ms (580-725 Hz). On the other hand, the precursor event durations are in the range 1.5-3 ms. The short duration events have similar time scales as the dynamic instability period. Low-pass filtering at 500 Hz, corresponding to a 2 ms time period, is able to suppress the instability and other high frequency noise and improved precursor signatures. This is evident in Figure 47, which presents a low-pass filtered optical signal corresponding to the raw signal in Figure 46. Low-pass filtering makes the precursors more evident. The filtering was performed with an 8^{th} order digital Butterworth filter. The higher filter order was used to achieve a sharper cutoff, as the instability period and precursor durations are close to each other. The filtering delays precursors by 2 ms, which may not be significant.

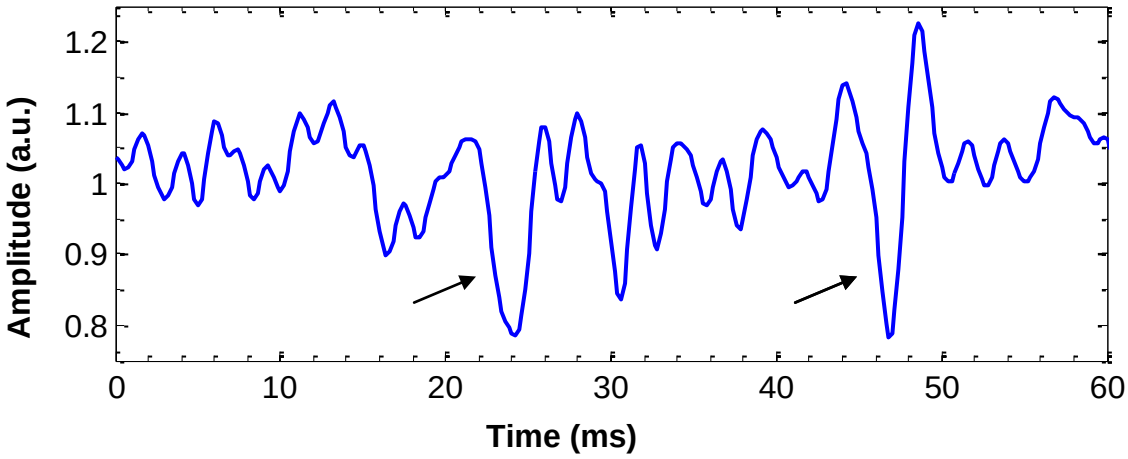

Figure 47. 500 Hz low-pass filtered CH^* signal with precursors indicated by arrows for combustor operation close to LBO at $\Phi/\Phi_{LBO} = 1.02$.

High-speed flame images during such a precursor event are shown in Figure 48. The images are successive 1 ms exposures, with the camera viewing at an angle of 45° from downstream direction, similar to the optical fiber (see Chapter 3). Grayscale (0-255 range) images are scaled with an intensity based color map as shown in the figure. The images are broadband chemiluminescence images, filtered between 325-600 nm using an optical filter placed before the camera lens. The 4th and 5th frames show a signification amount of flame extinction, followed by its recovery in the subsequent frame. Far from LBO, no such extinctions were observed and the flame appearance is similar to that of the flame in first three frames, with some unsteadiness. From observations of the high speed images during other extinction events, there is no single, preferable region where extinction occurs. In fact, it seems that the extinction event may begin at any particular azimuthal location and rotate around the combustor during the event. Based on the high speed images, the duration of the extinction is approximately 2-3 ms, as some level of extinction may still be present in the 3rd and 6th frames as well. Unlike the gas fueled combustor, there is no evidence of flame lift-off during precursors. Absence of such a flame mode change may be the cause of shorter event durations for the LDI combustor.

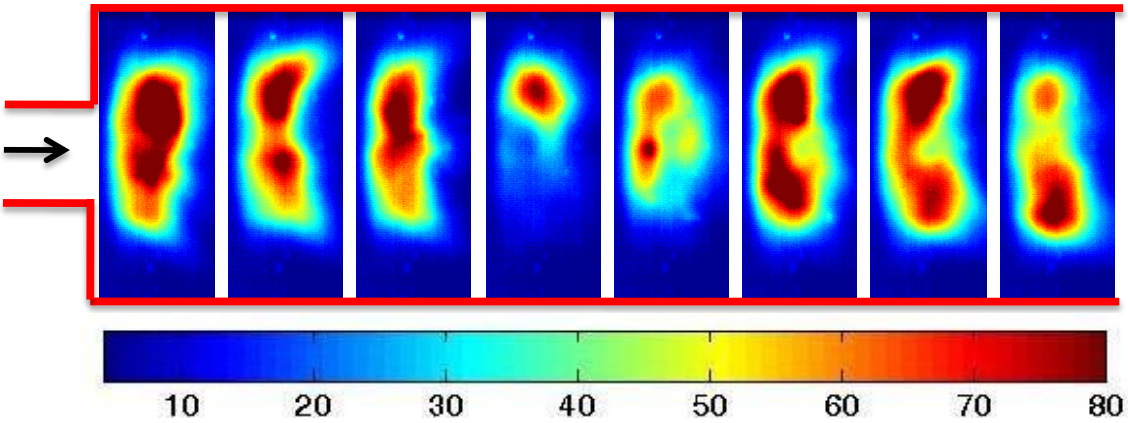

Figure 48. High speed flame images during a precursor event in the LDI combustor at 2 atm operation near LBO.

4.2.3. LBO Proximity Sensing

Precursor events in the filtered optical signals can be detected using the double thresholding approach, similar to the one used for the gas-fueled combustor. However, due to the smaller modulation depths and the durations of the precursor events, the threshold level and the duration constraints may require modification. Results of event identification for different lower threshold settings, obtained from low-pass filtered CH^* signals, averaged over 39 s at each equivalence ratio are shown in Figure 49. In the figure, an inset plot with the vertical scale reduced is also shown in order to emphasize on the event rates far from LBO. The upper threshold is kept at μ-0.5σ, and the duration constraint at 1.4 ms. In evaluating the signal mean and standard deviation, any departure above and below the μ-3σ limit is excluded. Besides, the signal during precursor events is also excluded from the calculation. From the figure, though all the threshold settings seem to provide an acceptable event rate trend, the setting μ-3.5σ may be the preferable choice, as it produces nearly zero events far from LBO and maximum near LBO. The setting μ-3.25σ produces non-zero event rate far from LBO, i.e., in the Φ/Φ_{LBO} range 1.3-1.5, and hence may not be preferable. On the other hand, the μ-3.75σ threshold setting,

though it produces zero events far from LBO, has a lower event rate near LBO and hence is not preferable.

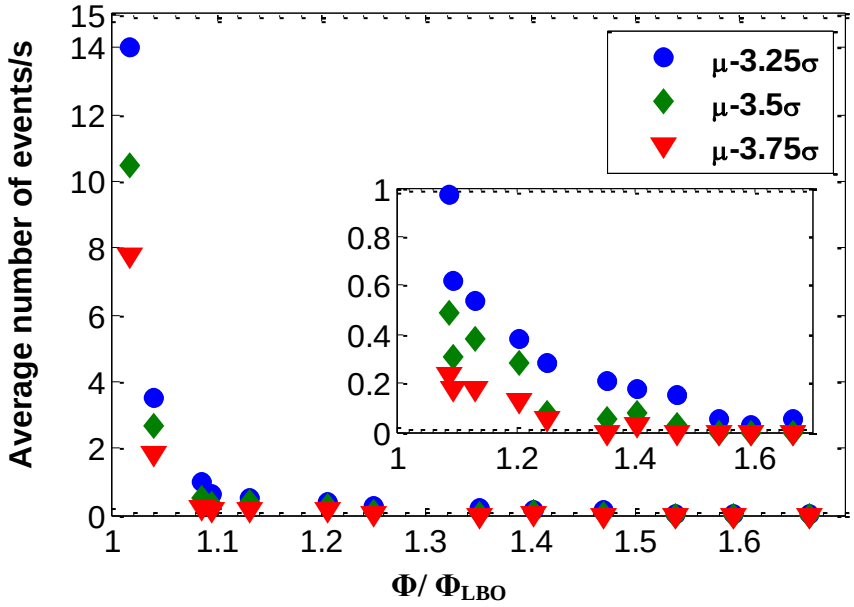

Figure 49. Average event rates for different lower threshold settings; upper threshold=μ-0.5σ and minimum time constraint =1.4 ms.

Besides the lower threshold, the event rate was also observed to be sensitive to the duration constraint as the precursor durations are close to the noise time scales. Average event rates for different duration constraints are plotted in Figure 50. The lower threshold in all cases is μ-3.5σ and the upper threshold is μ-0.5σ. Though all the duration constraints produce an acceptable event rate trend, the 1.4 ms constraint produces nearly zero events far from LBO and a high level near LBO. Based on these results, a lower threshold of μ-3.5σ, an upper threshold of μ-0.5σ and a minimum duration constraint of 1.4 ms was chosen to be the optimal settings for event detection in low-pass filtered CH^* signals in the LDI combustor.

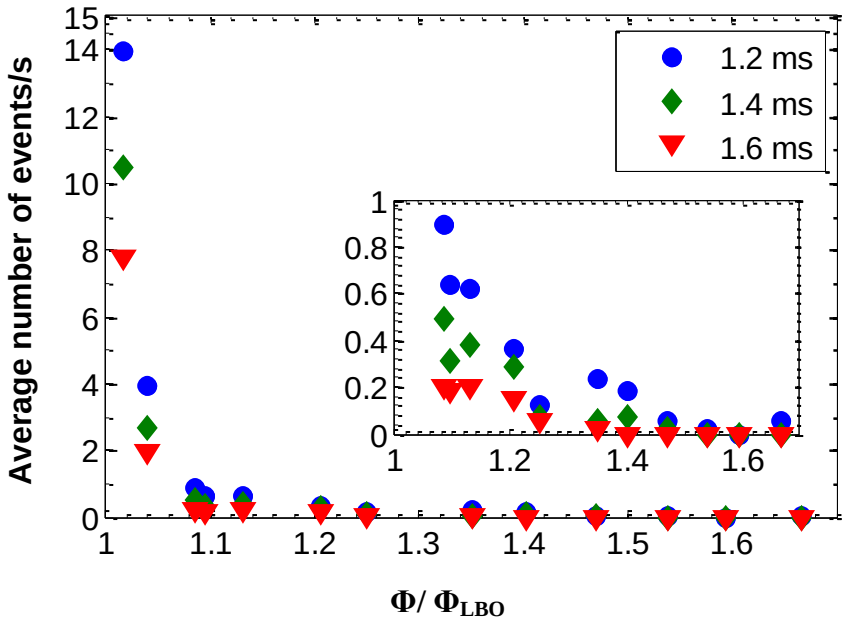

Figure 50. Average event rates for different minimum duration constraints; lower threshold=μ-3.5σ and upper threshold=μ-0.5σ.

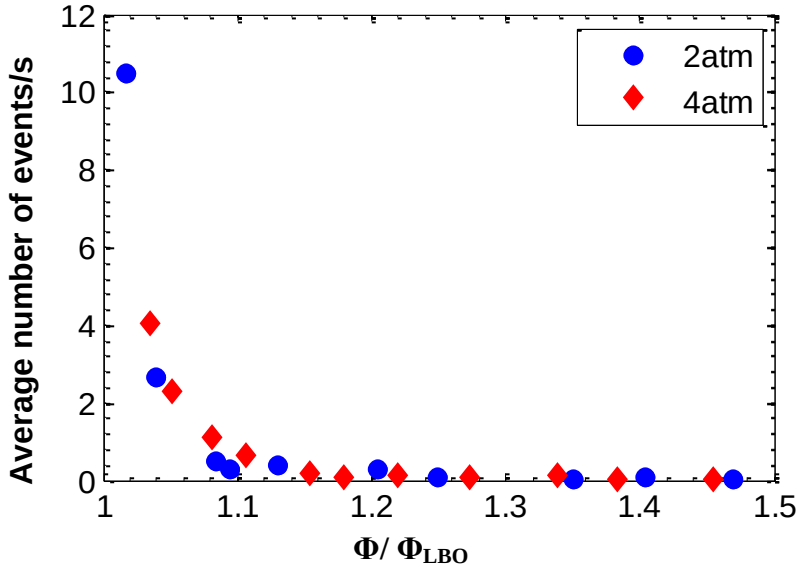

Figure 51. Average event rates for 2 and 4 atm operations.

Average event rates for 2 and 4 atm operation, obtained from 500 Hz low-pass filtered signals, are compared in Figure 51. For both pressures, the optimal event detection settings, identified above are employed. The average event rate is nearly the same for both the operating conditions. The seemingly lower event rate very close to

LBO for 4 atm operation is due to the lowest equivalence ratio not being as close to LBO as for the 2 atm case. The similar event rates for the different operating pressures are an indication of the robustness of this LBO sensing approach.

In the gas-fueled combustor, event durations and modulation depths increased towards LBO. Similar results for the liquid-fueled LDI combustor are plotted in Figure 52. Event durations are obtained from the unfiltered signals. As before, the duration of an event is defined as the time spent by the signal below the local mean during an event. Events are detected with a lower threshold of μ-3.25σ, an upper threshold of μ and a duration constraint of 0.8 ms. These settings provided event rates similar to the optimal event rates obtained from the filtered signals. The modulation depths are obtained from low-pass filtered signals, using the optimal threshold settings for low-pass filtered signals. Both event duration and modulation depth remain nearly constant until very close to LBO, then increase. Therefore combining event duration and modulation depth with event occurrence rate, using the Stability Index, should provide a more robust LBO proximity parameter, similar to the gas-fueled combustor.

Stability Index and event rate, normalized with the corresponding average values far from LBO ($\Phi/\ \Phi_{LBO}$ =1.25-1.47), are plotted in Figure 53, along with absolute values for *SI*. Both the event rate and *SI* are obtained from low-pass filtered signals, using the optimal threshold settings. *SI* is calculated by integrating the signal loss below the local mean during precursor events. As found for the gas-fueled combustor, *SI* provides a higher dynamic range compared to the average event rate. However, the LDI *SI* is about an order of magnitude smaller than the *SI* in the gas-fueled combustor. This is due primarily to the shorter event durations and modulation depths in the LDI combustor.

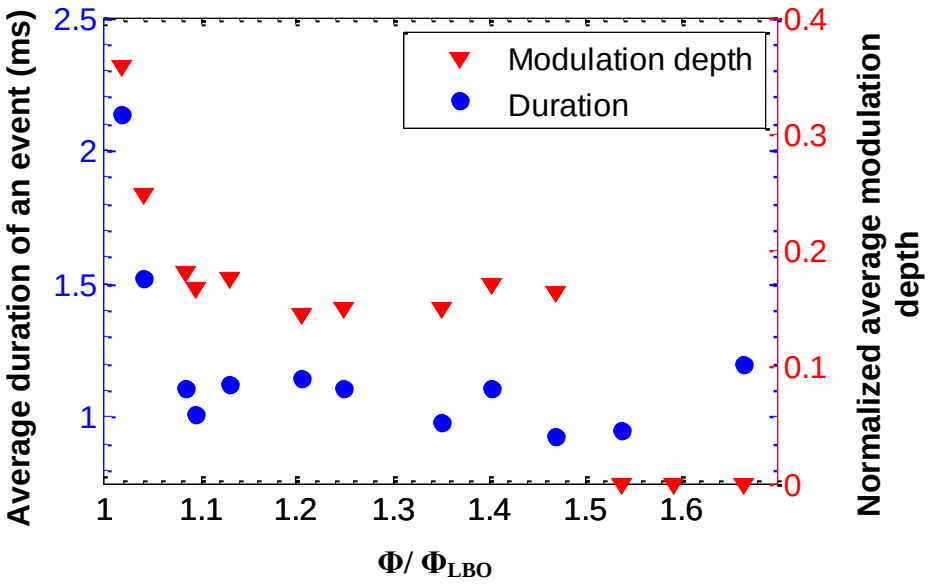

Figure 52. Average duration and normalized modulation depths of an event.

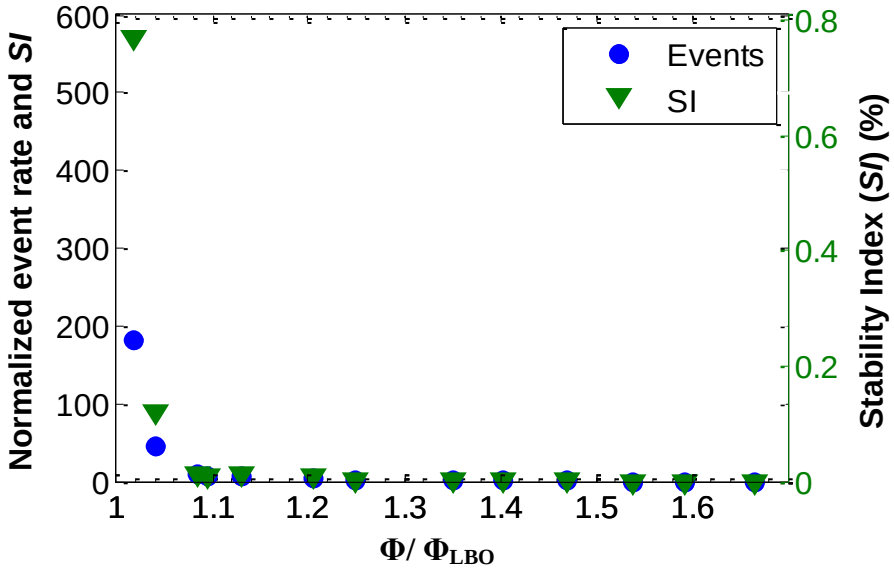

Figure 53. Average event rate and Stability Index (*SI*) comparison. Left axis scale: event rate and *SI* normalized with average values in Φ/ Φ_{LBO} range: 1.25-1.47.

The potential for real time LBO proximity sensing during slow transients, using precursor events, is demonstrated in Figure 54. Here, the fuel flow rate was decreased slowly and continuously, starting from t=0 s until LBO occurred at t=63 s. The number of events and *SI* at a time *t* are obtained from the low-pass filtered CH^* signal, during *t*-1 s to *t*. The same optimal event detection settings presented above are used here. Far from

LBO, the number of detected events is nearly zero, with occasional events seen between Φ/Φ_{LBO}=1.45-1.2. Events start to appear frequently at Φ/Φ_{LBO}=1.2 (t=35 s). The event occurrence rate appears to vary widely at this point, ranging from 1/sec to 5/sec between Φ/Φ_{LBO}=1.3 and 1.1 (i.e., t=60 to 68 sec). It then rises sharply at Φ/Φ_{LBO}=1.1. As expected, the *SI* provides a higher dynamic range, as events and *SI* are matched for Φ/Φ_{LBO}=1.1-1.06 (t=34-42 s). In addition, the *SI* appears to have a smoother, less noisy trend near LBO, compared to event occurrence rate.

The result demonstrates that an optical sensor monitoring LBO precursor events can be used as an input to a real-time LBO control system.

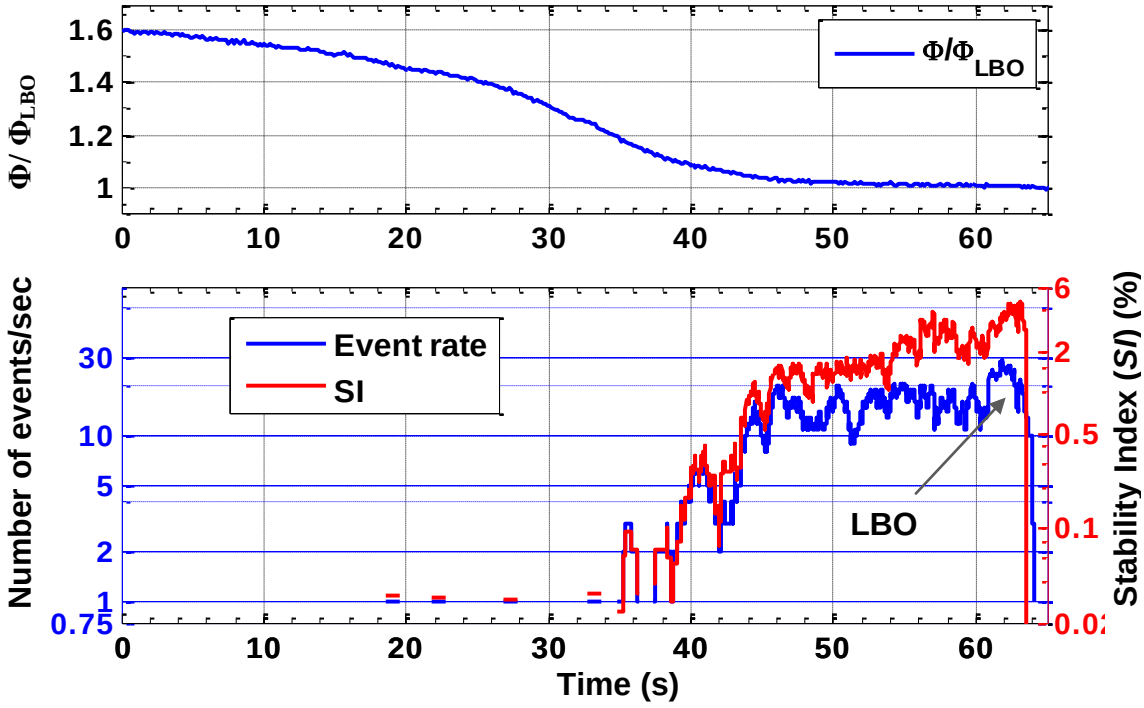

Figure 54. (top) Normalized equivalence ratio variation with time (bottom) Number of events and *SI* calculated in moving 1 s time windows.

4.2.4. CH* vs OH* Signals

The above results were presented for event detection using CH* chemiluminescence; the OH* signal is an alternative as both are generally proportional to

heat release rate. Precursor events detected in low-pass filtered CH^* and OH^* signals using the same event detection settings are presented in Figure 55. Both optical signals were acquired simultaneously with the same optical fiber probe, with the light exiting the probe split and sent to two spectrally filtered detectors, one for CH^* and the other for OH^*. With the same event identification settings, OH^* produces slightly higher event rates (0.3/s) far from LBO, whereas CH^* produced nearly zero events. In addition, OH* produces marginally higher event rates near LBO compared to CH^*. With the threshold settings modified to lower the OH* event rate far from LBO, the event rate near LBO is reduced to to about ~7/sec. This suggests some differences in the background CH^* and OH^* emissions, especially far from LBO. Since CH^* signals provided a better LBO proximity parameter in the present study, they are the focus of the results presented in this thesis.

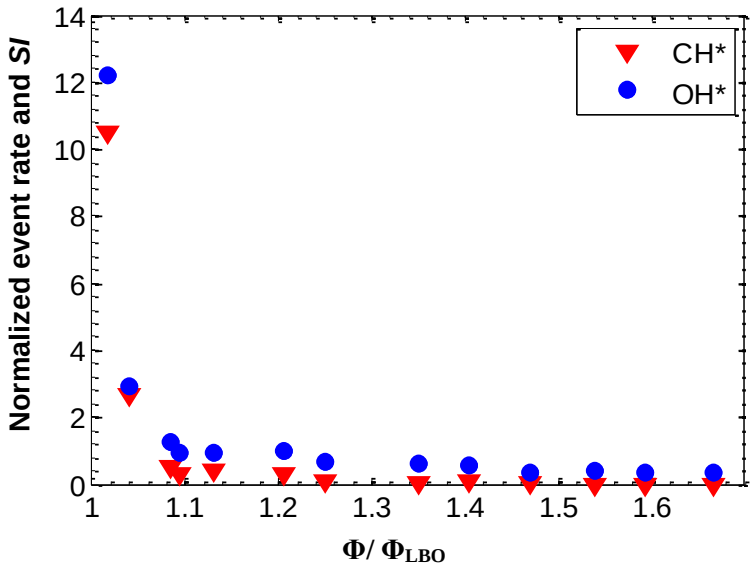

Figure 55. Average event rate from low-pass filtered CH^* and OH^* signals with same threshold settings.

Normalized unfiltered and low-pass filtered CH^* and OH^* signals, during a precursor detected in the filtered OH^* signal, far from LBO at $\Phi/\Phi_{LBO}=1.54$, are shown in Figure 56. In the filtered OH^* signal, the amplitude drop indicated by the arrow was detected as an event. However the corresponding filtered CH^* signal does not show any

amplitude drop. Examining the unfiltered signals OH^* signal shows amplitude drop similar to precursors, whereas CH^* does not show any such drop. The difference in signal features for OH^* and CH^* is not surprising, as the two respond somewhat differently to variations in heat release and unsteady combustion processes. For example, CH^* and OH^* emission respond differently to perturbations in local equivalence ratio and strain [79].

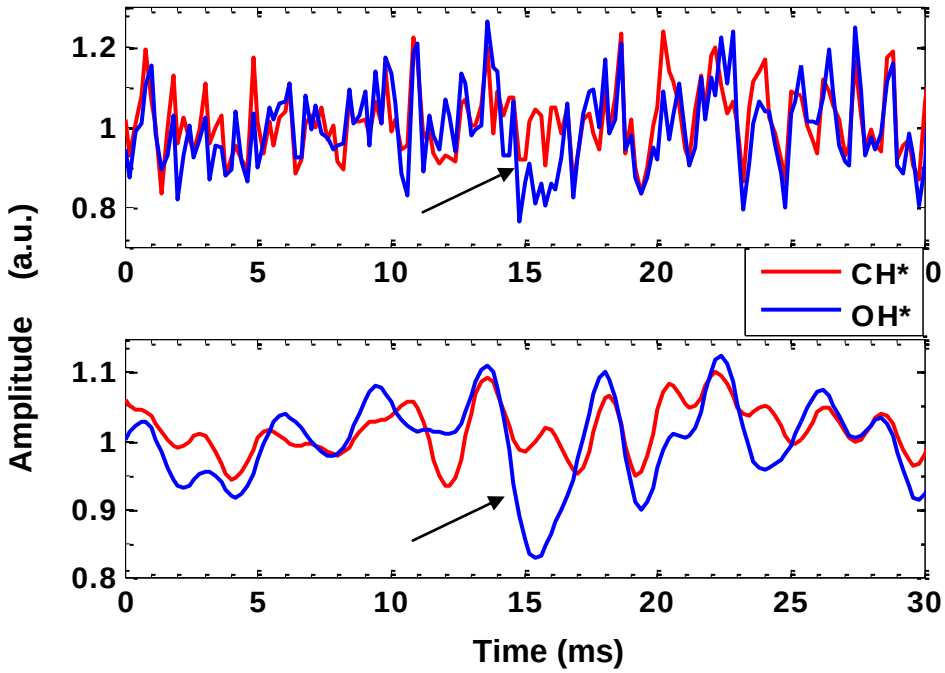

Figure 56. CH^* and OH^* signals during a precursor detected in the filtered OH^* signal; (top) unfiltered (bottom) low-pass filtered signals. ($\Phi/\ \Phi_{LBO}$=1.54).

4.3. Summary

This chapter investigated LBO margin sensing under high amplitude dynamic instability and under nearly realistic combustor operating conditions, i.e., elevated pressure and temperature operation. The LBO margin sensing approach was based on identifying flame extinction and re-ignition events (LBO precursors) in chemiluminescence signals.

LBO precursor events similar to those observed in dynamically stable conditions were also observed under high amplitude dynamic instability conditions, with two

distinct instability mechanisms (w/o Φ' and w/ Φ') produced by well-mixed and closed-coupled fueling in a gas-fueled combustor. Low-pass filtering applied to optical signals produced similar characteristic shape for precursors for all conditions, allowing for a single LBO precursor detection algorithm to be applied, as the results are relatively insensitive to changing level or type of dynamics. Precursor events detected in optical signals were observed to increase in number as LBO conditions were approached, providing a measure of proximity to LBO. Another parameter, Stability Index (*SI*), which combines event rate, duration and strength, produced a more robust LBO proximity parameter having higher dynamic range than the simple precursor event occurrence rate. On average, event rate near LBO was observed to be in the range of 1-2/sec and event durations in the range 20-50 ms.

The same LBO precursor detection approach was applied to a different combustor configuration, a liquid-fueled LDI combustor, operating at elevated pressure and preheat temperature. The combustor was observed to have a moderate level of dynamic instability, with multiple frequencies. Near LBO, the combustor exhibited partial extinction and re-ignition events. These events were observed to have much shorter durations (1.5-3ms) compared to the gas fueled combustor. The durations are similar to dynamic instability time periods (1.4-1.7ms). In optical signals some of these events were observed, however, others were obscured to some extent by dynamic instability and other high frequency noise. Nevertheless, low-pass filtering enabled robust event detection. In optical signals CH^* produced more number of events near LBO compared to OH^*, suggesting CH^* is a better choice. The detection approach was demonstrated to be capable of detecting LBO margin in real-time.

CHAPTER 5

LBO MARGIN SENSING: ACOUSTIC DETECTION

In addition to optical emissions, acoustic emissions can be used for monitoring LBO precursor events, as acoustic radiation is proportional to the time derivative of the heat release rate. During precursor events, the drop and rise in heat release can be expected to produce a corresponding acoustic signature. This chapter examines precursor event detection and LBO margin sensing using acoustic signals in the gas-fueled and LDI combustors. Acoustic data was acquired simultaneously with the optical results presented in the previous chapter. In the gas-fueled combustor, acoustic signals were acquired with a microphone located outside the combustor, while in the LDI combustor they were acquired with a piezo-electric transducer mounted on a standoff tube as described in Chapter 3.

5.1. LBO Margin Sensing in the Gas-Fueled Combustor

An acoustic signal and a simultaneous OH^* chemiluminescence time trace during a precursor event for dynamically stable operation are shown in Figure 57. The acoustic data exhibit a low level of coherent oscillations, which are less evident in the optical signal. The time delay between the acoustic and optical signals is about 2-3 ms based on the acoustic travel time from the combustor to the microphone. In the acoustic signal, a precursor event signature can be seen around the time when the optical signal shows re-ignition. The extinction phase does not produce a clear acoustic signature, probably due to the slow rate at which the heat release drops in this case. The re-ignition appears more rapid, with the heat release rate overshooting the nominal heat release rate, probably due to rapid burning of reactants present in the extinguished region. It should be noted that the optical signal here corresponds to a small region above the combustor inlet, thus it

represents local heat release. On the other hand, the acoustic signal is due to global heat release variations.

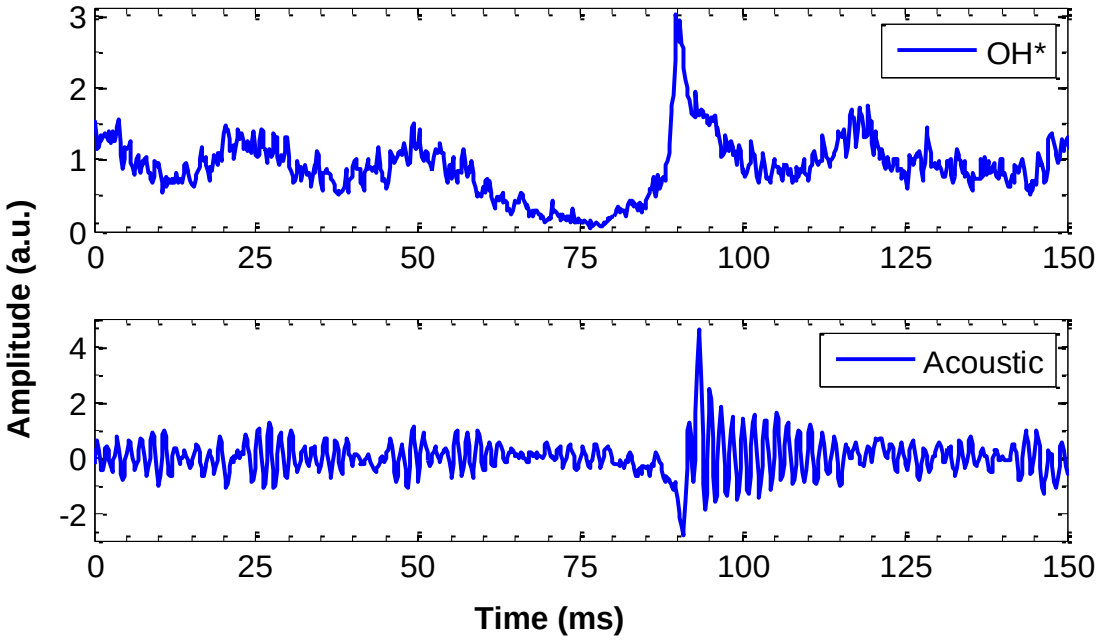

Figure 57. (Top) Precursor event in the OH* signal for dynamically stable operation with a precursor event at ~50-90 ms; (bottom) simultaneous acoustic signal.

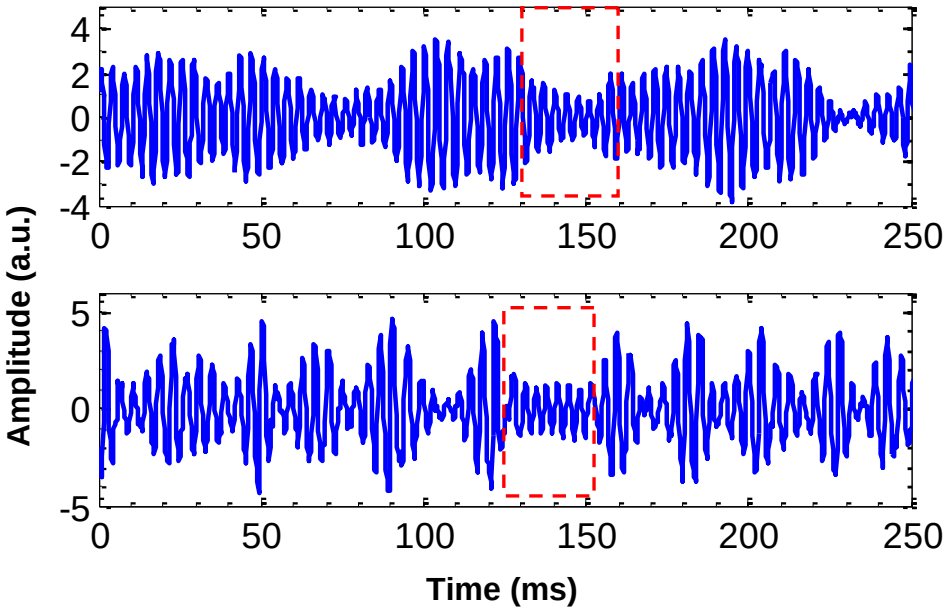

Figure 58. Acoustic signals during precursor events observed in optical signals (Figure 32) for instability w/o Φ' and w/ Φ'.

Acoustic signals, acquired simultaneously with the optical signals of Figure 32(Chapter 4) for instability w/o Φ' and w/ Φ', are shown in Figure 58. The time windows where optical precursors were observed are indicated by boxes. For both instability cases, the oscillation amplitude is reduced during the precursor. However, the reduction in oscillation amplitude is not limited to the precursors. For example for instability w/o Φ', the oscillation amplitude drops around 75 ms and 230 ms, though the optical signal did not show any corresponding precursors. In addition, the oscillation amplitude drops frequently for instability w/ Φ' due to its inherent amplitude modulation. Therefore, a reduction in dynamic instability amplitude cannot be considered a precursor event signature, as it is not uniquely attributable to the occurrence of precursor events. From a visual inspection, there is also no other clear sign of a precursor event in the raw acoustic signals during strong combustion dynamics.

Given the success of low-pass filtering for suppressing the combustion dynamic component in the optical signals, low-pass filtering at 50 Hz was applied to the acoustic signals for the dynamically unstable cases. The results, along with a result for a dynamically stable case, are shown in Figure 59. These traces correspond to the raw acoustic signals in Figure 57 and Figure 58. Low-pass filtering was performed with an 8^{th} order digital Butterworth filter. In the figure, the signal amplitude of the stable mode was reduced by a factor of 5 to put it on the same scale with the unstable cases.

Though there was no indication of precursor events in the raw acoustic signals during instability, clear precursor event signatures can be seen in the filtered signals. It is likely that in the raw acoustic signals, precursor events have much smaller amplitudes than the instability and are therefore obscured. By suppressing the instability, the precursor signature is revealed. All three precursors have nearly the same characteristic shape, and hence the same event detection algorithm can be used for their detection. For the precursors, the downward portion of the event signature is more pronounced than the

upward portion, possibly due to the effect of filtering. Since the upward part of the signature comes later in time, filtering would tend to add a portion of the downward signal to the upward, thus suppressing the latter more. For instability w/ Φ', the upward modulation is relatively smaller than the other two cases, and this behavior has been observed to be consistent for many other precursors. The smaller upward modulation could be due to a faster time scale for re-ignition, and thus it is suppressed more by low-pass filtering.

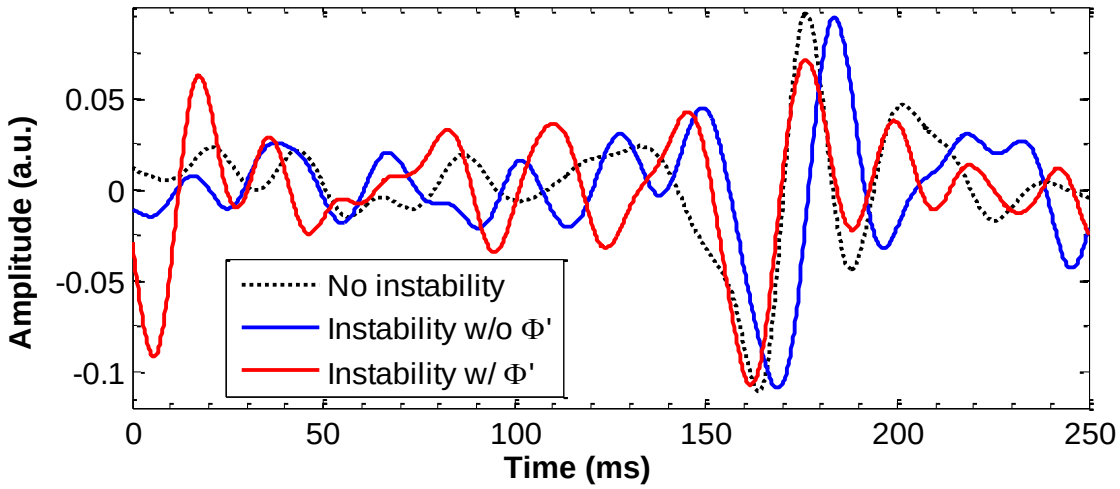

Figure 59. Low-pass filtered acoustic signal with precursor events for dynamically stable and unstable w/o Φ' and w/ Φ'.

Precursor events in the filtered acoustic signals can be detected based on the downward modulation feature alone, as the upward modulation is not as strong. Results of event identification for all three cases of operation, obtained from low-pass filtered signals, are shown in Figure 60. For event identification, a lower threshold of μ-4σ was used. In the threshold calculation, amplitude excursions above and below the 3σ limit and the signal during precursors are omitted.

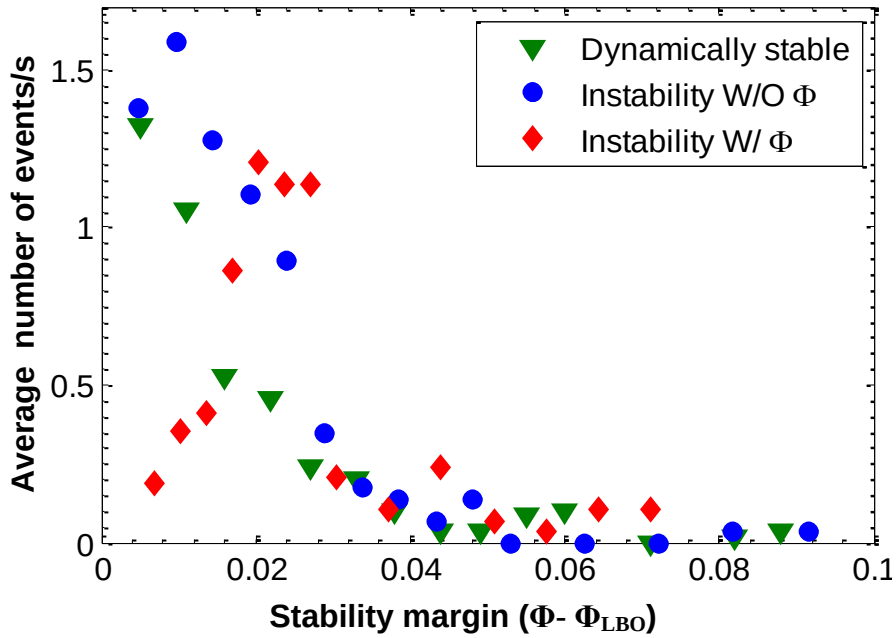

Figure 60. Average event rates obtained from low-pass filtered acoustic signals for dynamically stable and unstable conditions.

Events for the dynamically stable mode and unstable mode w/o Φ' provide the desired trend, a nearly monotonic increase in average event occurrence rate as LBO is approached. In addition, event rates are similar to the rates obtained with optical detection. On the other hand, for instability w/ Φ', the event rate increases initially towards LBO, but then drops. This is due to the lack of a significant precursor signature for very long duration precursors, which occur close to LBO. The long duration precursors did not produce noticeable precursor signatures, probably due to the slower changes in heat release compared to the other two cases.

5.2. LBO Margin Sensing in the LDI Combustor

For comparison, an acoustic signal from the LDI combustor is shown in Figure 61, along with its 500 Hz low-pass filtered version. Results are shown during times when a precursor event was observed in the optical signal (Figure 46-Chapter 4). The time delay between the `optical and acoustic signals is about ~1.5 ms, based on the travel time to the acoustic pressure sensor. The time windows where the precursor signatures are

expected (from the optical detection) are indicated by boxes. The behavior of the raw acoustic signal during these instances is not noticeably different from other times. The filtered signal does not show significant improvement either, except for slightly longer features. Unlike the gas-fueled combustor results, where filtering made precursor signature conspicuous, the same behavior was not observed for the LDI combustor.

The absence of clear precursor signatures in the acoustic signal for the LDI combustor could be due to smaller changes in heat release during precursors. Compared to the gas-fueled combustor, the extent of flame extinction and consequently the re-ignition is much smaller. This would produce smaller fractional variations in heat release, and therefore weaker acoustic signatures. Another possible reason is that in the LDI combustor, the dynamic instability period is comparable to the precursor event duration, which would limit the effectiveness of filtering in separating precursors from dynamics. Finally, reflections of the precursor pulse from combustor boundaries may play a role as well. These latter two issues are examined in the following sections.

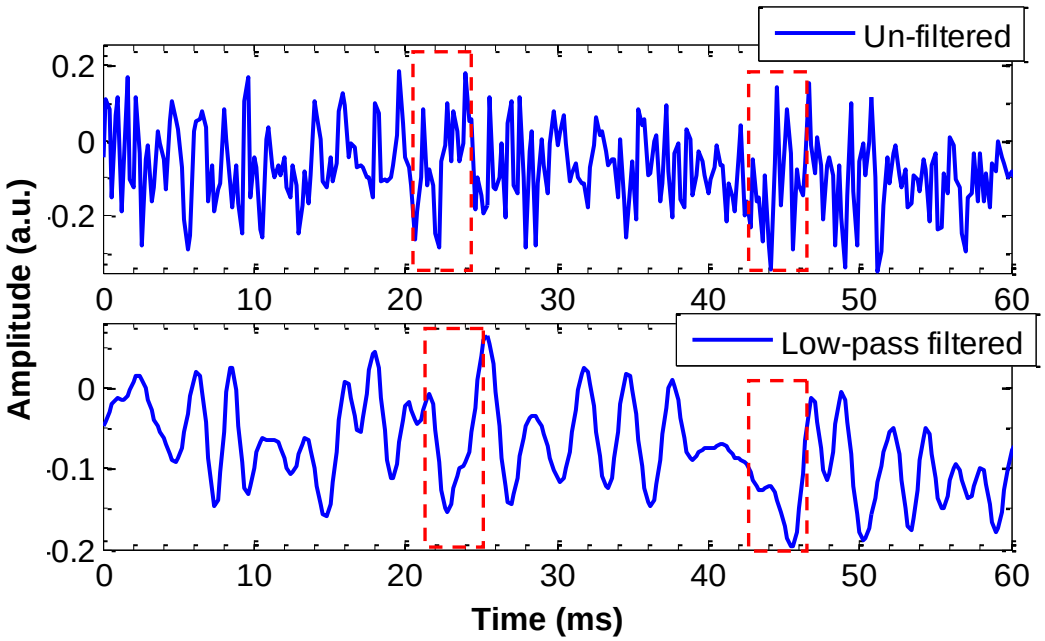

Figure 61. (Top) Raw acoustic signal time trace from the LDI combustor during precursor events observed in optical signals, as marked by boxes; (bottom) low-pass filtered signal.

5.3. Effect of Instability and Precursors Timescales

When the duration of precursor events and the dynamic instability period are sufficiently different, filtering can be applied to separate precursors from dynamics. However as the time scales of both get closer, filtering can be expected to be ineffective. This is one reason filtering may have failed to reveal precursor signatures in the LDI acoustic signals. The problem might be expected to exist for optical signals as well, if precursors have weak signatures and the dynamics are strong enough to obscure them. To address possible differences between the two detection approaches, we can analyze the limitations of filtering when the instability period and precursor event durations are nearly the same. Since filtering separates signals based on their spectral content, the spectra of precursors relative to that of the dynamic instability needs can be analyzed.

Ideally, combustion dynamics produces harmonic oscillations in heat release and pressure. The signals usually have spectra that are narrowband, with peaks at the instability frequencies. However, amplitude variations and phase drifts can result in some broadening of the instability spectra. Precursor events are discrete and occur intermittently at a low rate (usually below 10-20 events/sec). Such discrete events have wide frequency content due to their non-periodic nature [80]. This behavior is similar to spectral leakage arising from using a finite time interval for spectral evaluation of a periodic signal. For example, if spectrum of a periodic signal is evaluated over only one cycle, the spectrum would be broad due to convolution with the spectrum of a boxcar truncation function [80].

Model optical and acoustic precursor event time traces, along with their amplitude spectra are plotted in Figure 62. An optical precursor event is generally an inverted, single peak curve, and can be modeled by Eq. (5.1). The acoustic precursor source event, given by the time derivative of the optical precursor, is given by Eq. (5.2). In the figure, the duration of precursor events is normalized to have a unit time scale. Similarly in the

spectra, a unit frequency corresponds to the inverse of the precursor time scale. As seen in the amplitude spectra, both precursors have quite broad spectra. For a dynamic instability having the same period as the precursor duration, the spectrum would be narrowband with unit center frequency. This suggests that even if the durations of the precursors and the instability period are similar, filtering (low-pass or a narrow bandpass around instability frequency) would still be effective in improving precursor signatures. The acoustic precursor has a relatively higher amount of power above unit frequency compared to the optical precursor. Hence, low-pass filtering will tend to suppress acoustic precursors more than the optical precursors.

$$\dot{Q}(t) = 1 - 0.5e^{(-t^2)} \quad \forall -2.5 \le t \le 2.5 \tag{5.1}$$

$$p(t) = te^{(-t^2)} \quad \forall -2.5 \le t \le 2.5 \tag{5.2}$$

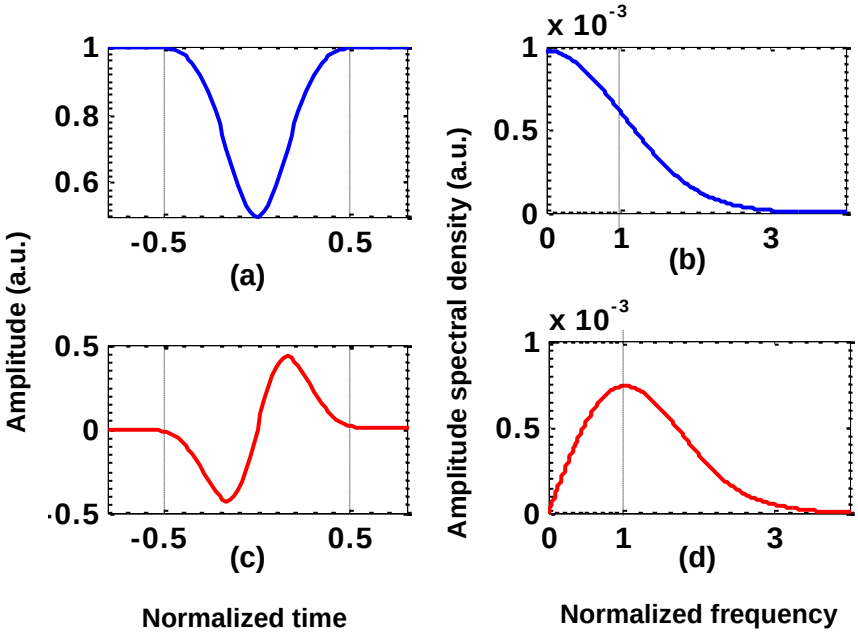

Figure 62. Precursor events and their spectral content: (a) optical precursor, (b) its amplitude spectrum, (c) acoustic precursor, and (d) its amplitude spectrum.

The effectiveness of filtering in revealing precursors in the presence of instabilities, when both have the same time scales, is illustrated in Figure 63. The instability signal is modeled by a *sine* function with a unit period, having a peak-to-peak amplitude of 2 units. In addition, Gaussian noise having a standard deviation of 0.1 units is added to the instability signals. The downward peak of the optical precursor has an amplitude of 0.5 units, whereas the acoustic precursor has a peak-to-peak amplitude of 1 unit. Optical and acoustic precursors are added to the instability signal, at a time of 5 units, which corresponds to the zero phase of the instability signal. Raw signals, low-pass filtered with an 8^{th} order Butterworth filter at a cutoff of frequency of 0.6 units (instability frequency =1 unit), are also shown in the figure.

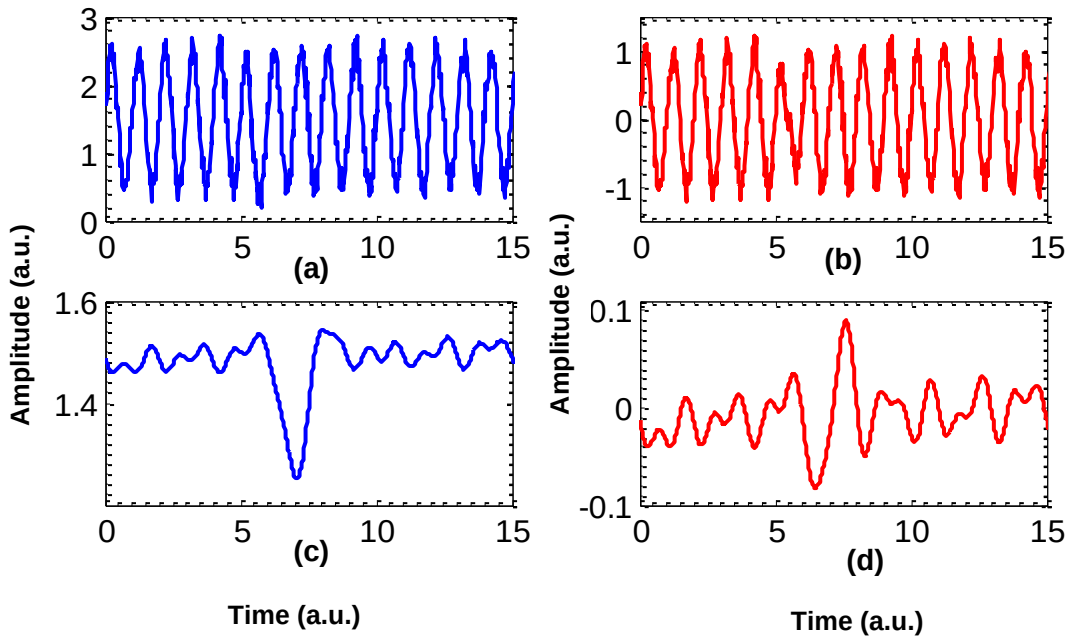

Figure 63. Model optical and acoustic signals with instability and precursors having similar time scales: (a) optical instability signal with a precursor; (b) acoustic instability signal with a precursor; (c) low-pass filtered optical signal; and (d) low-pass filtered acoustic signal.

In the raw signals, there is no discernible precursor. However, the filtered signals clearly show the precursors. This is due to the above observation that precursors have wider spectral bands compared to the instability. In the filtered results, the signal-to-noise ratio is higher for the optical precursor compared to the acoustic precursor. This is due to the acoustic precursor having more frequency content above the filter cutoff of compared to the optical precursor. Thus the acoustic precursor is suppressed more by the low-pass filtering. In addition, similar simulations show that the shape of the filtered optical precursor is relatively insensitive to the phase at which the precursor occurs. On the other hand, the relative magnitudes of the downward peak compared to the upward peak of the filtered acoustic precursor are sensitive to the phase.

5.4. Effect of Reflections on Acoustic Precursor Detection

The acoustic pressure measured by a transducer at any given time is not due solely to acoustic emission produced at a single instance. It has components of acoustic emissions from a range of previous times, due to reflections from boundaries. This is less of an issue for optical detection, because the propagation time of light makes any reflections nearly simultaneous with the original. Thus one might expect that in addition to the acoustic precursor pulse traveling directly from the source, i.e., the location in the flame where extinction and re-ignition occur, there will also be reflections of the acoustic pulse from the combustor boundaries. These reflections can overlap with the actual precursor signal at the transducer and may corrupt the expected precursor signature.

5.4.1. Acoustic Model

To examine the effect of reflections on detection of acoustic precursors, a simple combustor model was developed (see Figure 64). The model consists of two regions with different impedances, Z_1 and Z_2, separated by a thin flame. The flame is assumed to stand at a distance of L_1 from the inlet. The two impedances, Z_1 and Z_2, are given

by $Z = \rho C$ where ρ is density of the medium and C is the speed of sound. The impedance to the right of the tube exit boundary is given by (5.3), which takes into account the end correction and mean flow for an un-flanged tube [81]. In that equation, k is the wave number, a is the tube diameter and M is the flow Mach number. Though the precursor pulse has a range of wave numbers (frequencies), a single wave number is used, based on the inverse of the precursor duration. Correction to the tube length due to the end wall is also applied, as given by $\Delta l = 0.613a$. Reflection and transmission coefficients for a pulse traveling from left to right at a boundary are given by Eq. (5.4) and Eq. (5.5). The reflection coefficient at the inlet boundary is calculated based on area change at the inlet given by Eq. (5.6).

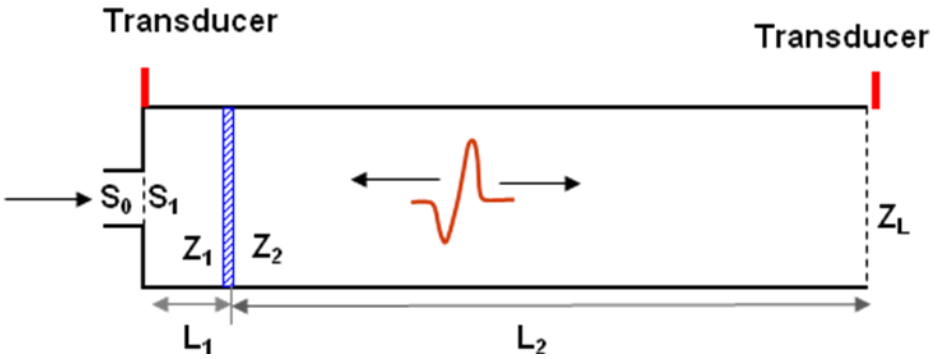

Figure 64. Schematic of acoustic model system used to investigate the influence of reflections on the detected acoustic pressure signal. The flow inlet is at the left; two possible transducer locations are indicated.

$$Z_L = \rho C\left(\left(\frac{(ka)^2}{4} - i0.613ka\right) + M_L\right) \tag{5.3}$$

$$R_{l,r} = \frac{Z_r - Z_l}{Z_r + Z_l} \tag{5.4}$$

$$T_{l,r} = 1 + R_{l,r} \tag{5.5}$$

$$R_{1,0} = \frac{S_1 - S_0}{S_1 + S_0} \tag{5.6}$$

It is assumed that the acoustic precursor originates at the flame and produces waves traveling to the left and right. The left going wave gets partially reflected from the inlet, while the right going wave is reflected from the exhaust. Also, each time a wave goes through the flame, it becomes two waves, one reflected and the other transmitted. This gives rise to numerous waves crisscrossing inside the combustor. Pulses are dissipated at the inlet and tube exit due to the reflection coefficients being less than one. Dissipation at the tube wall boundary layer by thermal and viscous losses is neglected here, as it is usually small for short tube lengths [81]. The signal measured by a transducer is a superposition of the multiple pulses separated by different delay times.

To simplify the implementation of this model, the relative strength of the reflections can be considered. Reflections by the inlet and tube exit are considerably stronger ($R_{1,0}$ and $R_{2,L}$ ~0.9) than the reflections at the flame boundary ($R_{1,2}$ ~0.25 for LDI and ~0.4 for the gas-fueled combustor). Therefore up to 15 reflections by the inlet and tube exit are accounted for in the current analysis, whereas flame reflections are truncated after two or three reflections. For example in the LDI combustor model, the amplitude has dropped to ~6% of the original pulse amplitude by the second flame reflection, and by the third reflection, the amplitude is as low as 1%. Thus only two flame reflections are considered. In the gas-fueled combustor, the 4^{th} reflection amplitude drops to ~3% and hence three flame reflections are included. The pressure transducer is assumed to be mounted either at the inlet similar to the LDI setup or at the tube exit, similar to the gas fueled combustor setup.

5.4.2. Model Results for LDI Combustor

The model parameters required to simulate the LDI combustor are: L_1 = 30 mm, L_2= 270 mm, T_1=700K, T_2=1970K and P=2atm. The resulting reflection and transmission coefficients are $R_{1,0}$=0.89, $R_{2,L}$= -0.88, $R_{1,2}$= -0.25, $R_{2,1}$=0.25, $T_{1,2}$=0.75 and $T_{2,1}$=1.25. In calculating $R_{1,0}$, S_0 included the open area of the swirler and the perforated plate hole area. The acoustic precursor is assumed to have a shape as shown in Figure 62(c), with a duration of 2 ms, and it is created at time zero.

The original precursor generated by the flame, i.e., reaching the transducer without any reflections and denoted the *initial* precursor, and the precursor signal with reflections are shown in Figure 65. Reflections produce a ringing behavior in the precursor signal seen by the transducer. Ringing is due to the reflected precursor pulses reaching the transducer with different time delays and the decay of the amplitude by each reflection. Thus the ringing is periodic with a slow decay, and resembles a typical instability signal. The amplitude spectra of the initial and reflected precursors are shown in Figure 66. Unlike the initial precursor with its power distributed over a broad range of frequencies, the reflected precursor has the majority of its power in a narrow band, centered at ~610Hz. In addition at low frequencies (<300 Hz), the reflected precursors has nearly half the power of the initial precursor. The natural frequency of the combustor duct can be calculated using the boundary conditions $P'_1 = P'_2$ and $\rho_1 U_1' = \rho_2 U_2'$ at the flame boundary along with U'_0=0 at the inlet and P'_L=0 at the tube exit. The calculated fundamental natural frequency of the combustor duct is 630 Hz. Therefore reflections result in a precursor signal having nearly the ringing frequency as the combustor's natural frequency, which is usually the frequency for combustors exhibiting longitudinal dynamic instability. This makes it hard to separate the precursor from dynamic instabilities. This result, reflections generating a precursor signal at the duct natural frequency, is not surprising. For example, for a closed open duct, the periodicity of pulses reflecting back and forth is $4L/C$ and the inverse of it is the natural period of the duct.

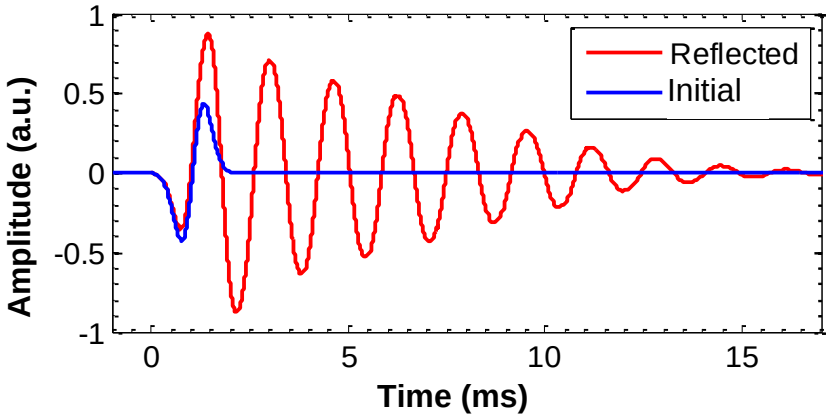

Figure 65. An acoustic precursor reaching the transducer without any reflections (initial precursor) and the resultant of multiple reflections (reflected precursor).

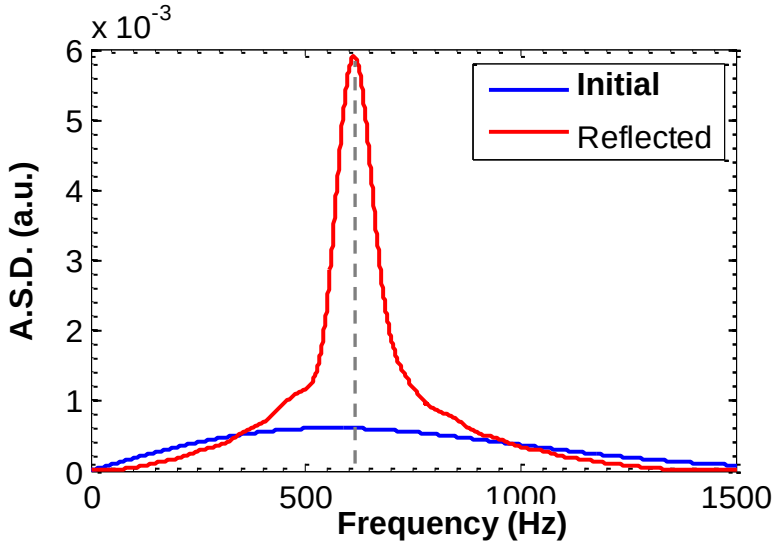

Figure 66. Amplitude spectra of the initial and reflected precursors.

In order to investigate the limitations of filtering for separating the reflected precursor from dynamics, the reflected precursor is added to an instability signal at 630 Hz. The peak-to-peak amplitude of the instability signal is taken to be 6 units. In addition, Gaussian noise with a standard deviation of 0.05 units is added to the instability. Since precursors cannot be identified in raw signals under instability conditions, low-pass filtering was performed at 350 Hz with an 8^{th} order Butterworth filter. Raw signals along with low-pass filtered signals are shown in

Figure 67, for initial and reflected precursors added to the instability signals. The precursors added to the instability have amplitudes as shown in Figure 65. In the filtered signals, the initial precursor simulation results in a more distinct signature compared to the reflected precursor (same vertical axis scale for both). Though the reflected precursor is somewhat clear in this simulation, it may not be as evident in real combustor scenarios where combustion dynamics are more complex, with instability frequencies having a broader spectrum than simulated here. In addition, this analysis assumed plane wave propagation. In reality due to the non-planar nature of the initial precursor, reflections from the combustor duct walls may contribute to increased noise in the reflected precursor signal.

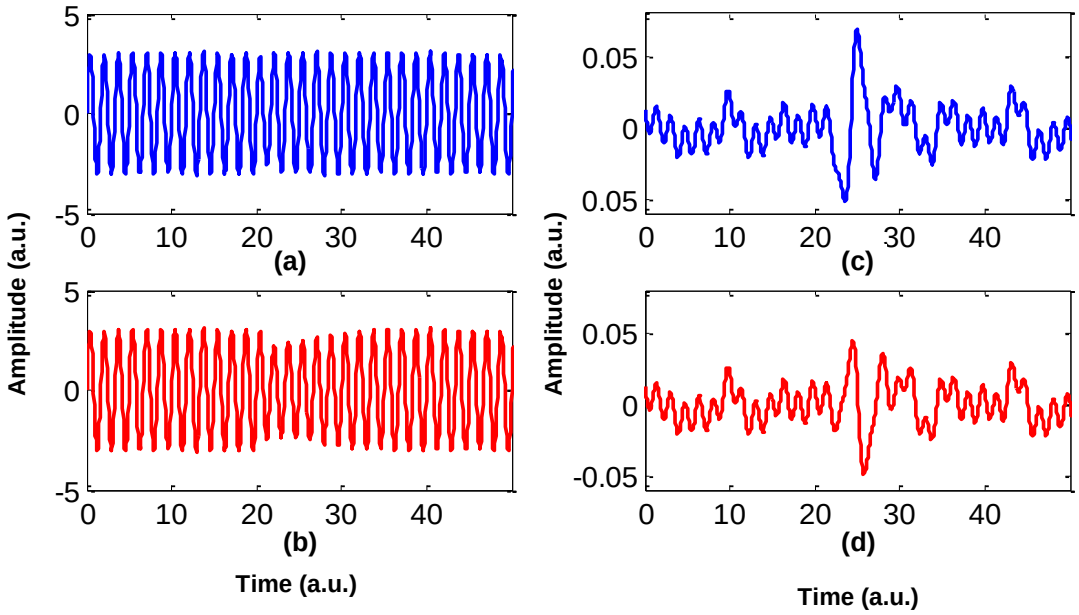

Figure 67. Model instability signals with initial and reflected precursors added to them: (a) instability signal with initial precursor; (b) instability signal with reflected precursor; (c) low-pass filtered version of (a); (d) low-pass filtered version of (b).

The signal characteristics of the reflected precursors depend on the duration of the precursor and the travel time inside the combustor, which depends on the combustor length. For example, Figure 68 shows reflected precursor signals with the initial precursor having different durations, in the same combustor geometry. Long duration precursors

(e.g., 8 ms) do not produce a noticeable ringing signal. This is due to the reflections having much shorter time scales than the precursor duration. All the reflections, before dying out, arrive nearly coincident with the initial precursor (this is closer to what would be expected for optical detection). The reflected precursor has a somewhat lower amplitude than the initial precursor. However, the precursor could be detected as it does not coincide with the instability signal. If the tube was long enough, the 8 ms precursor would also produce ringing, as the travel time becomes comparable to the precursor duration.

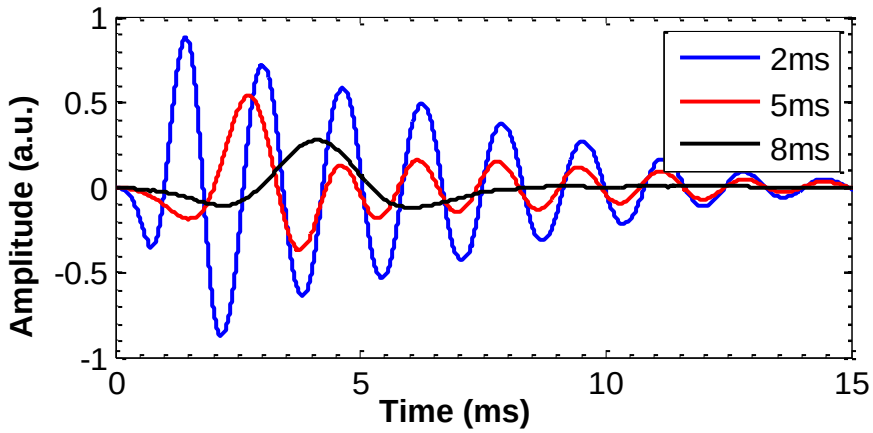

Figure 68. Simulated reflected precursor signals with the initial precursor having different durations in the LDI combustor.

5.4.3. Model Results for Gas-Fueled Combustor

The model parameters that match the conditions of the gas-fueled combustor are: L_1 = 50 mm, L_2= 550 mm, T_1=300 K, T_2=1830 K and P=1 atm. The resulting reflection and transmission coefficients are: $R_{1,0}$ = 0.97, $R_{2,L}$= -0.92, $R_{1,2}$= -0.42, $R_{2,1}$=0.42, $T_{1,2}$=0.57 and $T_{2,1}$=1.42.

Reflected precursors for different initial precursor durations are plotted in Figure 69. Long durations, e.g., above 10 ms, do not produce noticeable ringing. As such, we can conclude that the actual precursor durations in the gas-fueled combustor (generally above 5 ms) can be considered relatively large. Therefore, low-pass filtering helped with

precursor event identification in the gas-fueled combustor by separating the precursor from the dynamics.

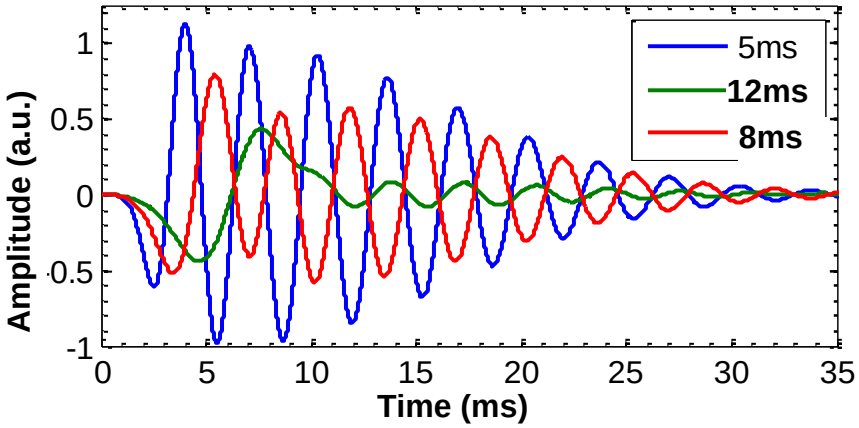

Figure 69. Simulated reflected precursor signals with the initial precursors having different durations in the gas-fueled combustor.

In addition to the above observations, the location of the pressure transducer along the combustor wall is an additional concern. In the gas-fueled combustor, the pressure transducer was located outside the combustor, which is qualitatively equivalent to locating it at the tube exit. On the other hand in the LDI combustor, the pressure transducer was located at the inlet. Both combustor geometries are approximately closed-open tubes, which produce an acoustic anti-node at the closed end (inlet) and a node at the open end (exit) for the standing wave expected for the case of combustion dynamics. The precursor pulse amplitude, however, is independent of axial location. Thus the higher pressure produced by the combustion dynamics at the inlet can more easily corrupt the precursor signals for the case of the pressure transducer at the inlet compared to the case where the transducer is near the exit. Hence for better detection of acoustic precursor events, the pressure transducer should be located near the combustor exit, where pressure oscillations associated with combustion dynamics are less pronounced.

5.5. Summary

LBO margin sensing using acoustic signals was investigated in the gas-fueled and LDI combustors. In the gas-fueled combustor, in the presence of strong combustion dynamics, no visible precursor signature was observed in the raw acoustic signals. Low-pass filtering, however, provided clear precursor signatures by suppressing the dynamic instability signal component. Precursors could be detected with a simple thresholding approach based on the depth of (downward) signal modulation during events. In the LDI combustor, neither raw signals nor low-pass filtered signals revealed reliable precursor signatures. One possible reason is the smaller heat release changes during precursors in the LDI combustor. Other possible reasons include, similar time scales for combustion dynamics and precursors in the LDI combustor, reflection of precursors from impedance discontinuities and, pressure transducer location.

Even if precursors have similar time scales as the combustion dynamic oscillations, they can be separated due to the wider spectral bandwidth of the discrete precursor events. The effect of precursor reflections from impedance discontinuities inside the combustor were examined by modeling acoustic reflections in a one-dimensional combustor geometry with an impedance jump caused by the flame and combustor boundaries. The reflections result in a narrow band ringing signal with a frequency similar to the combustor's natural frequency. This manifestation makes it difficult to separate precursors from combustion dynamics. The ringing is not significant if precursor durations are long compared to the round trip (acoustic) travel time inside a combustor. Finally it is postulated that for better detection of precursors in the presence of combustion dynamics, the pressure transducer should be located near the combustor exit, where the combustion dynamic pressure oscillations have lower amplitudes.

CHAPTER 6

LBO MARGIN SENSING: RAPID TRANSIENTS

The previous two chapters investigated the existence and sensing of LBO precursors in mostly steady-state operating conditions. In gas turbines, LBO could occur both during nominally steady-state operation and rapid power reduction transients. The current study, as well as previous efforts, have shown LBO margin can be effectively sensed during slow variations in equivalence ratio. The same may not be possible for rapid transients. Precursor events are discrete and occur intermittently. For a sufficiently fast transient, for example if the fuel flow rate is rapidly reduced to lower the engine power, a precursor may not occur before blowout occurs. Thus an approach is required to analyze the likelihood (probability) of events occurring before blowout during a transient.

This chapter examines the appropriate probability models that can capture statistical properties of precursor events. Using the statistical properties, probabilities for events to occur during rapid transients is examined. In addition implementation of LBO margin sensing during rapid deceleration transients in aircraft engines is examined.

6.1. Stochastic Model for Precursor Event Occurrence

At a given steady-state operating condition, precursor events occur sporadically, with a wide variation in time between successive events. For example in the LDI combustor at a nominally steady operating condition, the time between successive events was as small as 10 ms to as high as 500 ms. Such a large variation in the time between events is another indication of the random nature of the event occurrence, which should be predictable with probability models. Since precursors are discrete events, a common discrete event probability model such as Poisson distribution may predict the probability

for precursor event occurrence. The Poisson process has the property that the time between successive events follows an exponential distribution.

Empirical cumulative distribution functions (CDF) of the time between successive events (TBE), obtained from the LDI combustor data, are plotted in Figure 70. Events were detected in the low-pass filtered optical signals with the optimized threshold settings (lower threshold of μ-3.5σ and a minimum duration constraint of 1.4 ms, see Chapter 4). TBE is defined as the time between the starting times of successive events, with the start of an event considered to be the time when the signal amplitude goes below μ-0.25σ, during an event. In the figure, the empirical CDFs are compared with corresponding exponential CDFs. The CDF of an exponential distribution is given by Eq. (6.1), where λ is the average event occurrence rate (s^{-1}), and τ is the time between events (s). The event rate parameter λ is the inverse of the average time between events, which was shown to be a function of the normalized equivalence ratio ($\phi = \Phi/\Phi_{LBO}$) in Chapter 4.

$$F(\tau) = P(TBE < \tau) = 1 - e^{-\lambda(\phi)\tau} \tag{6.1}$$

The empirical CDFs for equivalence ratios closer to LBO (Φ/Φ_{LBO} =1.017 and 1.039) match quite well with the exponential CDFs, whereas for the equivalence ratios farther from LBO, the agreement is not as good. However, the mismatch is simply an artifact of having less data points (events) far from LBO. Sampled data probability distribution functions qualitatively appear close to theoretical distributions only if there are a sufficient number of data points to completely sample the distribution. Data for equivalence ratios even farther from LBO are not compared, as the number of captured events is even fewer, and a qualitative comparison could not be made. Though there is a good agreement between the empirical and theoretical CDFs near LBO for most of the time range, the theoretical distributions at smaller time scales, e.g., below 10 ms, have a higher probability than the empirical results. This is primarily due to the precursors

having finite durations; therefore the time between successive events cannot be smaller than this duration. There is no such constraint on the simple theoretical distribution used here.

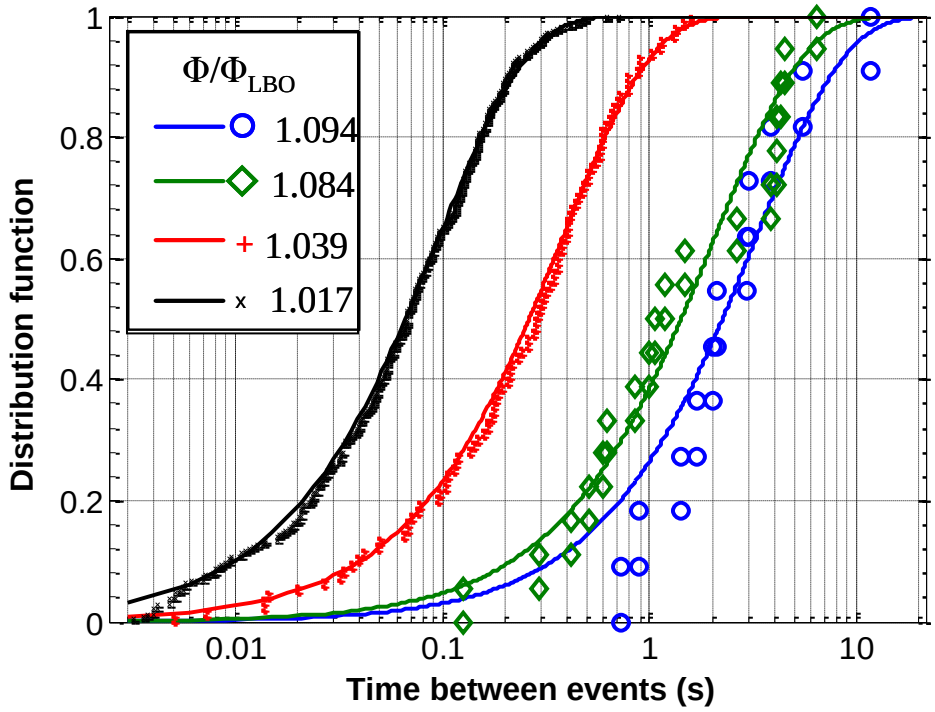

Figure 70. CDFs of measured time between successive events (TBE) for the LDI combustor (symbols) along with corresponding exponential CDFs (lines).

Besides the qualitative comparison of CDFs, quantitative approaches such as statistical hypothesis testing methods can be used for more accurate determination of the distribution assumption. One such approach is the Kolmogorov-Smirnov hypothesis test [82], which tests sampled data against its assumed distribution. The test is given by Eq.(6.2), where F is the empirical distribution, F_0 is the theoretical distribution, N is the number of samples and α is a given significance level. The hypothesis assumption is accepted if the maximum error between theoretical and empirical distributions is less than the test metric given on the right side of Eq. (6.2). The test results for the data of Figure 70 are given in Table 3, where the commonly employed 5% significance level was used for the test metric. The maximum error is 2.5-4 times less than the test metric for these cases. The results further validate the use of an exponential distribution hypothesis.

$$\max\left|F(\tau)-F_0(\tau)\right| < \sqrt{\frac{-1}{2N}\log\left(\frac{\alpha}{2}\right)} \tag{6.2}$$

Table 3. Kolmogorov-Smirnov hypothesis test results.

Φ/Φ_{LBO}	1.094	1.084	1.039	1.017
max|F(t)-F_0(t)|	0.158	0.132	0.03	0.021
Test metric	0.409	0.32	0.134	0.067

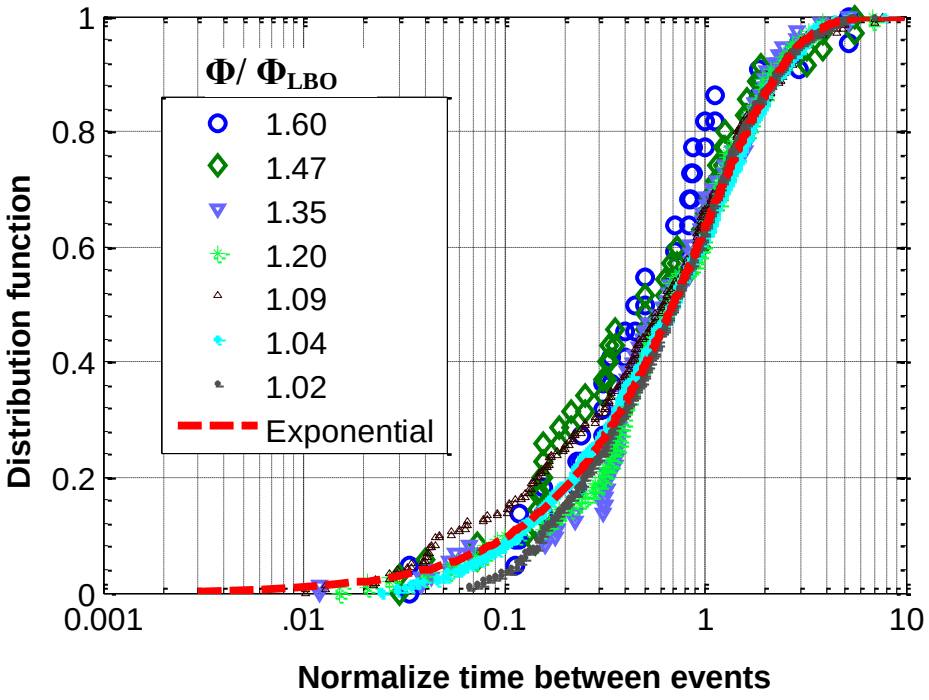

Figure 71. Empirical CDFs of the normalized time between events, with events detected using a threshold of μ-3σ. An exponential CDF with a unit mean time between events is also shown.

Empirical CDFs of the time between events, with events detected using a lower threshold closer to the signal mean (μ-3σ) and a duration constraint of 1 ms are plotted in Figure 71. With the relaxed detection threshold, the number of detected events increases significantly, with about 0.5-1 events/s events far from LBO and about 30 events/s near LBO. However, it should be noticed that these results contain some false events as well. In the figure, the time between events is normalized with the mean time between events for each operating equivalence ratio. Normalized in this way, all of the distributions

collapse to a single curve. The measured data is compared to a normalized exponential CDF having a unit mean time between events. With the modified thresholds and increased number of events, useful for the statistical comparison, the empirical CDFs are again in good agreement with the exponential CDF. The data again satisfy the Kolmogorov-Smirnov hypothesis test. This indicates that the form of the probability distribution does not change with small modifications of the threshold settings used for event detection.

Empirical and corresponding exponential CDFs for the data from the gas-fueled combustor are shown in Figure 72, for the case of instability without equivalence ratio oscillations. Events were identified in the low-pass filtered optical signals with the threshold settings that were observed to produce optimal event occurrence rate trend (see Figure 41 Chapter 4). Similar to the LDI combustor results, the time between events is well modeled by an exponential distribution. However very close to LBO (Φ/Φ_{LBO}=1.014), the empirical CDF appears to deviate from the exponential result for smaller values of TBE (t<0.2 s). Such behavior is probably due to the increased fraction of long duration precursors, as the precursor durations in the gas-fueled combustor are much longer than in the LDI combustor. For the gas-fueled combustion, the hypothesis testing results (not shown) again validate the use of an exponential distribution.

So for both the combustors, the time between events can be assumed with reasonable accuracy to have an exponential distribution. As mentioned earlier, a process characterized by discrete events, occurring randomly and with a TBE distribution described by an exponential is known as a Poisson process. Therefore the stochastic nature of event occurrence can be considered to follow Poisson statistics. Based on Poisson statistics, the probability of the number of events being *n* during a time interval Δt is given by the probability distribution function (PDF) in Eq. (6.3), where λ is the average event occurrence rate. The Poisson probability distribution is a widely used model for point processes, such as our precursor events. The model requires that events

occur independently of each other, which may be a reasonable assumption for the LBO precursors, at least when events are not too close together.

$$P(N_{ev}(\Delta t) = n) = \frac{e^{-\lambda \Delta t} (\lambda \Delta t)^n}{n!} \tag{6.3}$$

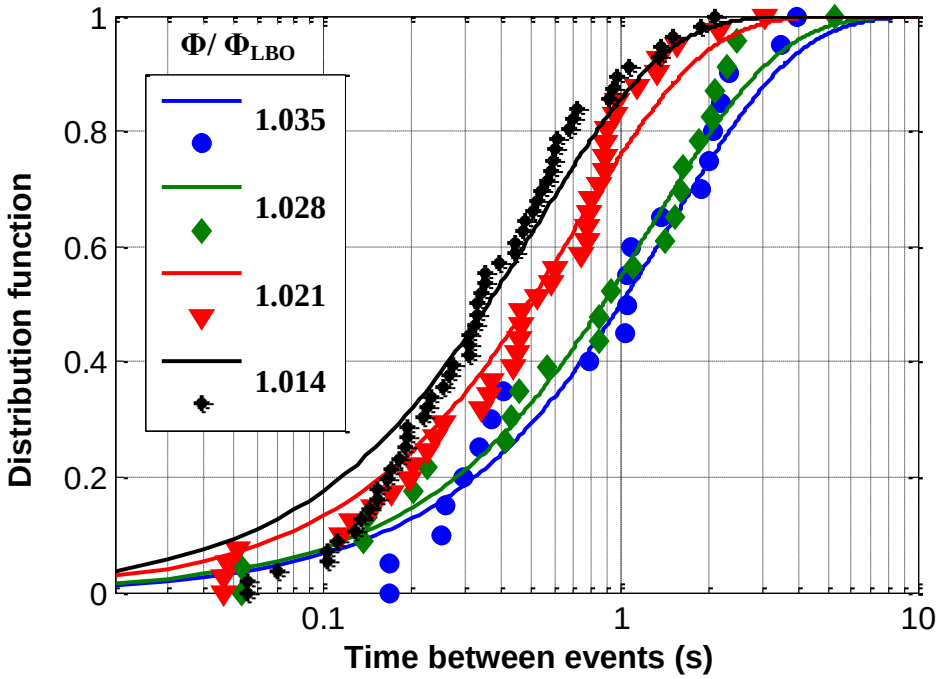

Figure 72. Empirical CDFs of time between events for the gas fueled combustor, having instability without equivalence ratio oscillations, along with corresponding exponential CDFs.

6.2. Probability of Precursor Event Occurrence in a Rapid Transient

The Poisson probability model described above is valid when the equivalence ratio is kept constant, i.e., for a stationary Poisson process. During a power reduction transient, the equivalence ratio changes with time. Assuming that at each point in the transient, i.e., for a given Φ/Φ_{LBO}, the stationary Poisson process would govern the event rate, then the transient process can be described as a non-stationary or non-homogenous Poisson process. For a transient having an equivalence ratio that changes with time, the total number of events expected during the transient is given by Eq. (6.4), where Λ is the

expected number of events, T is the transient duration and ϕ is the normalized equivalence ratio (Φ/Φ_{LBO}). In addition, the total number of events during the transient follows the Poisson distribution given by Eq. (6.5), where N is the total number of events in the transient. By specifying a given transient, $\phi(t)$, and for a given combustor's $\lambda(\phi)$, one can determine the probability of some minimum number (e.g., one or two) events occurring in a given transient.

$$\Lambda(T) = \int_0^T \lambda\left(\phi(t)\right)dt \tag{6.4}$$

$$P\left(N(0-T) = n\right) = \frac{\Lambda^n e^{-\Lambda}}{n!} \tag{6.5}$$

As an example, we can calculate the probability of events occurring within some time during a transient in equivalence ratio for the LDI combustor. In this example, ϕ (Φ/Φ_{LBO}) is reduced linearly from 1.20 to 1 at different rates. A value of ϕ=1.20 was chosen for the starting condition because the event rate in the LDI combustor began to rise at this equivalence ratio. The probability for at least one or two events to occur as a function of duration of the transient is calculated using the non-stationary Poisson distribution equations. A continuous function for event occurrence rate $\lambda=fn(\phi)$, required for the calculation, is obtained by curve-fitting the steady state experimental data. In the curve fit, the event rate far away from LBO is very small (<0.07 s^{-1}), therefore the contribution of false events to the calculated probabilities is negligible.

The probability of at least one or two events occurring is shown in Figure 73 as a function of the transient duration. The results are presented for events detected with two lower threshold values: μ-3.25σ and μ-3.5σ. With a required probability of 98% for at least one event to occur before LBO, the transient can have a duration no less than 2.35 s for the μ-3.25σ threshold case, and 3.35 s for the μ-3.5σ threshold case. For an increased

requirement of at least two events occurring, with two events providing a more certain indication of LBO proximity, the transients would have to be even slower (3.0 and 4.3 s for the two threshold cases). Since the result for the minimum required transient duration is contingent upon the value of ϕ where the transient starts, a better descriptor might be the equivalence ratio transient rate $d\phi/dt$. For at least one event to occur, the maximum allowed transient rate for the μ-3.25σ threshold is 0.085 s^{-1} and 0.059 s^{-1} for the μ-3.5σ threshold.

The probability for at least one or two events occurring in the gas-fueled combustor are shown in Figure 74, again as a function of the duration of the power transient. The transient starts at ϕ=1.06, where the event rate starts to increase. The results shown are for the case of instability w/o Φ' and detection using the optimal threshold settings (Chapter 4). With a 98% probability of at least one event occurring before the end of the transient, i.e., before LBO occurs, the reduction must occur over at least 4.85 s. The corresponding maximum transient rate is 0.012 s^{-1}, much lower than for the LDI combustor transient rate due to the lower event rate in the gas-fueled combustor.

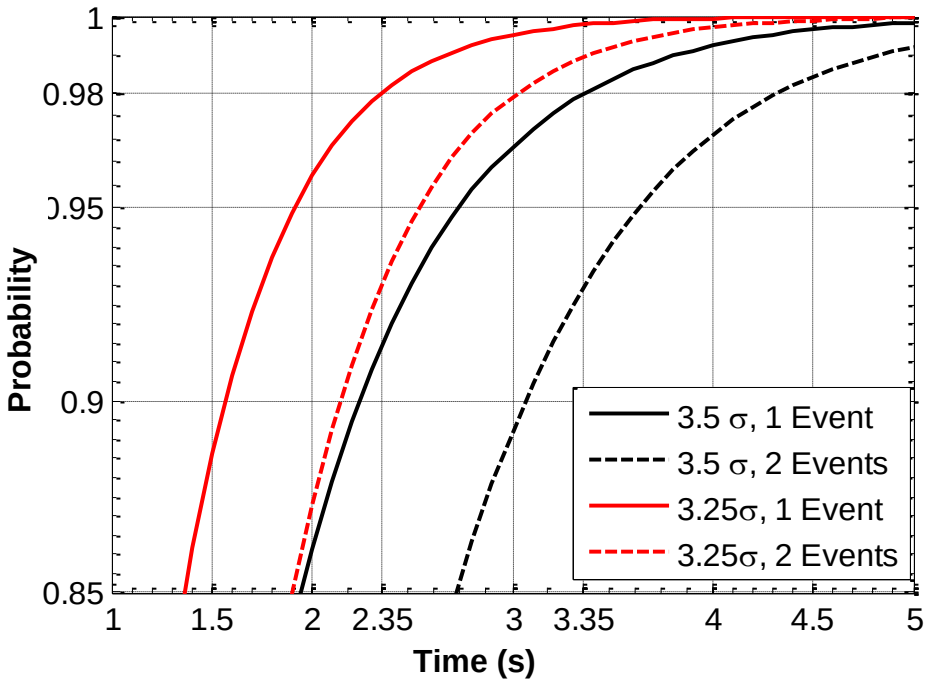

Figure 73. Probability of at least one or two events occurring for a linear transient in ϕ from 1.20 to 1, as a function of the transient duration. Results are based on the LDI combustor event rates.

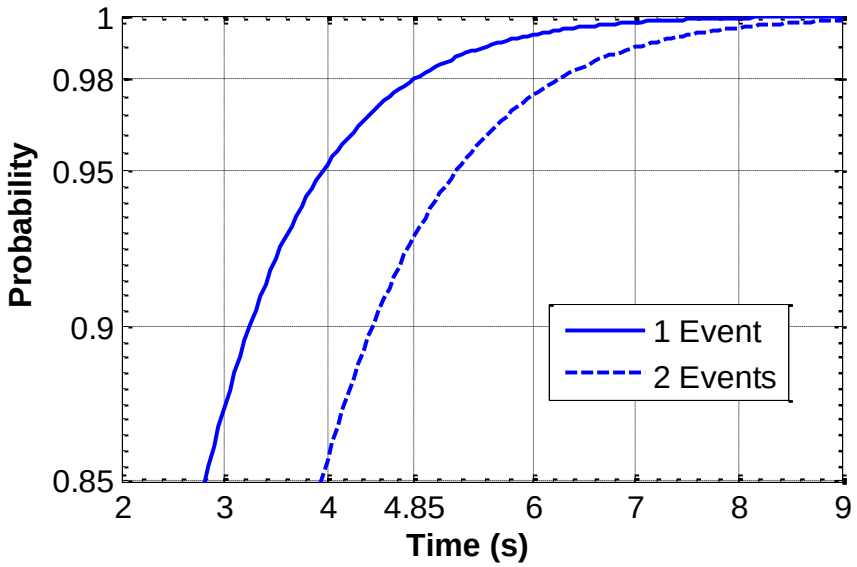

Figure 74. Probability of at least one or two events occurring for a linear transient in ϕ from 1.06 to 1, as a function of the transient duration. Results are based on the gas-fueled combustor event rates.

6.3. Precursor Event Simulation in Real-time

The characterization of the event rate as a Poisson process allows for simulations to test various aspects of LBO precursor sensing. One such example is the simulation of precursor events in real-time during a transient. This can be used to enable active LBO control simulations, without having to do costly experiments. A few algorithms exist for the simulation of non-stationary Poisson processes. However, only the algorithms capable of real-time event simulations are useful for control simulations. A common approach for non-stationary Poisson process event simulation is to use the thinning algorithm [83]. The algorithm requires the input of a maximum event rate (λ_{max}) that can be expected in the simulation. Next, the arrival time of the next event is generated using the maximum event rate. The generated arrival time is accepted with a probability of $\lambda(t)/\lambda_{max}$. If $\lambda(t)$ is small, such as what would be expected far from LBO, the generated event has a low probability of acceptance. The simulation algorithm is given in Table 4.

The simulation approach is tested for its capability to simulate events for a slow transient in equivalence ratio in the LDI combustor. The simulation results are presented in Figure 75. In the simulation, $\lambda(\phi)$ is obtained from a curve fit of the nominal steady-state data. From $\lambda(\phi(t))$ and the maximum event rate near LBO, the events are simulated in real-time. The simulation results agree reasonably well with the experimental data. It captures the general trend of fluctuations in number of events per second. It should be noticed that the simulation result varies from run to run due to the random nature of the simulation. The simulation slightly under- predicts the number of events farther from LBO, and slightly over predicts the events very close to LBO. The difference may be due to limitations of the simulation algorithm, and other simulation algorithms need to be investigated.

Table 4. Event simulation algorithm for non-stationary Poisson process.

1) Start at t=0

2) Generate uniform pseudo random number $U_1[0,1]$

3) Generate next event arrival time with the maximum event rate with exponential distribution and reset t to $t = t - \frac{1}{\lambda_{\max}} \log(U_1)$

4) Generate a second uniform pseudo random number $U_2[0,1]$ independent of U_1

5) If $U_2 \leq \frac{\lambda(t)}{\lambda_{\max}}$ then accept t

6) Go back to step 1

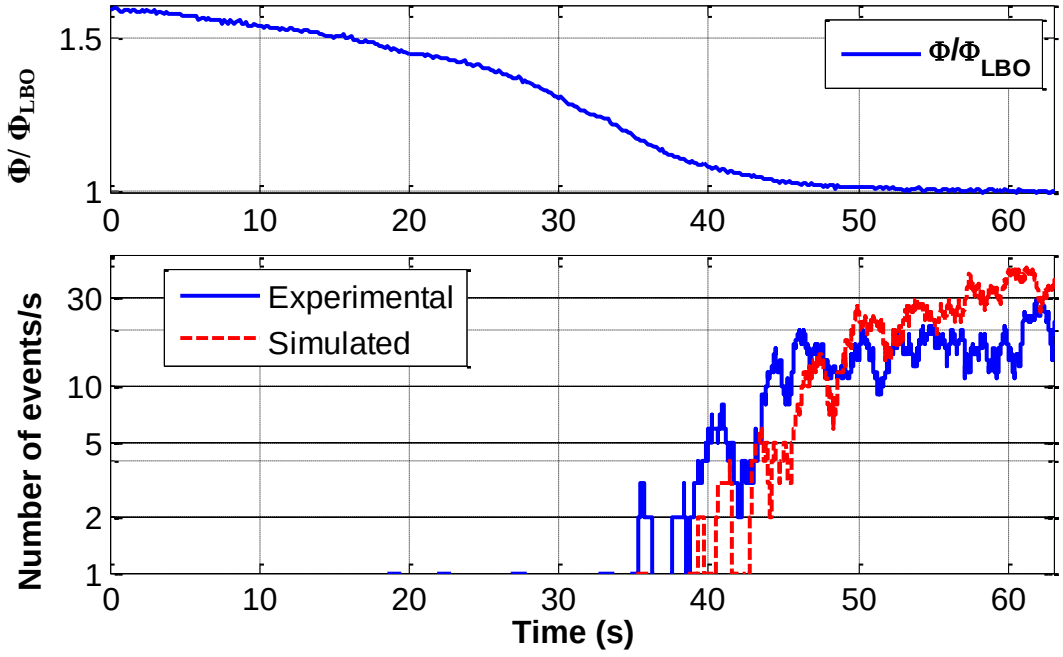

Figure 75. Experimental and simulated number of events in a one second interval

6.4. Time Response Improvement in Engine Decelerations with LBO Margin Sensing

As described previously, LBO can occur during deceleration transients in gas turbines due to excessively lean equivalence ratios resulting from the slow spool down response of engines. To prevent LBO during deceleration transients, current aircraft engine control systems commonly use a passive method that is based on placing a minimum limit on the Ratio Unit (RU) [75, 76]. As outlined in Section 2.5, RU is defined as *Wf/Ps3*, where *Wf* is the fuel flow rate and *Ps3* is the combustor inlet static pressure. Thus RU is an approximate measure of a combustor's overall equivalence ratio (see Appendix A). Current engine control systems likely use an excessively high margin for the RU limiter, because it only provides an approximate measure of the equivalence ratio, and because blowout limits are inherently uncertain. Such excessive margins limit the transient response of an engine during a deceleration.

If LBO margin sensors are employed, it can be speculated that the RU limiter might not be needed; instead, LBO prevention would be based on output from the margin sensors. However, such an approach could result in pushing the combustor through flame extinction and re-ignition events during each deceleration, which might not be preferable from an engine performance point of view. Therefore, the nominal LBO prevention approach based on the RU limiter could still be used, however with a lower LBO margin. Protection from LBO would be achieved with an LBO margin sensor-based controller to deal with infrequent near-LBO excursions. The potential advantage of this approach is that with a lower LBO margin used for the RU limiter, the transient response during decelerations can be improved.

In order to investigate the potential for improvements in transient response, along with other issues in LBO margin sensing, a turbofan engine simulation was implemented using the Numerical Propulsion System Simulation (NPSS) tool. The engine model and control scheme are described in Section 3.3 of the thesis. For the nominal engine control,

without LBO margin sensing, the RU limiter is set at 15.12 lb/hr/psi, which is slightly below the idle RU of 17.6 lb/hr/psi. To relate this to a standard combustion parameter, the combustor primary zone equivalence ratio corresponding to the nominal RU limit is about 0.58, assuming 27% of the total combustor air passes through the primary zone. The LBO precursors are modeled using the statistical methods described in the previous sections, and the statistics are based on the LDI combustor precursor results.

6.4.1. Transient Response Improvement

For the nominal case (without margin sensing), the LBO margin limit is assumed to be $\Phi/\Phi_{LBO}=1.35$. This is a reasonable assumption based on the observation that in the LDI combustor events start to occur at $\Phi/\Phi_{LBO}=1.20$, and one would expect the nominal margin to be where local extinctions are unlikely to occur. Based on this, the LBO equivalence ratio would be 0.43. However, the LBO limit cannot be a perfectly known value; it should be uncertain due to variations in temperature, strain, mixing, etc. So if the nominal RU limit is intended to reliably prevent blowout excursions, one can assume that the probability that LBO might occur at this nominal equivalence ratio is quite small. For example, one might expect LBO might occur at the margin limit only once in a million decelerations. Furthermore for this exercise, we assume that the equivalence ratio where LBO occurs follows a Gaussian distribution due to the random fluctuations in operating conditions. Using a probability of 10^{-6} for LBO occurring at the nominal limit equivalence ratio and the expected (average) LBO equivalence ratio of 0.43, the probability of LBO occurring at a particular equivalence ratio can be calculated. The Gaussian distribution of the LBO equivalence ratio and its CDF are shown in Figure 76.

The next step in the simulation is to choose a new, lower margin (minimum allowed equivalence ratio) for the case with LBO margin sensing. If successful, the control system should prevent the occurrence of LBO with the same reliability as the nominal margin without control, i.e., a probability of blowout occurring that is less than

10^{-6}. For this exercise, we choose the new limit as the point where the likelihood of LBO occurring is ~5%. The resulting minimum allowed equivalence ratio is 0.49. In the figure, the minimum allowed equivalence ratios for the nominal case (black circle) and the modified case (red circle) are shown. The reduction in minimum allowed equivalence ratio results in a corresponding reduction in the RU limiter from the nominal 15.12 lb/hr/psi to 13.32 b/hr/psi (a 12% reduction). Whether such a reduction results in appreciable improvement in transient response needs to be investigated.

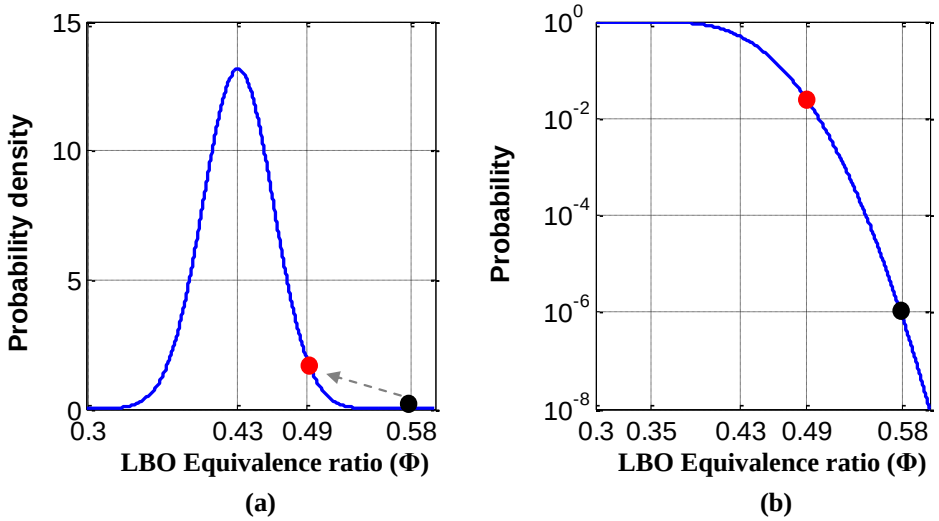

Figure 76. (a) Gaussian PDF of LBO equivalence ratio; (b) probability of LBO equivalence ratio being above a given equivalence ratio.

For the modified engine case, the RU limit is not suddenly reduced but is gradually reduced over a 2 s period after the nominal (original) RU limit is reached. A gradual reduction is necessary since the equivalence ratio has to be reduced somewhat slowly, in order to allow time for precursor events to occur. The RU traces for nominal and modified control, for a full power to idle transient, are shown in Figure 77. In Figure 78 corresponding thrust response at sea level static conditions is shown. The time required to reach 90% idle thrust level for the nominal limiter case is 6.6 s (measured from the initiation of the transient). For the modified limiter, the required time is reduced to 4.4 s, providing a 33% improvement transient engine response.

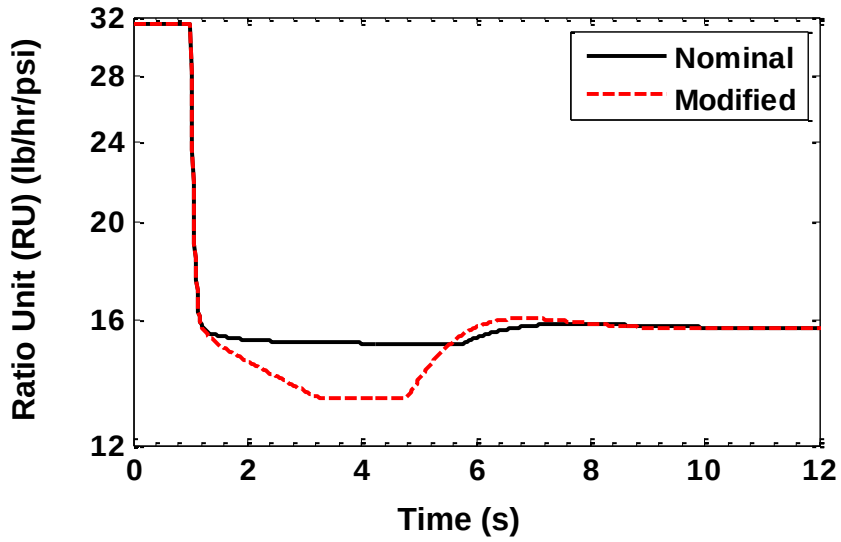

Figure 77. Engine Ratio Unit (RU) during a full power to idle transient for nominal and modified RU limit control cases.

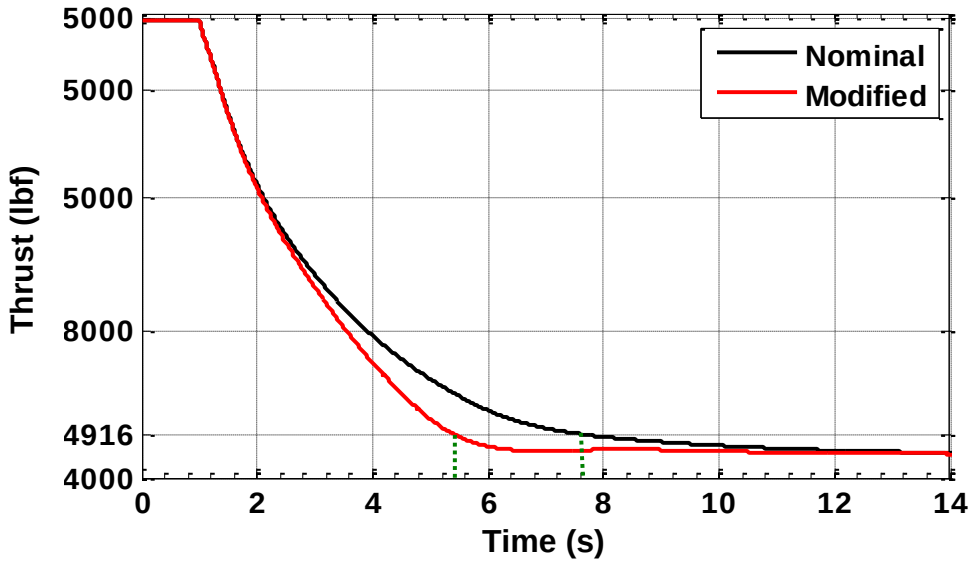

Figure 78. Thrust response for full power to idle transient at sea level static conditions with the nominal RU limiter and the modified RU limiter.

As noted before, the modified limiter approach should provide the same low probability of LBO occurring ($<10^{-6}$) as the nominal limiter case. For the modified case, the LBO margin sensor control is assumed to work if it can detect a precursor before the LBO limit is reached. Therefore, the probability of failure is based on the lack of an LBO precursor occurring before the transient reduction in equivalence ratio reaches the LBO

limit, which as noted above is also assumed to have a Guassian probability distribution. The LBO equivalence ratio probability and the probability of event occurrence can be combined in order to estimate the failure probability of the precursor event-based control system. For a transient in Φ, the probability of failure is the integrated product of LBO being at a given Φ and the probability that no event occurs before that Φ is reached, as given by Eq. (6.6).

$$P_{failure} = \int_{\Phi_1}^{\Phi_2} P\left(\Phi = \Phi_{LBO}\right) P_{no\,events}\left(\Phi\right) d\Phi \tag{6.6}$$

This failure probability is calculated for the modified limiter case above, based on the simulated equivalence ratio transient. The probability of no events is calculated using a similar approach as employed in Section 6.3, assuming LBO exists at a given Φ. For the calculation, different event rate trends obtained using different threshold settings for the LDI combustor data are used. The resulting failure probabilities and event rates are shown in Figure 79. Cases 1, 2 and 3 correspond to event rates obtained with lower thresholds of μ-3.5σ, μ-3.25σ and μ-3.0σ respectively. Recall that the less stringent threshold produces higher detected event rates. In the figure, the probability of failure is normalized with the required nominal probability of 10^{-6}. The failure probabilities are quite sensitive to the event rates. While Case 2 nearly meets the required "safety" constraint (10^{-6}), Case 1 results in a system that is 100 times more likely to blowout compared to the nominal case. Similarly, Case 3 exceeds the requirement by more than 3 orders of magnitude. However, it should be noted that the events detected based on the threshold of Case 3 would likely include some false events.

The failure probability calculation approach could be used as guidance for selection of RU limiter when an active LBO control, based on precursor events, is employed. The approach used in this example calculation provides a scheme for estimating the reliability of the margin sensing in order to prevent LBO.

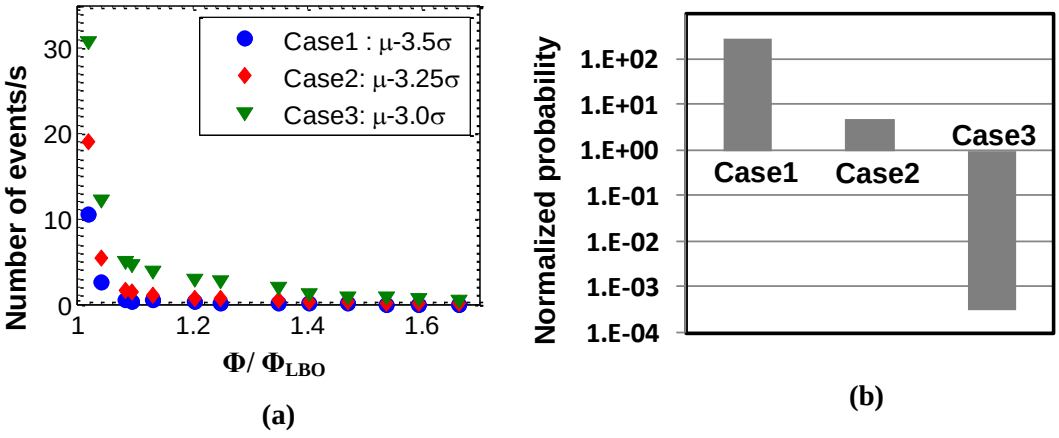

Figure 79. (a) Average event rates for different lower threshold settings; (b) probability of failure to sense LBO for different event rate trends.

6.4.2. Event based active control

The above analysis addresses whether precursors occur before LBO in a deceleration transient. It does not address the possible reduction in transient response due to precursor event occurrence and the control action in response to the events. In order to investigate this possible reduction in transient response, an additional controller responding to precursor events is added to the simulation. The control also simulates the practical scenario, where LBO is controlled based on precursor detection.

For the simulation, LBO is assumed to be at Φ=0.51, above the minimum equivalence ratio attained during the modified RU limiter case (Φ=0.49). Events are simulated in real time, similar to the simulation shown in Figure 75, using the μ-3.25σ threshold event rates. Possible control actions in response to event occurrences are: 1) increase the fuel flow for a brief period in order to increase equivalence ratio, and 2)

maintain a constant fuel flow for a brief period, to allow the air flow rate to drop, thereby increasing the equivalence ratio. For this simulation, the constant fuel flow option is used. The event based controller commands the fuel flow rate to be paused for about 100 ms when an event is detected. A maximum comparator approach is used, i.e., the maximum of the fuel flows calculated by the event based controller and the regular engine controller is provided as the command to the engine.

Equivalence ratio responses with the event based controller and without the event based controller (modified RU limiter case) are shown in Figure 80. With the controller responding to precursor events, the combustor is prevented from going below the LBO limit. Events simulated in real time and the equivalence ratio response (normalized as Φ/Φ_{LBO}) are shown in Figure 81 on an expanded scale. The pause in the fuel flow reduction clearly prevents the combustor from going below the LBO limit. The number of events in the simulation is about 13 over the three seconds that the combustor operates near the LBO limit.

The thrust response for the modified RU limiter control with the added event based controller is shown in Figure 82, along with a comparison to the case without the event based controller (presented earlier). The thrust response with the event based controller is nearly the same as the case with only the modified RU limit, just marginally slower. The response is not reduced even in the scenario where the LBO limit is above the assumed RU margin limit. For cases where LBO is below the minimum equivalence ratio, the thrust response would be nearly the same. Thus the addition of an event based controller should not significantly affect the transient response improvements estimated using the simulation with just the modified RU limit.

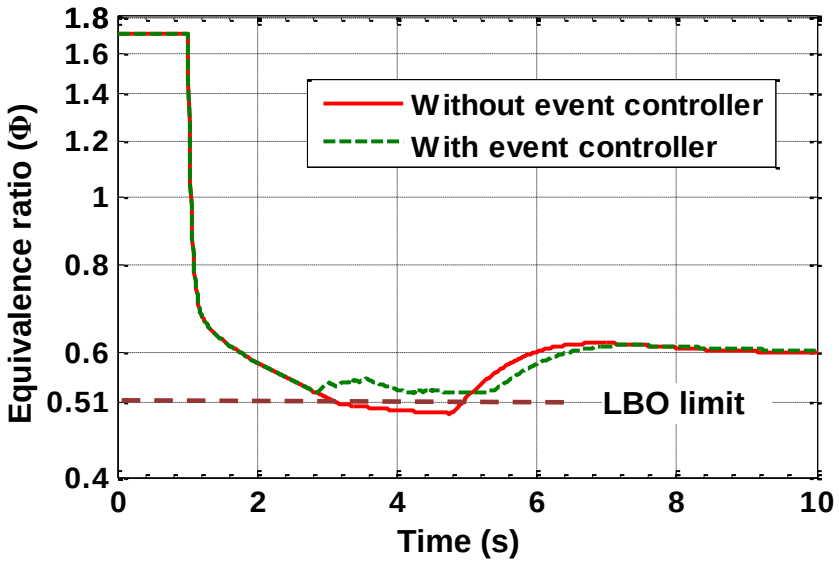

Figure 80. Equivalence ratio response for the modified RU limiter case and event based control case assuming Φ_{LBO}=0.51.

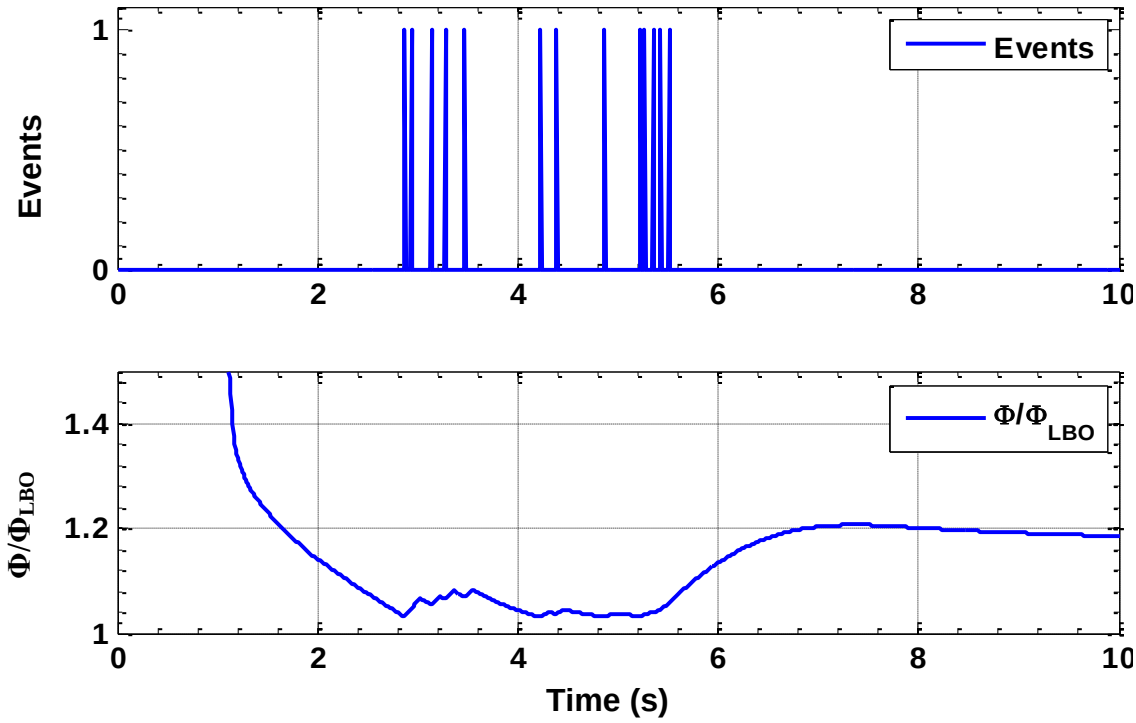

Figure 81. Simulated events in real-time (top) and normalized equivalence ratio

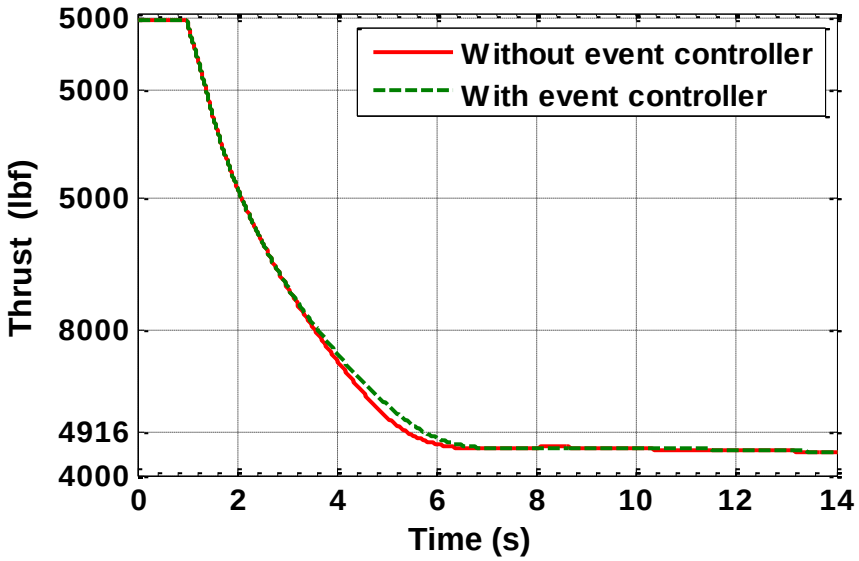

Figure 82. Thrust responses for the modified RU limiter case and with event based control case.

6.5. Summary

Precursors are discrete events and were observed to occur randomly with wide variations in the time between successive events. The random nature indicates that for a sufficiently fast transient that moves the system towards LBO, precursors may not occur before the flame is lost. Therefore an analysis is required for estimating the probability that at least one precursor occurs before LBO during a power transient.

For both the LDI and gas-fueled combustor data, the time between successive precursor events (TBE) is well modeled with an exponential distribution, except for a slight mismatch at smaller time scales, possibly due to the finite duration of precursors, which is not included in the theoretical distribution. The exponential distribution for TBE implies that precursor event occurrences can be modeled with Poisson statistics. Poisson statistics can thus be used to calculate the probability of at least one precursor occurring before LBO during a transient. This method provides a basis for determining the maximum allowed fuel flow reduction rate that can be implemented without risking flame loss. Moreover, it was demonstrated that discrete event simulation approaches can

be used for simulating precursor events in real-time. This enables simulation and analysis of LBO control approaches based on precursor event detection.

Results presented here show that LBO margins can be reduced during deceleration transients in turbine engines, thus improving transient response. The possible improvements in transient response are examined in a model turbofan engine simulation. The results indicated considerable improvement in thrust response (33%) by a reasonable reduction in the LBO margin (12%). An approach has been proposed for providing a basis for LBO margin reduction while implementing margin sensors, such that the margin sensing is reliable to the same degree as provided by the higher LBO margin without sensing and control. An active LBO control approach simulating precursor event based LBO control in engines during deceleration transients was also demonstrated.

CHAPTER 7

CONCLUSIONS AND RECOMMENDATIONS

This chapter summarizes the findings of this thesis, describes the potential impact of the results, and provides recommendations for future work in the area of LBO precursor sensing and control.

7.1 Summary and Conclusions

The four primary objectives of this thesis and the approach for each are listed below. Following that, more detailed conclusions are presented.

Robust LBO Margin Sensing

1) **To investigate LBO margin sensing under dynamically unstable conditions**, as this issue has not been addressed in previous studies. This was accomplished by investigating LBO margin sensing in a premixed gas-fueled combustor that exhibited pronounced combustion dynamics.
2) **To investigate LBO margin sensing under combustor operating conditions that are more representative of practical combustors**, i.e., at elevated pressure and preheat temperature operation. This has been addressed by investigating margin sensing in a liquid-fueled, LDI-type combustor designed for low NO_x emissions and operating at elevated pressure and temperature.

LBO Margin Sensing for Rapid Transients

3) **To analyze the limitations of LBO margin sensing approach in rapid transients leading to LBO.** This has been accomplished by developing a

probability model and analysis approach for the time between the random precursor events.

4) **To address the benefits and issues in implementing the LBO margin sensing in deceleration transients of aircraft engines.** This issue has been addressed by simulating the transient response of a turbofan engine with the addition of probability models for the LBO limit and the appearance of precursors during the transient.

7.1.1. Robust LBO Margin Sensing

In previous studies, LBO margin sensing was mainly studied under dynamically stable conditions. As dynamic instability can considerably alter flame and flow fields, it was initially uncertain if the previously observed LBO precursors would exist or be detectable in optical and acoustic signals dominated by high amplitude instability. To address these issues, margin sensing was studied in a gas-fueled combustor configuration with a centerbody, representative of ground-based gas turbine combustors. Through appropriate choice of combustor length, the system could be made to exhibit strong dynamic instability. In order to examine margin sensing under different instability scenarios, the combustor was capable of operating in a premixed mode with fuel added far upstream, and a mode with fuel addition just upstream of the dump plane, providing dynamics that included equivalence ratio oscillations mechanism.

The results of Chapter 4 demonstrated that precursor events still exist in the presence of dynamics, and their characteristics are not significantly altered by the presence of dynamics. Though precursors could be detected in the raw optical signals with large scale dynamic fluctuations, different event detection approaches were required for the different instability modes. Low-pass filtering of the signal, however, was shown to suppress the dynamics in the signal and provide the same precursor signature for all the three cases: dynamically stable, and unstable with and without equivalence ratio

oscillations. The universal signature allowed a single precursor detection algorithm to work regardless of the dynamic stability characteristics of the combustor. This is important because the dynamic characteristics in fielded engines can change with operating conditions. Therefore, having one common detection algorithm greatly reduces the complexity of the detection software.

Precursor events detected in the optical signals were observed to increase in number as LBO conditions were approached, providing a clear measure of the proximity to LBO. On average, the event occurrence rate near LBO was observed to be in the range of 1-2 per second and the event durations were in the range 20-50 ms. A novel parameter defined in this thesis, the Stability Index (*SI*), combines event rate, event duration and event strength to produce a more robust LBO proximity parameter that provides a higher dynamic range between statically stable and nearly unstable operating conditions.

The same LBO precursor detection approach was applied to a different combustor configuration, a liquid-fueled, LDI combustor operating at elevated pressure and preheat temperature. Near LBO, the combustor exhibited partial extinction and re-ignition events. These events were observed to have much shorter durations (1.5-3 ms) compared to the gas-fueled combustor. In addition, this combustor produced a higher average event rate near LBO. The experimental data from the gas-fueled combustor show that the LBO precursors correspond to the flame temporarily switching from a compact flame mode with burning around the inner recirculation zone to a long flame with most of the burning taking place downstream. In the LDI combustor, on the other hand, no such flame mode change was observed; rather the precursors appear to be local extinctions in the flame close to the injector.

The LDI combustor operated with a moderate level of dynamic instability occurring at multiple frequencies. The period of the dynamic instability (1.4-1.7 ms) was similar to the duration of the precursor events in the LDI combustor. While events were sometimes observable in the raw optical signals, comparison to high speed imaging

suggested other events could be obscured by dynamic oscillations and high frequency noise. Once again, low-pass filtering enabled robust event detection. In the optical signals, CH^* chemiluminescence showed improved performance compared to OH^* chemiluminescence, producing more events near LBO. Results from this combustor were also used to demonstrate the capability of detecting LBO margin in real-time.

LBO margin sensing using acoustic signals was also investigated in both combustors. Under dynamically unstable conditions in the gas-fueled combustor, no apparent precursor signature was observed in the raw acoustic signals. However, by low-pass filtering the signals precursor signatures became evident. On the other hand in the LDI combustor, neither the raw signals nor the low-pass filtered signals revealed precursor events. One likely reason is the smaller heat release changes during precursors due to the lack of a mode change. In addition, it was demonstrated that even if precursor event durations and dynamic instability period have nearly the same time scales, low-pass filtering would be less effective for separating precursors from dynamics with acoustic detection. Finally, the effect of pressure reflections from combustor boundaries was also addressed by modeling reflections in a one-dimensional combustor geometry with an impedance jump caused by the flame. The results indicated that reflections cause ringing in the detected acoustic precursor signal. The ringing is at the combustor's natural axial mode frequency, which is often the same as the frequency of the dynamic instability. This manifestation makes it hard to separate precursors from combustion dynamics. This ringing is not a significant issue if the event duration is long compared to the round-trip travel time, which was the case for the gas-fueled combustor. It is recommended that for improved detection of precursors in the presence of dynamic instability, pressure transducer should be located at combustor exit where dynamic instability amplitudes are low, thus minimizing the affect on precursor signal.

7.1.2. LBO Margin Sensing in Rapid Transients

Precursor events are discrete and occur randomly in time with wide variations in time between events. Therefore for a sufficiently fast transient leading to LBO, precursors may not occur before blowout occurs. Hence, transients would have to be limited to a rate that allows at least one precursor to occur before LBO.

It has been shown that time between successive events can be modeled reasonably well with an exponential distribution. This indicates the event occurrence can be described by a Poisson process, or the probability of a precursor event occurring during some time can be calculated from a Poisson distribution. This distribution was used to calculate the probabilities for at least one event to occur for a transient in equivalence ratio, thus providing a basis for determining the limiting transient fuel reduction rate. It has been demonstrated that discrete event simulation approaches could be used for simulating precursor events in real-time. An illustrative test simulation matched closely with the experimental results. Such simulation capability will aid in LBO control simulations using precursor events, without having to do costly experiments.

The potential for transient response improvement, during decelerations using LBO margin sensors has been demonstrated with a simulation of a turbofan engine. The results indicated considerable improvement (33% for the example presented) in thrust response by a reasonable lowering of LBO margins (12%) while employing LBO margin sensors. An approach has been proposed for providing a basis for LBO margin reduction while implementing margin sensors, such that the margin sensing is reliable to the same degree as provided by the higher LBO margin without sensing and control. An event-based, active LBO control approach for combining with existing RU limit controllers was also described and implemented in the simulation.

7.2. Recommendations for Future Work

The precursor events in the gas-fueled combustor are associated with a flame mode shift, whereas in the LDI combustor no such shift was observed. This is an indication that not all combustors will have flame mode changes and hence precursor characteristics could vary greatly between combustors. A better knowledge of the flame and flow field dynamics near LBO are required in order to explain the observed differences and thus provide the ability to predict the expected precursor characteristics for different combustors.

An instantaneous flame image obtained during a representative long flame mode (precursor) in the gas fueled combustor is shown in Figure 83. This flame mode consists of a large downstream flame, burning most of the fuel and flame along two helical like regions. Besides the flame zones shown in the figure, a small flame near the inlet above the center body is often observed. The helical regions are most likely precessing vortex cores (PVCs) as they were observed to rotate about the combustor geometrical axis. In addition, they exist for a distance of about 1.5 times the combustor diameter, from the inlet, similar to PVCs. These helical flames could be igniting the un-burnt fuel downstream and stabilizing the downstream flame, creating a long flame mode. The PVCs could favor the presence of a flame due to relatively smaller strains rates experienced there, as was observed in a study by Stohr et al. [54]. Hence, it is possible that existence of PVCs is primarily responsible for causing a flame mode change in the gas fueled combustor. In the LDI combustor PVCs might not be present, due to its geometric features, confinement, and combustion mode, thus not resulting in a flame mode change.

To ascertain the existence of PVCs in the gas fueled combustor during precursors high speed PIV in a horizontal plane could be performed. Addition of simultaneous PLIF

(OH or CH) to PIV would further corroborate the existence of flame along PVCs. Similar experiments in the LDI combustor would show the absence of PVCs.

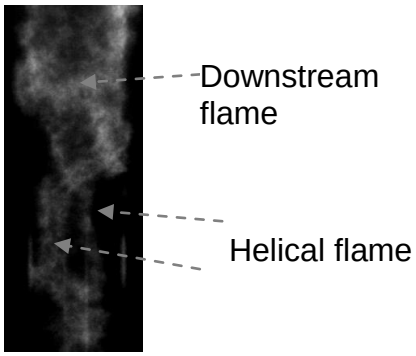

Figure 83. An example flame configuration during precursor events from a time resolved chemiluminescence image.

Combustion dynamics, mainly at low frequencies, growing in amplitude and causing blow-off is often observed in gas turbine engines. Though the current study investigated LBO margin sensing in the presence of dynamics, it does not precisely address the scenario of transient growth in dynamics causing blow-off. In the current study the dynamics were at their limit cycle amplitudes and did not exclusively cause blow-off. The possibility of precursors occurring before blow-off could be limited by the rate at which instabilities grow before resulting in blow-off, similar to the equivalence ratio reduction transients investigated in this study. LBO margin sensing for the scenario of transient growth in dynamics resulting in blow-off is worth further investigation. The transient growth could be simulated by employing a fuel system tuner (FST) to initially damp the dynamics and later letting the dynamics amplitude grow by changing the FST properties.

The acoustic precursor reflection model used in the current study could be improved further by including transmission losses at wall boundary layers. Such analysis would give a more accurate waveform for reflected precursor signature. Instead of the approach used in the current study for simulating reflections, alternative approaches for simulating impulse response of the combustor could be used. For example, a layer

peeling algorithm, which is often used for simulating impulse response of a wave tube with multiple impedance jumps [84, 85], might be appropriate. With this approach, a larger number of impedance discontinuities, reflections, and, transmission losses could be implemented. In addition, the possibility of deconvolving the impulse response from the measured acoustic signal could be investigated in order to reveal the actual precursor signature.

In the current study, the exponential distribution hypothesis for time between successive events is validated using Kolmogorov-Smirnov test. Alternative hypothesis testing methods such as Shapiro-Wilk test or Anderson-Darling test could be employed for more rigorous validation. The current study demonstrated a method for calculating the probability for a given number of precursors to occur during a transient before LBO is reached. The analysis assumes that the combustor precursor statistics during a transient are the same at each condition (equivalence ratio, mass flow rate, etc.) as for the corresponding steady-state operating point. The validity of this assumption, which may fail, for example, due to thermal inertia effects, should be explored. In addition, the theoretical results could be validated by conducting several fast transients in a combustor. The discrete event simulation algorithm used in the current study for simulating precursor events in real-time can be refined by including a constraint on the minimum allowed time between two successive events in order to account for the finite duration of precursor events. Besides, alternative simulation algorithms could be explored for more accurate simulation of precursor events.

The active LBO control approach demonstrated in the current study could be refined further with more realistic implementation. For example precursor event occurrence rates could be scheduled with combustor operating conditions since the precursor properties can be expected to be dependent on the operating conditions. In addition instead of a constant RU limiter a varying RU limiter could be used, as LBO fuel-air ratio can change with the operating conditions. Besides, alternative control

methods to prevent LBO such as increasing fuel flow rate when an event is detected or selecting a minimum RU limit when the first event is detected could be explored. The deceleration transient response improvements observed in the current study could be validated by implementing margin sensing and active LBO control in a real engine. In addition to aircraft gas turbines, transient response improvements could be investigated in land based gas turbines during rapid load shedding incidents.

Though LBO margin sensing was successful in the combustors employed in the current study, the same many not be true for other combustors. The ability to detect precursor events depends on the strength of precursor events compared to the noise in the optical signals. Combustors with significant combustion unsteadiness could produce sufficiently high noise levels to prevent precursor detection. In addition, precursors should have sufficient signatures, i.e., large enough flame extinctions, in order to detect them. The spatial extent of extinction before re-ignition could be dependent on several features such as mean flow field and turbulence characteristics, non-premixedness, stratification in the mixture, and fuel spray characteristics. Such dependency can result in wide variations in the extinction and re-ignition processes between combustors. A more detailed study of dependency of extinction and re-ignition event characteristics on flow field and fuel distribution is required in order to generalize our understaning of the characteristics of precursors.

APPENDIX A

ENGINE FUEL-AIR RATIO ESTIMATION

In gas turbine engines fuel flow rate is measured directly whereas the combustor air flow rate cannot be measured. However, an estimation of combustor fuel-air ratio is required for preventing lean blowout and avoiding turbine over temperature etc. Flow through the turbine inlet nozzle (i.e, combustor exit) is choked over most of the operating range of an engine [74]. Therefore the mass flow rate through the nozzle, assuming choking is given by Eq. (A.1), where A^* is the nozzle area, K is a constant and the subscript 4 denotes combustor exist conditions. Though the equation gives a means for calculating the flow rate, combustor exit flow properties (P_{04} and T_{04}) are not usually measured, due to the harsh environment and instead combustor inlet properties are measured.

$$\dot{m}_4 = A^* \frac{P_{04}}{\sqrt{RT_{04}}} \sqrt{\gamma} \left(\frac{2}{\gamma+1} \right)^{\gamma+1/2(\gamma-1)} = K \frac{P_{04}}{\sqrt{T_{04}}} \tag{A.1}$$

The stagnation flow properties at the nozzle are nearly same as the stagnation properties sufficiently upstream of the nozzle, inside the combustor. Due to small mach numbers inside the combustor the stagnation properties can be approximately replaced by static properties, P_4 and T_4. Further, due to a small pressure drop across the combustor inlet, combustor pressure can be approximated to compressor exit static pressure, i.e, $P_4 \approx P_3$. These approximations give rise to Eq.(A.2) for the mass flow rate.

$$\dot{m}_4 \approx K \frac{P_3}{\sqrt{T_4}} \tag{A.2}$$

In combustors usually the amount of fuel is a small fraction of the airflow rate, and thus $\dot{m}_4 \approx \dot{m}_a$. The ratio of fuel flow rate to air flow rate is given by Eq. (A.3).

$$\frac{\dot{m}_f}{\dot{m}_a} \approx K \frac{\dot{m}_f}{P_3} \sqrt{T_4} \tag{A.3}$$

Since the temperature of combustion products (T4) is essentially is a function of fuel-air air ratio, we obtain

$$\frac{\dot{m}_f}{P_3} \approx fn\left(\frac{\dot{m}_f}{\dot{m}_a}\right) \tag{A.4}$$

Thus the ratio of fuel flow rate to the compressor exit static pressure (Ratio Unit, i.e, *RU*) provides a measure of combustor fuel-air ratio. However, the equation (A.4) does not indicate a linear relationship between *RU* and fuel-air ratio, due to the presence of $\sqrt{T_4}$ term. However over the operating range of an engine, the relative change in $\sqrt{T_4}$ is quite small where as P_3 changes by an order of magnitude [74]. This implies that air flow rate is approximately proportional to P_3 in Eq. (A.2) and hence *RU* is approximately linearly proportional to fuel-air ratio.

APPENDIX B

LDI FUEL NOZZLE TESTING

The fuel supply tube section of the fuel nozzle unit supplied by NASA was modified in order to fit the setup used in the study. The original fuel supply tube had an L-shaped bend with a very short straight section between the bending location and the nozzle stem (see Figure 84). However the current LDI injector required a much longer straight section before the bend to fit into the facility. In addition, it was required to increase the tube diameter slightly (from 2.28 mm OD to 3.17 mm) in order to use standard compression tube fittings. Therefore, the fuel supply tube and the tube providing the air gap were cut, leaving a short straight section, on to which straight tubes with slightly higher diameter were welded (see Figure 84). At the joining location there is a sudden change in area that may cause cavitation. Because of the modifications, it was required to test the original and modified nozzles for similar spray performance. The spray produced by each was characterized with qualitative spray imaging and Phase Doppler Particle Anemometry (PDPA).

Figure 84. The original bent fuel nozzle and the modified straight nozzle.

Spray visualization was performed in order to obtain qualitative spray structure, cone angle, etc. These experiments were carried out with pressurized water and with the

spray injected into quiescent room air. The visualization was performed by illuminating the spray with a laser sheet and taking images perpendicular to the sheet. The laser, a copper vapor laser (Meta Laser Technologies Inc, MLT-20), was operated with a pulse rate of 5.7 KHz with a pulse duration of 5 ns. The nozzles were tested with different pressure differentials in the range 30-75 psi. Example spray images obtained at 70 psi for both the nozzles are shown in Figure 85. The images show similar spray structure for both the nozzles. In addition, the spray cone angles are around 40° for both. The spray forms into a conical sheet near the nozzle orifice and subsequently breaks down into droplets. Spray images at other pressure differentials indicated similar characteristics for both nozzles.

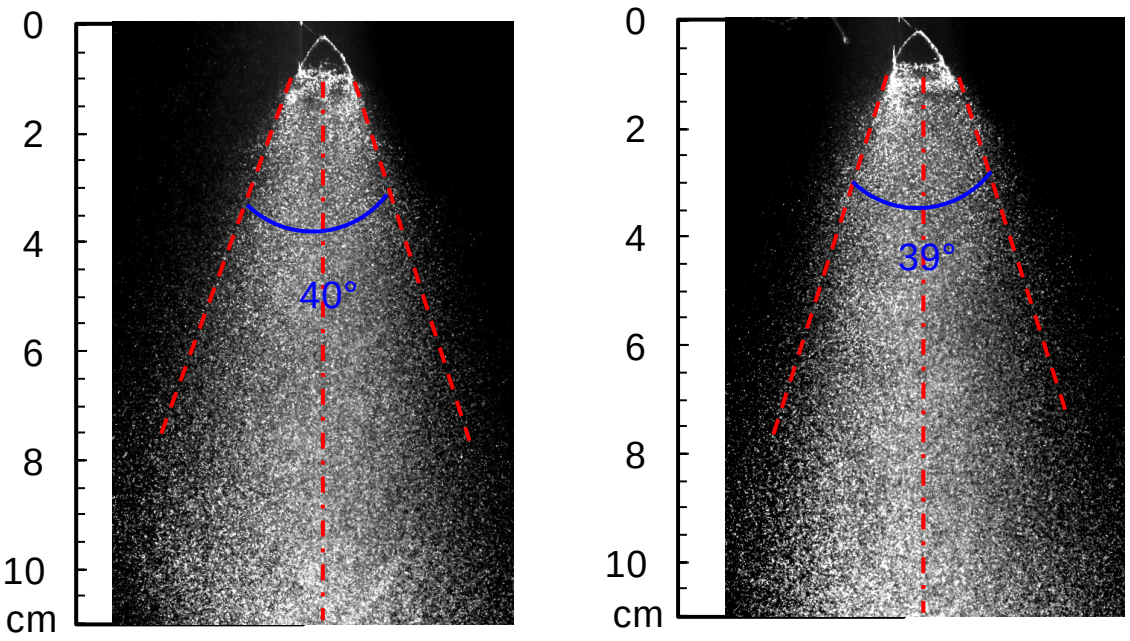

Figure 85. Spray images for (left) bent nozzle (right) straight nozzle at 70 psi pressure differential.

Spray characterization with a 2-D PDPA system was performed to measure droplet sizes and velocities. For these experiments, the pressure differential was maintained at 70 psi. Measurements were carried out in a plane perpendicular to the spray axis along a radial line. Drop diameters expressed as Sauter Mean Diameters (SMD or

D_{32}) for axial locations 20 and 50 mm from the nozzle tip are plotted in Figure 86, for the bent and straight nozzles. A radial position of zero corresponds to the spray center line. The figure conveys similar drop sizes for both nozzles. From the figure, SMD are in the range 30-80 µm, indicating that the nozzles are designed to produce a moderately fine spray.

Droplet average velocities in the axial direction are shown in Figure 87 for two axial locations. Both nozzles have similar axial velocities, and the velocity profile in the radial direction changes with axial location. Near the nozzle tip, there is a high velocity along the cone edges and lower velocities along the centerline. Farther downstream, the velocity peaks along the center line and decreases with radial distance.

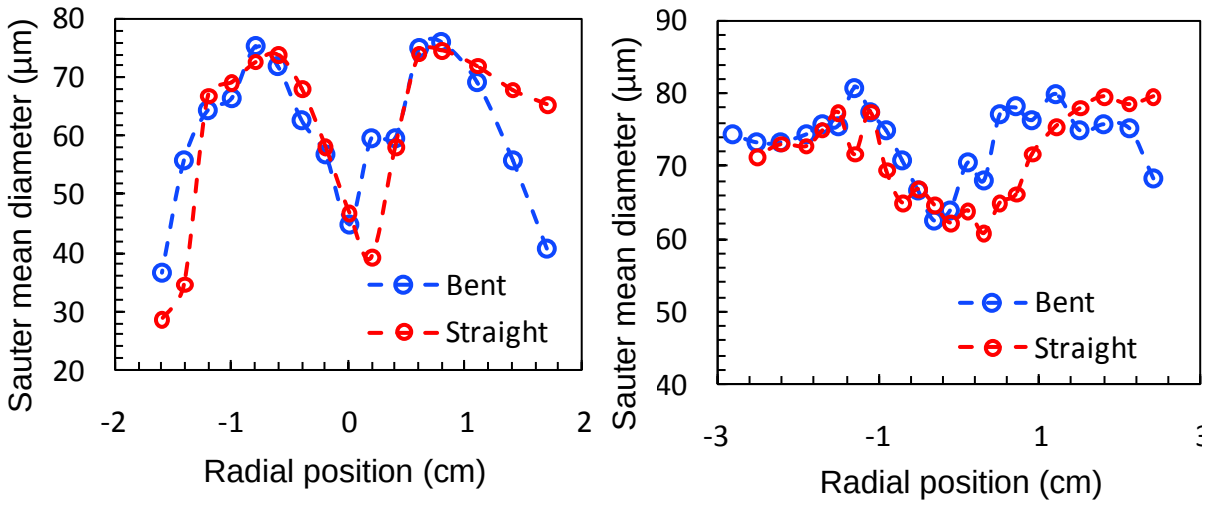

Figure 86. Droplet sauter mean drop diameters (left) at an axial location of 2cm (right) at an axial location of 5cm, from nozzle tip, for bent and straight nozzles.

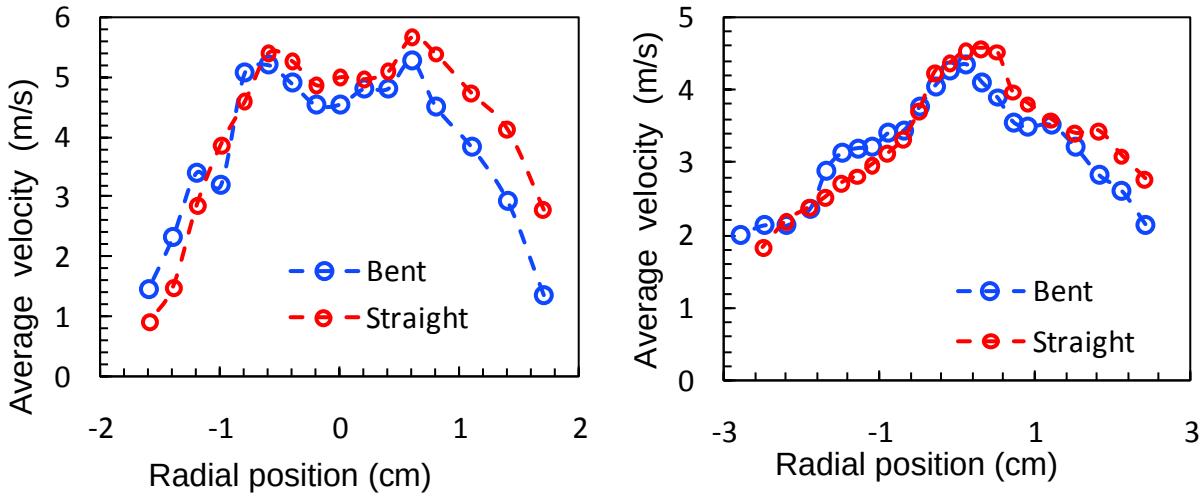

Figure 87. Droplet average axial velocities (left) at an axial location of 2cm (right) at an axial location of 5cm, from nozzle tip, for bent and straight nozzles.

APPENDIX C

LDI COMBUSTOR DEVELOPMENT

The present study used a single element LDI injector derived from a 9-element LDI injector developed by NASA Glenn Research Center [5]. The single element version uses a co-flow around the LDI element flow in order to compensate for the absence of surrounding elements. Since this was the first time the single element configuration has been operated with a co-flow, great attention was devoted to ensuring its operation was similar to the expected behavior of the multi-element LDI system. Specifically, the single element LDI injector should have a lean partially premixed flame, with low emissions, similar to the full nine-element NASA LDI injector. In addition, similarity in qualitative flame shape and flame size to the multi-element injector is desired, as practical combustors would employ multi-element configurations.

To provide confinement for the central LDI element, similar to the confinement by surrounding elements in a multi-element configuration, a co-flow is used. The co-flow is created using a perforated plate. The mass flow rate split between the co-flow and the LDI element flow determines the effective confinement. In the original nine element injector, the flow split ratio is eight (between surrounding elements and the central element), inside a square cross section of 76.2 mm on each side. For the single element injector, sitting in a test section with a circular cross section and a 76.2 mm nominal diameter, the flow split ratio that would produce the same average axial velocity ratio (in the absence of combustion) between the center element and the surrounding flow drops to 6.3. However, this does not account for any loss of confinement associated with the absence of swirl in the surrounding flow.

A perforated plate with 2.38 mm diameter holes, uniformly distributed across the plate, with an overall area blockage of 88% was designed in order to produce the required flow split ratio of 6.3. However, effective area measurements of the injector and perforated plate indicate the actual flow split ratio was closer to 8. Combustion testing of the injector with this plate produced a "clean" blue flame at atmospheric pressure, but an orange flame at elevated pressures (> 2 atm), as shown in Figure 88. In the figure, the velocity is the average un-burnt flow velocity and the temperature is the inlet air temperature. Equivalence ratio is the overall equivalence ratio, calculated from the total fuel and air flow rates. The existence of a blue flame is an indication of lean premixed/partially premixed operation, whereas the existence of an orange flame indicates formation of soot, typical for non-premixed operation. In addition, the blue flame at ~1 atm can be observed to spread to almost the entire width of the combustor, indicating that the co-flow produced less flame confinement than expected from a multi-element injector, where the flame spread would typically be limited to the size of a single element (25.4 mm). Moreover, the injector produced a twin flame structure, seen in the blue flame at atmospheric pressure, having two distinctively bright flames. Thus improvements to the injector design were required in order to reduce the flame spread and to produce a more premixed (blue) flame at elevated pressures.

In addition to the flow split ratio affecting the flame spread, fuel nozzle tip position relative to the throat of the venturi has also been observed to affect the flame spread significantly. For the images presented in Figure 88, the fuel nozzle tip was located slightly ahead of the venturi throat, by a small distance of ~1 mm. However placing the nozzle tip slightly behind the venturi throat, at a distance of 1.5 mm, produced a significant decrease in flame spread at atmospheric pressure, as shown in Figure 89. In addition, the twin flame structure observed earlier disappeared. Even with this improvement, there was a slight appearance of orange trails in the atmospheric tests,

indicating excessive non-premixedness, and an orange flame was observed at elevated pressures.

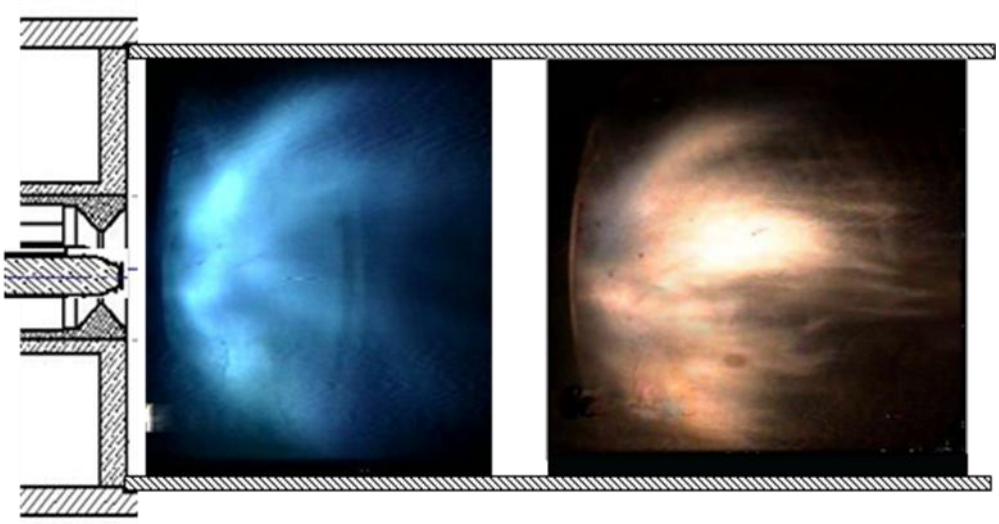

Figure 88. Flame in the LDI combustor for (a) P=1.17 atm, T=663 K, V=14 m/s, $\Phi_{overall}$=0.5 (b) P=2atm, T=682K, V=10.6m/s, $\Phi_{overall}$ =0.3.

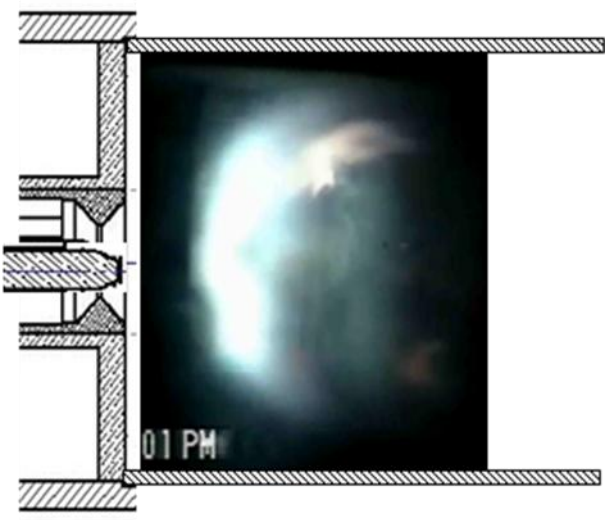

Figure 89. Flame in the combustor at P=1.13 atm, T=654K, V= 13.4m/s, $\Phi_{overall}$=0.32, for fuel nozzle position upstream of venturi throat.

Improved operation was obtained by reducing the flow split ratio close to 6.3. For a given average velocity in the combustor, the reduced flow split ratio results in a higher velocity through the LDI element. Higher air velocity through LDI element's venturi

throat would improve spray break up creating finer droplets promoting premixed combustion. However, a reduction in flow split would decrease confinement by the co-flow, as its mass flow rate decreases. To compensate for this, the co-flow velocity profile was modified such that there is a higher velocity surrounding the center and lower farther away. To achieve such a profile, some of the holes away from the center were blocked. Besides the flow split modification, the fuel nozzle tip was positioned behind the venturi at a distance of ~1 mm. This arrangement produced a blue flame at atmospheric pressure and at elevated pressures, as shown in Figure 90. In addition, the flame spread is reduced, suggesting improved confinement of the fuel/flame by the higher velocity co-flow. All the LBO sensing results in this thesis correspond to combustor operating in this final configuration.

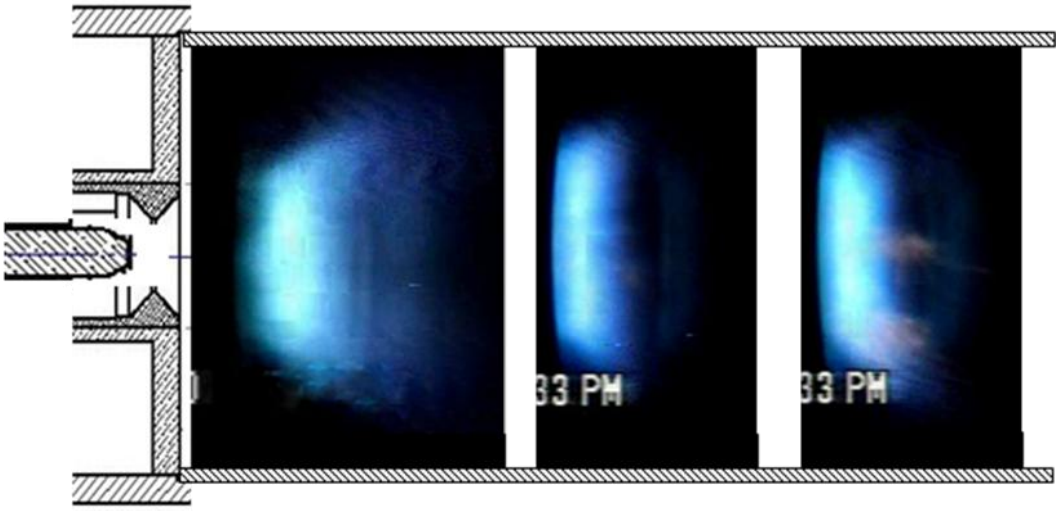

Figure 90. Flame in the combustor at (a) P=1atm, T=663K , V=14 m/s, $\Phi_{overall}$=0.41 (b) P=2atm, T=682K, V=10.6m/s, $\Phi_{overall}$=0.28 (c) P=4atm, T=733K, V=12m/s, $\Phi_{overall}$=0.23 .

REFERENCES

1. Bowman, C. T. "Control of combustion-generated nitrogen oxide emissions: technology driven by regulation," *Symposium (International) on Combustion* Vol. 24, No. 1, 1992, pp. 859-878.

2. Penner, J. E., Lister, D., Griggs, D. J. Dokken, D. J. and McFarland, M., "Aviation and the Global Atmosphere: A Special Report of the Intergovernmental Panel on Climate Change." Cambridge, UK., 1999.

3. Sanjay, M. C. "A review of NOx formation under gas-turbine combustion conditions," *Combustion science and technology* Vol. 87, No. 1-6, 1993, pp. 329-362.

4. Gokulakrishnan, P., Ramotowski, M., Gaines, G., Fuller, C., Joklik, R., Eskin, L., Klassen, M., and Roby, R. "A Novel Low NO Lean, Premixed, and Prevaporized Combustion System for Liquid Fuels," *Journal of Engineering for Gas Turbines and Power* Vol. 130, No. 5, 2008, p. 051501.

5. Tacina, K. M., Lee, C. M., and Wey, C. " NASA Glenn High Pressure Low NOx Emissions Research." NASA/TM-2008-214974, 2008.

6. Feitelberg, A. S., and Lacey, M. A. "The GE rich-quench-lean gas turbine combustor," *Journal of engineering for gas turbines and power* Vol. 120, No. 3, 1998, pp. 508-508.

7. Lefebvre, A. H. *Gas turbine combustion*, Taylor & Francis publishers, Philadelphia, 1998.

8. Lilley, D. G. "Swirl Flows in Combustion - Review," *AIAA Journal* Vol. 15, No. 8, 1977, pp. 1063-1078.

9. Sung, C., and Law, C. "Extinction mechanisms of near-limit premixed flames and extended limits of flammability," *Symposium (International) on Combustion* Vol. 26, No. 1, 1996, pp. 865-873.

10. Mitch Cohen "7F Users Group – preventing blowout trips." Comined Cycle Journal, 3rd quarter, 2011.

11. Bahr, D. "Technology for the design of high temperature rise combustors," *Journal of propulsion and power* Vol. 3, No. 2, 1987, pp. 179-86.

12. Mongia, H. C. "TAPS–A 4th Generation Propulsion Combustor Technology for Low Emissions," *2003 AIAA/ICAS International Air and Space Symposium and Exposition: The Next 100 Years*. Dayton, OH, 2003.

13. Lenertz, J. E. "Deceleration fuel control system for a turbine engine." U.S., Patenet 5596871, 1997.

14. Longwell, J. P., Frost, E. E., and Weiss, M. A. "Flame stability in bluff body recirculation zones," *Industrial & Engineering Chemistry* Vol. 45, No. 8, 1953, pp. 1629-1633.

15. Shanbhogue, S. J., Husain, S., and Lieuwen, T. "Lean blowoff of bluff body stabilized flames: Scaling and dynamics," *Progress in Energy and Combustion Science* Vol. 35, No. 1, 2009, pp. 98-120.

16. Zukoski, E. E. "Afterburners," *Aerothermodynamics of aircraft engine components*. AIAA education series, New York, NY, 1985.

17. Hedman, P. O., Fletcher, T. H., Graham, S. G., Timothy, G. W., Flores, D. V., and Haslam, J. K. "Observations of Flame Behavior in a Laboratory-Scale Pre-mixed Natural Gas/Air Gas Turbine Combustor from PLIF measurements of OH," *Journal of Engineering for Gas Turbines and Power* Vol. 127, No. 4, 2005, pp. 724-739.

18. Griebel, P., Boschek, E., and Jansohn, P. "Lean Blowout Limits and NO Emissions of Turbulent, Lean Premixed, Hydrogen-Enriched Methane/Air Flames at High Pressure," *Journal of engineering for gas turbines and power* Vol. 129, No. 2, 2007, pp. 404-410.

19. Sturgess, G., Sloan, D., Lesmerises, A., Heneghan, S., and Ballal, D. "Design and development of a research combustor for lean blow-out studies," *Journal of engineering for gas turbines and power* Vol. 114, No. 1, 1992, pp. 13-19.

20. Sturgess, G., Heneghan, S., Vangsness, M., Ballal, D., Lesmerises, A., and Shouse, D. "Effects of back-pressure in a lean blowout research combustor," *Journal of engineering for gas turbines and power* Vol. 115, No. 3, 1993, pp. 486-498.

21. Muruganandam, T., Nair, S., Scarborough, D., Neumeier, Y., Jagoda, J., Lieuwen, T., Seitzman, J., and Zinn, B. "Active control of lean blowout for turbine engine combustors," *Journal of propulsion and power* Vol. 21, No. 5, 2005, pp. 807-814.

22. Nair, S., and Lieuwen, T. "Acoustic detection of blowout in premixed flames," *Journal of propulsion and power* Vol. 21, No. 1, 2005, pp. 32-39.

23. Prakash, S., Nair, S., Muruganandam, T., Neumeier, Y., Lieuwen, T., Seitzman, J. M., and Zinn, B. T. "Acoustic based rapid blowout mitigation in a swirl stabilized combustor," *ASME Turbo Expo 2005: Power for Land, Sea and Air, Paper GT2005-68589,* Reno-Tahoe, Nevada, USA, 2005.

24. Taware, A., Shah, M., Wu, P., Yang, Y., Zhou, J., and Singh, A. "Acoustics Based Prognostics for DLE Combustor Lean Blowout Detection," *ASME Turbo Expo: Power for Land, Sea, and Air, Paper GT2006-90231*, Barcelona, Spain 2006.

25. Muruganandam, T., Nair, S., Olsen, R., Neumeier, Y., Meyers, A., Jagoda, J., Lieuwen, T., Seitzman, J., and Zinn, B. "Blowout control in turbine engine combustors," *42nd Aerospace Sciences Meeting & Exhibit, Paper AIAA-2004-0637*, Reno, NV, 2004.

26. Nair, S., Muruganandam, T., Olsen, R., Meyers, A., Seitzman, J., Zinn, B., Lieuwen, T., Held, T., and Mongia, H. "Lean Blowout Detection in a Single Nozzle Swirl Cup Combustor," *42nd Aerospace Sciences Meeting & Exhibit, Paper AIAA-2004-138*, Reno, Nevada, 2004, 2004.

27. Yi, T., and Gutmark, E. J. "Real-time prediction of incipient lean blowout in gas turbine combustors," *AIAA journal* Vol. 45, No. 7, 2007, pp. 1734-1739.

28. Thornton, J. D., Straub, D. L., Chorpening, B. T., Huckaby, E. D., Richards, G. A., and Benson, K. "A combustion control and diagnostics sensor for gas turbines," *ASME Turbo Expo 2004: Power for Land, Sea, and Air, Paper GT2004-53392*, Vol. 2, Vienna, Austria 2004, pp. 535-543

29. Li, H., Zhou, X., Jeffries, J. B., and Hanson, R. K. "Active control of lean blowout in a swirl-stabilized combustor using a tunable diode laser," *Proceedings of the Combustion Institute* Vol. 31, No. 2, 2007, pp. 3215-3223.

30. Keller, J. J. "Thermoacoustic oscillations in combustion chambers of gas turbines," *AIAA journal* Vol. 33, No. 12, 1995, pp. 2280-2287.

31. Lieuwen, T. "Modeling premixed combustion-acoustic wave interactions: A review," *Journal of propulsion and power* Vol. 19, No. 5, 2003, pp. 765-781.

32. Snyder, T. S., and Rosfjord, T. J. "Active gas turbine combustion control to minimize nitrous oxide emissions." United Technologies Corporation, U.S. Patent-5706643, Jan 13, 1998.

33. Lieuwen, T. "CDMS Helps Prevent Forced Outages, Tune Engine After Overhaul," *Combined Cycle Journal, Third Quarter*, 2008.

34. Cohen, J., and Anderson, T. "Experimental Investigation of Near-Blowout Instabilities in a Lean Premixed Step Combustor," *34th AIAA Aerospace Sciences Meeting and Exhibit ,Paper AIAA-1996-0819, Reno, NV*, 1996.

35. Turns, S. R. *An introduction to combustion: concepts and applications*: McGraw-hill publications, New York, 1996.

36. Cheng, R. K. "Low Swirl Combustion," *Gas Turbine Handbook, US Dept. of Energy*, 2006.

37. Syred, N., and Beér, J. M. "Combustion in swirling flows: a review," *Combustion and Flame* Vol. 23, No. 2, 1974, pp. 143-201.

38. Hillemanns, R., Lenze, B., and Leuckel, W. "Flame Stabilization and Turbulent Exchange in Strongly Swirling Natural Gas Flames," *Twenty-First Symposuim (International on Combustion)*, Vol. 21, 1988, pp. 1445-1453.

39. Feikema, D., Chen, R. H., and Driscoll, J. F. "Enhancement of flame blowout limits by the use of swirl," *Combustion and Flame* Vol. 80, No. 2, 1990, pp. 183-195.

40. Syred, N. "A review of oscillation mechanisms and the role of the precessing vortex core (PVC) in swirl combustion systems," *Progress in Energy and Combustion Science* Vol. 32, No. 2, 2006, pp. 93-161.

41. Leibovich, S. "The structure of vortex breakdown," *Annual Review of Fluid Mechanics* Vol. 10, No. 1, 1978, pp. 221-246.

42. Lucca-Negro, O., and O'Doherty, T. "Vortex breakdown: a review," *Progress in Energy and Combustion Science* Vol. 27, No. 4, 2001, pp. 431-481.

43. Ruith, M., Chen, P., Meiburg, E., and Maxworthy, T. "Three-dimensional vortex breakdown in swirling jets and wakes: direct numerical simulation," *Journal of Fluid Mechanics* Vol. 486, No. 486, 2003, pp. 331-378.

44. Vandervort, C. "9 ppm NOx/CO combustion system for F class industrial gas turbines," *Journal of engineering for gas turbines and power* Vol. 123, No. 2, 2001, pp. 317-321.

45. Escudier, M., and Keller, J. "Recirculation in swirling flow-a manifestation of vortex breakdown," *AIAA Journal* Vol. 23, No. 1, 1985, pp. 111-116.

46. Liang, H., and Maxworthy, T. "An experimental investigation of swirling jets," *Journal of Fluid Mechanics* Vol. 525, 2005, pp. 115-159.

47. Wang, S., Hsieh, S. Y., and Yang, V. "Unsteady flow evolution in swirl injector with radial entry. I. Stationary conditions," *Physics of Fluids* Vol. 17, No. 4, 2005, p. 045106.

48. Huang, Y., and Yang, V. "Bifurcation of flame structure in a lean-premixed swirl-stabilized combustor: transition from stable to unstable flame," *Combustion and Flame* Vol. 136, No. 3, 2004, pp. 383-389.

49. Bradley, D., Gaskell, P., Gu, X., Lawes, M., and Scott, M. "Premixed turbulent flame instability and NO formation in a lean-burn swirl burner," *Combustion and Flame* Vol. 115, No. 4, 1998, pp. 515-538.

50. Chterev, I., Foti, D., Seitzman, J., Menon, S., Lieuwen, T.,. "Flow Field Characterization in a Premixed, Swirling Annular Flow," *50th AIAA Aerospace Sciences Meeting including the New Horizons Forum and Aerospace Exposition, Nashville, Tennessee, Jan. 9-12, 2012* 2012.

51. Wicksall, D., Agrawal, A., Schefer, R., and Keller, J. "The Interaction of Flame and Flow Field in a Lean Premixed Swirl-stabilized Combustor Operated on H_2/CH_4/air," *Proceedings of the Combustion Institute* Vol. 30, No. 2, 2005, pp. 2875-2883.

52. Ji, J., and Gore, J. P. "Flow structure in lean premixed swirling combustion," *Proceedings of the Combustion Institute* Vol. 29, No. 1, 2002, pp. 861-867.

53. Law, C. K. *Combustion physics*: Cambridge University Press, Cambridge, UK, 2006.

54. Stöhr, M., Boxx, I., Carter, C., and Meier, W. "Dynamics of lean blowout of a swirl-stabilized flame in a gas turbine model combustor," *Proceedings of the Combustion Institute* Vol. 33, No. 2, 2011, pp. 2953-2960.

55. Turns, S. R. *An introduction to combustion: concepts and applications*: McGraw-hill, New York , NY, 1996.

56. Peters, N. *Turbulent Combustion*: Cambridge University Press, Cambridge, UK, 2000.

57. Ballal, D., and Lefebvre, A. "Weak extinction limits of turbulent heterogeneous fuel/air mixtures," *J. Eng. Power;(United States)* Vol. 102, No. 2, 1980, pp. 416-421.

58. Strakey, P., Sidwell, T., and Ontko, J. "Investigation of the effects of hydrogen addition on lean extinction in a swirl stabilized combustor," *Proceedings of the Combustion Institute* Vol. 31, No. 2, 2007, pp. 3173-3180.

59. Hoffmann, S., Habisreuther, P., and Lenze, B. "Development and assessment of correlations for predicting stability limits of swirling flames," *Chemical Engineering and Processing: Process Intensification* Vol. 33, No. 5, 1994, pp. 393-400.

60. Sloan, D. G., and Sturgess, G. J. "Modeling of local extinction in turbulent flames," *Journal of engineering for gas turbines and power* Vol. 118, No. 2, 1996, pp. 292-307.

61. Spalding, D. "Theoretical aspects of flame stabilization: an approximate graphical method for the flame speed of mixed gases," *Aircraft Engineering and Aerospace Technology* Vol. 25, No. 9, 1953, pp. 264-276.

62. Penner, S., and Williams, F. "Recent studies on flame stabilization of premixed turbulent gases," *Applied Mechanics Reviews* Vol. 10, No. 6, 1957, pp. 229-237.

63. Zukoski, E. E. "Flame stabilization on bluff bodies at low and intermediate Reynolds numbers." PhD Thesis, California Institute of Technology, Pasadena, CA, 1954.

64. Driscoll, J. F. "Turbulent premixed combustion: Flamelet structure and its effect on turbulent burning velocities," *Progress in Energy and Combustion Science* Vol. 34, No. 1, 2008, pp. 91-134.

65. Dinkelacker, F., Soika, A., Most, D., Hofmann, D., Leipertz, A., Polifke, W., and Döbbeling, K. "Structure of locally quenched highly turbulent lean premixed flames." Vol. 27, Elsevier, 1998, pp. 857-865.

66. Ratner, A., Driscoll, J., Donbar, J., Carter, C., and Mullin, J. "Reaction zone structure of non-premixed turbulent flames in the," *Proceedings of the Combustion Institute* Vol. 28, No. 1, 2000, pp. 245-252.

67. Chaudhuri, S., Kostka, S., Renfro, M. W., and Cetegen, B. M. "Blowoff dynamics of bluff body stabilized turbulent premixed flames," *Combustion and Flame* Vol. 157, No. 4, 2010, pp. 790-802.

68. Kariuki, J., Dawson, J. R., and Mastorakos, E. "Measurements in turbulent premixed bluff body flames close to blow-off," *Combustion and Flame*, 2012.

69. Muruganandam, T. "Sensing and Dynamics of Lean Blowout in a Swirl Dump Combustor." PhD Thesis, Georgia Institute of Technology, Atlanta, GA, 2006.

70. Zhang, Q., Shanbhogue, S. J., and Lieuwen, T. "Dynamics of Premixed H_2/CH_4 Flames Under Near Blowoff Conditions," *Journal of engineering for gas turbines and power* Vol. 132, No. 11, 2010, p. 111502.

71. Nair, S. "Acoustic characterization of flame blowout phenomenon." PhD Thesis, Georgia Institute of Technology, Atlanta, GA, 2006.

72. Lee, J., and Santavicca, D. "Experimental diagnostics for the study of combustion instabilities in lean premixed combustors," *Journal of propulsion and power* Vol. 19, No. 5, 2003, pp. 735-750.

73. Docquier, N., and Candel, S. "Combustion control and sensors: a review," *Progress in Energy and Combustion Science* Vol. 28, No. 2, 2002, pp. 107-150.

74. Hill, P. G., and Peterson, C. R. *Mechanics and thermodynamics of propulsion*: Addison-Wesley, Reading, Massachusetts, 1992.

75. Spang III, H. A., and Brown, H. "Control of jet engines," *Control Engineering Practice* Vol. 7, No. 9, 1999, pp. 1043-1060.

76. May, R. D., Csank, J., Lavelle, T. M., Litt, J. S., and Guo, T. H. "A High-Fidelity Simulation of a Generic Commercial Aircraft Engine and Controller." NASA/TM-2010-216810, October, 2010.

77. Jaw, L. C., and Mattingly, J. D., *Aircraft engine controls*, American Institute of Aeronautics and Astronautics, New York, 2009.

78. Csank, J., May, R. D., Litt, J. S., and Guo, T. H. "Control Design for a Generic Commercial Aircraft Engine," NASA/TM—2010-216811, October, 2010.

79. Nori, V. N. "Modeling and analysis of chemiluminescence sensing for syngas, methane and Jet-A combustion." PhD Thesis, Georgia Institute of Technology, Atlanta, GA, 2008.

80. Walker, J. S., *Fast fourier transforms*, CRC Press, 1996.

81. Pierce, A. D., *Acoustics: An Introduction to its Physical Principles and Applications*, Acoustical Society of America, Melville, NY, 1989.

82. Yates, R. D., and Goodman, D. J., *Probability and Stochastic Processes: A Friendly Introduction for Electrical and Computer Engineers*, Jon Wiley & Sons, 2004.

83. Lewis, P. A., and Shedler, G. S. "Simulation of nonhomogeneous Poisson processes by thinning," *Naval Research Logistics Quarterly* Vol. 26, No. 3, 1979, pp. 403-413.

84. Li, A. "Improvements to the acoustic pulse reflectometry technique for measuring duct dimensions." PhD Thesis, The Open University, UK, 2004.

85. Amir, N., Shimony, U., and Rosenhouse, G. "A Discrete Model for Tubular Acoustic Systems with Varying Cross Section The Direct and Inverse Problems. Part 1: Theory," *Acta Acustica united with Acustica* Vol. 81, No. 5, 1995, pp. 450-462.